

Solidification in a thin liquid film: Growing Alq₃ needles via methanol-vapor annealing

by

Tony S. Yu

B.S. Mechanical Engineering
Columbia University, 2004

S.M. Mechanical Engineering
Massachusetts Institute of Technology, 2007

Submitted to the Department of Mechanical Engineering
in partial fulfillment of the requirements for the degree of

Doctor of Philosophy in Mechanical Engineering

at the

MASSACHUSETTS INSTITUTE OF TECHNOLOGY

February 2011

© Massachusetts Institute of Technology 2011. All rights reserved.

Author Department of Mechanical Engineering
November 30, 2010

Certified by Anette E. Hosoi
Associate Professor of Mechanical Engineering
Thesis Supervisor

Accepted by David E. Hardt
Chairman, Department Committee on Graduate Students

**Solidification in a thin liquid film:
Growing Alq₃ needles via methanol-vapor annealing**

by
Tony S. Yu

Submitted to the Department of Mechanical Engineering
on November 30, 2010, in partial fulfillment of the
requirements for the degree of
Doctor of Philosophy in Mechanical Engineering

Abstract

Organic electronics hold the promise of low-cost, flexible, large-area electronic and optoelectronic devices. In order to improve the performance of these devices, it is vital to control the morphology (*e.g.*, the crystallinity) of these thin films. This thesis examines how solvent-vapor annealing of thin, amorphous films of Alq₃—*i.e.*, tris-(8-hydroxyquinoline) aluminum—promotes the growth of single-crystal needles; we explore this system through experiments, modeling, and analytical scaling laws.

The first part of this thesis describes the growth of single-crystal Alq₃ needles from amorphous, thin films of Alq₃ annealed in methanol vapor. Micrographs captured during annealing reveal needle lengths that grow like power laws, such that $L_{\text{needle}} \sim t^\gamma$. We show that the growth exponent, γ , decreases when the thickness of the Alq₃ film is increased. In addition to needle growth, the fluid films exhibited dewetting and coarsening behavior: the initially-uniform film broke up into small drops that coalesced to form larger drops.

In the second part of this thesis, we develop a mathematical model describing these morphological changes—both drop formation and needle growth—during solvent-vapor annealing. The evolution of the fluid film is modeled by a lubrication equation, and a convection-diffusion equation captures the transport of Alq₃ and methanol within the film. We define a dimensionless transport coefficient, α , which describes the relative effects of diffusion and coarsening-driven convection. Numerical simulations based on this 1D model reproduce the film evolution observed in experiments.

The final part of this thesis describes scaling laws that govern needle growth. For large α -values, needle growth matched the theory of 1D, diffusion-driven solidification, such that $\gamma \rightarrow 1/2$. For low α -values, flow driven by drop collapses—*i.e.*, coarsening—controls the growth of needles. Within this regime, we identify two cases: needles that were small compared to the typical drop size, and those that were large. For small needles, $\gamma \rightarrow 2/5$, and for large needles, $\gamma \rightarrow 0.29$. These scaling laws provide a simple physical picture of needle growth and match numerical simulations.

Thesis Supervisor: Anette E. Hosoi
Title: Associate Professor of Mechanical Engineering

Acknowledgments

The Ph.D. is a long and difficult journey. It's especially trying for someone, such as myself, who tends to focus on failures and be doubtful of successes. Through both my master's and doctorate, Anette "Peko" Hosoi has been an encouraging and supportive mentor—a positive and optimistic balance to my negativity and pessimism (I'm only half-joking here). I was fortunate to find an advisor who is truly a great role model: A smart and creative researcher; an enthusiastic and engaging teacher; and an approachable and sympathetic mentor. Her awesomeness (What?—no one's going to read this anyway) as an advisor is reflected in the gifted students who have gravitated toward her research group.

I was also fortunate to have a very capable and supportive thesis committee. Vladimir Bulović originally proposed this research project and lent his considerable expertise on organic electronics. Meetings with him were both enlightening and enjoyable. Daniel Rothman provided his modeling expertise and was instrumental in driving this project toward an elegant modeling effort (and away from a convoluted early attempt). Evelyn Wang was always ready with suggestions to improve my experimental measurements and was a trusted advisor on career matters.

When I started this project, I had no experience with materials processing, and I want to thank everyone in the Organic and Nanostructured Electronics (ONE) lab for their help. In particular, Jill Rowehl trained me on the ONE lab equipment and was incredibly patient with me throughout the process. She was also generous with answers to my endless questions about organic electronics. In addition, I want to thank Debbie Mascaro, who's research was the inspiration for this project; she was kind enough to dig into her old lab notebook when I had questions about her solvent-annealing experiments.

In addition to my Ph.D. project, I had the opportunity to work on a number of research projects during my time at MIT. Eric Lauga—the world's expert on low Reynolds number swimming—was a great collaborator and mentor in a number of graduate-school-prolonging research projects. I also had the pleasure to work with Sunghwan (Sunny) Jung and Christophe Clanet—two of the most creative researchers I know.

Much of my time at MIT was funded through teaching. As a result, I had the opportunity to work with some wonderful professors. In particular Gareth McKinley and Simona Socrate, who (in addition to Peko) are a couple of the most engaging and thoughtful lecturers I know. If I become a professor, I'll have some excellent examples of how a great professor should teach.

I would, of course, like to thank my research group: Sungyon Lee, my close friend and local math expert; Daniel Tam, who's number one in my book; Randy Ewoldt, a rare mix of brilliance and modesty; Justin Kao, my go-to guy when I needed to rant about a paper or a seminar; Amos Winter, the design ninja; Dawn Wendell, who kept me positive during my final year of the Ph.D.; Debbie Blanchard, who kept the group functioning (and filled with chocolate); and the rest of Team Peko.

Finally, I'd like to thank the family I found here in Cambridge. This project involved 2 to 3 years of feeling incredibly stupid—followed by a year, or so, of thinking that I might have a chance at graduating. I couldn't have gotten through this experience without the love and support of my friends and family. I was particularly fortunate to live in a house filled with friends who knew the ups-and-downs of graduate school. Sungyon Lee, Barry Kudrowitz, Monica Rush, Steve Peters, Teresa Peters, and rest of the Lopez St. Family kept me from losing my mind during my time here at MIT.

Contents

1	Introduction	19
1.1	Motivation	19
1.1.1	Organic electronics and crystalline order	20
1.1.2	Nonlinear optics and waveguides	20
1.2	Previous Work	21
1.2.1	Evaporative processes	21
1.2.2	Solvent-vapor annealing	22
1.2.3	Growth of oriented Alq ₃ needles	22
1.3	Overview of thesis	24
2	Physical Background	25
2.1	Solvent-vapor annealing	25
2.1.1	Vapor equilibrium and diffusion	26
2.1.2	Adsorption and condensation of solvent-vapor	26
2.1.3	Glass-transition and plasticization	29
2.2	The physics of thin fluid films	30
2.2.1	Thin-film evolution equation	31
2.2.2	Convection-diffusion equation for thin films	32
2.2.3	Surface tension	34
2.2.4	Intermolecular interactions	35
2.2.5	Dewetting fluid films	40
2.2.6	Drop coarsening	42
2.3	Nucleation and solidification	43

2.3.1	Nucleation of solids	43
2.3.2	Interface equilibrium	45
2.3.3	Interface growth velocity (the Stefan Condition)	45
3	Experiments	47
3.1	Experimental procedure	47
3.2	Annealing chamber	48
3.3	Solvent-annealing setup	49
3.4	Needle-length measurements	51
4	Mathematical model of thin-film crystal growth	53
4.1	Thin-film evolution equation	54
4.2	Solvent-mass evolution equation	55
4.3	Pressure in the thin liquid film	56
4.4	Needle velocity	57
4.5	Rescaled governing equations	57
4.5.1	Simulation parameters	58
4.6	Numerical implementation	59
5	Analytical Results	61
5.1	Dewetting and Coarsening	61
5.1.1	Dewetting instability	61
5.1.2	Drop coarsening	63
5.2	High α -values: diffusion-dominated needle growth	66
5.3	Low α -values: coarsening-dominated needle growth	67
5.3.1	Mass conservation at the growing needle tip	68
5.4	Needle growth for low α -values and small h_{solid}	70
5.5	Needle growth for low α -values and large h_{solid}	71
5.5.1	Flux through the wetting layer	71
5.5.2	Needle growth	74

6 Results and Discussion	77
6.1 Overview	77
6.1.1 Experiments	77
6.1.2 Simulations	78
6.1.3 Comparing simulations and experiments	79
6.2 Needle Growth	80
6.2.1 Evolution of needle lengths in experiments	80
6.2.2 Influence Alq ₃ film thickness, \tilde{h}_{Alq}	81
6.2.3 Influence of transport coefficient, α	82
6.2.4 Comparing needle growth in simulations and experiments	84
6.2.5 Influence of needle thickness, h_{solid}	84
6.2.6 Influence of initial concentration, ϕ_0	86
6.2.7 Influence of equilibrium film thickness, ε	87
6.3 Dewetting and coarsening	87
6.3.1 Dewetting and coarsening in simulations	88
6.3.2 Dewetting and coarsening in experiments	89
6.4 Growth of the wetting layer	89
6.4.1 Variation of the wetting-layer thickness for large h_{solid}	90
6.4.2 Growth of the wetting layer in simulations	91
6.5 Crystal nucleation and morphology in experiments	91
6.5.1 Nucleation sites and hole formation	92
6.5.2 Influence of solvent concentration on nucleation	93
6.5.3 Anisotropy of needle growth	93
6.5.4 Splintering needles for thick Alq ₃ -films	94
6.6 Open issues	95
6.6.1 Resolution of micrographs taken during solvent annealing	95
6.6.2 Faster-than- $t^{1/2}$ needle growth in experiments	96
6.6.3 The lubrication approximation	97
6.6.4 Concentration-dependent material properties	97
6.6.5 Meniscus at the needle tip	97

6.6.6	Intermolecular pressure exponents	98
6.6.7	Retarded van der Waals interactions	99
7	Conclusions and Outlook	101
A	Phase transitions and equilibria	105
A.1	Nucleation of drops, holes, and solids	105
A.2	Coarsening in liquid drops and separated phases	105
A.2.1	Coarsening of a phase-separated mixture	106
A.2.2	Comparison between coarsening of drops and particles	107
B	Finite-difference formulations	109
B.1	Nomenclature	109
B.2	Newton's Method of root-finding	110
B.3	Jacobian	111
B.4	Discretization of thin-film equations in 1D	112
B.4.1	Discretization of film thickness equation	112
B.4.2	Interface values—a word of warning	114
B.5	Discretization of convection-diffusion equation	115
B.6	No-flux boundary condition at right edge	116
B.6.1	Thin-film equation	117
B.6.2	Solvent-mass equation	118
B.7	Boundary conditions at the growing needle tip	118
B.7.1	Discretization at the needle tip	119
B.7.2	Solving the governing equations at the needle tip	120
B.7.3	Solving for the velocity at the needle tip	122
B.7.4	Eating nodes	124
C	Miscellaneous	127
C.1	Filtering needle growth data	127
C.2	Measuring the growth-exponent in simulations	128
C.2.1	Growth-exponent transition at late times	128

C.2.2	Numerical transient in needle growth	128
C.2.3	Perturbations in the growth-exponent due to drop collapse	129
C.3	Marangoni effects	130
C.3.1	Flows driven by Marangoni effects	130
C.3.2	Marangoni effects vs. capillary effects	131
C.4	Cleaning procedure for silicon/glass wafers	132
C.5	Methanol properties	132

List of Figures

1-1 Schematic and micrograph of Alq ₃ needle and surrounding fluid.	19
1-2 Micrograph of fluorescing Alq ₃ needle	21
1-3 Experimental results from Mascaro [58]	23
2-1 Wetting scenarios for molecules of C in a fluid B near a solid surface A.	27
2-2 Supercritical and subcritical condensation regimes.	28
2-3 Schematic of phase diagram for glass transition	29
2-4 Schematic of absorption	30
2-5 Schematic of a thin liquid film	31
2-6 Schematic of pressure jump across a curved interface	34
2-7 Intermolecular interactions between molecules and surfaces.	35
2-8 Intermolecular potential and pressure	37
2-9 Dewetting instability of thin liquid films	40
2-10 Hole formation from Becker <i>et al.</i> [4]	42
2-11 Schematic of drop collapse and collision	43
2-12 Total-free-energy change vs. the nucleus size	44
2-13 Local thermodynamic equilibrium at a solid/liquid interface	45
3-1 Micrograph of region around Alq ₃ needle	47
3-2 Experimental procedure	48
3-3 Annealing chamber	48
3-4 Experimental setup	50
3-5 Time-lapse micrographs of growing needle cluster	50

4-1	Schematic of thin film with thickness, h , and solvent-concentration, ϕ	53
4-2	Local solvent concentration near the needle tip	55
4-3	Finite-difference discretization near the needle tip	60
5-1	Dispersion relation for dewetting instability	62
5-2	Schematic of a collapsing droplet	64
5-3	Schematic of meniscus region at the needle tip	68
5-4	Schematic of wetting layer and drops in front of growing needle	69
5-5	Schematic of a small needle.	70
5-6	Schematic of a large needle	71
5-7	Schematic of growing wetting layer	72
6-1	Glass substrate after annealing for 3 hours.	78
6-2	Evolution of needle lengths	80
6-3	Histogram of growth exponents	81
6-4	Micrographs and histograms for various Alq ₃ film-thicknesses	82
6-5	Growth exponent vs. α	83
6-6	Growth exponents from experiments as a function of α	83
6-7	Growth exponent vs. h_{solid}	85
6-8	SEM image of needle tip	85
6-9	Needle evolution for different initial concentrations, ϕ_0	86
6-10	Needle evolution for different equilibrium thickness, ε	87
6-11	Droplet dewetting and coarsening in simulations	88
6-12	Wetting-layer for very large needle heights.	90
6-13	Plot of the wetting layer evolution	91
6-14	SEM image of needles and nucleation site	92
6-15	Possible hole formation in thick Alq ₃ films.	92
6-16	Micrograph of Alq ₃ splotches	93
6-17	Micrograph from wetting experiment	94
6-18	Crystal morphology for different Alq ₃ -film thicknesses	95
6-19	Comparison of menisci at the needle tip	98

B-1	Nodes and interfaces on the computational mesh	109
B-2	Arbitrary function, $f(x)$ near root.	110
B-3	Schematic of no-flux boundary condition at right boundary.	116
B-4	Discretization of the region near the tip of a growing, 1D crystal.	119
B-5	Schematic showing interpolation of mesh-values near the needle tip	120
B-6	Schematic of mesh deformation due to needle growth	123
B-7	Schematic of mesh node destruction due to advancing needle	125
C-1	Micrograph and histogram of obstructed and unobstructed needles	127
C-2	Transition of growth-exponent, γ , at late times	128
C-3	Numerical transient in needle growth	129
C-4	Perturbation of the growth-exponent due to drop collapse	130
C-5	Shear flow driven by the Marangoni effect	130

List of Tables

2.1	Physical interpretation of terms in intermolecular pressure	37
3.1	Experimental parameters	48
4.1	Dimensionless variables	54
4.2	Relevant dimensionless groups for the binary thin film.	57
5.1	Scaling laws for needle growth	75
6.1	Range of dimensionless parameters explored in simulations	79
A.1	Comparison of drop-coarsening and particle-coarsening	108
B.1	Coefficients for Jacobian terms of thin-film equation (h -derivatives)	114
B.2	Coefficients for Jacobian terms of solvent-mass equation (ϕ -derivatives) . . .	114
B.3	Coefficients for Jacobian terms of solvent-mass equation (h -derivatives) . . .	116
B.4	Coefficients for Jacobian terms of solvent-mass equation (ϕ -derivatives) . . .	117
B.5	Coefficients for Jacobian terms of thin-film equation at right boundary . . .	118
B.6	Coefficients for Jacobian terms of solvent-mass equation at right boundary .	119
C.1	Cleaning procedure for glass substrates.	132
C.2	Methanol properties	133

Chapter 1

Introduction

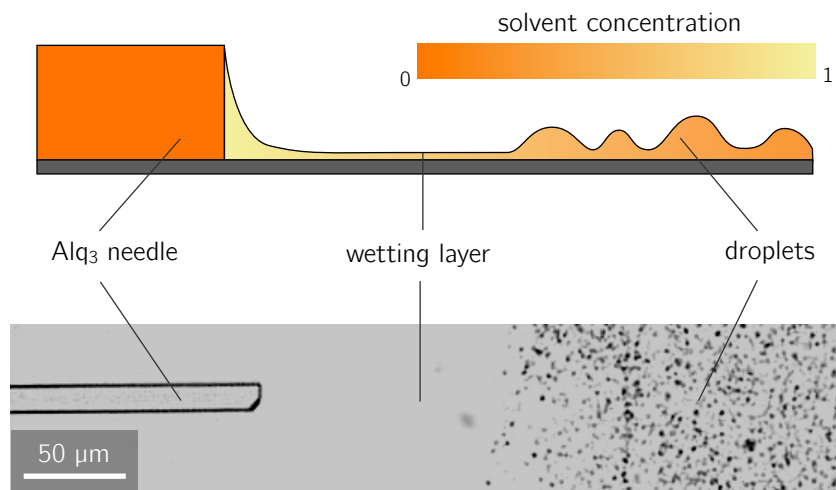


Figure 1-1: Top: schematic of needle growing into a fluid film with a varying solvent concentration. Bottom: optical micrograph of area surrounding an Alq₃ needle after annealing the Alq₃ film for 3 hours. The rectangular needle (entering from the left of the image) is surrounded by a clear wetting layer of fluid and small droplets. Note: the schematic is drawn in the plane of the substrate, while the micrograph shows a top-down view of the substrate.

1.1 Motivation

“The dream for many scientists is . . . to produce easy-to-process yet highly ordered molecular systems” [62]. In an effort to realize this goal, I grow single-crystal organic needles (see Fig. 1-1) and present a mathematical model describing their solidification from a thin, liquid film.

1.1.1 Organic electronics and crystalline order

Organic materials hold the potential for flexible, lightweight, large-area electronic [30] and optoelectronic devices [34]. The intermolecular forces that bind organic semiconductors together are weak relative to the covalent bonds of traditional semiconductors, such as silicon and germanium [71]. As a result, organic materials are ideal for electronic devices that require mechanical flexibility [33]. These weaker bonds also allow the use of low-temperature or solvent processing techniques, which could significantly reduce manufacturing costs. Furthermore, the properties of organic molecules can be custom-tailored for specific applications (*e.g.*, color tuning in electroluminescent materials [63]). But, whereas the method for producing single-crystal silicon for electronics is well understood [31], controlling the morphology (*e.g.*, the crystallinity) of organic materials remains a challenge [57].

To make organic devices commercially-viable, further research is required to understand changes in film morphology during deposition, post-processing (*e.g.*, annealing), and device operation. Although the isotropic and homogenous nature of amorphous films benefits organic, light-emitting diodes (OLEDs), oriented, crystalline films of organic semiconductors are better suited for “polarized light emission, OFETs [organic field-effect transistors], or organic solid-state injection lasers” [67]. In fact, previous solvent-vapor annealing experiments have shown that increased crystalline order can improve electroluminescence [5] and the performance of transistors [28] and photovoltaics [64] due to their enhanced charge mobility¹ compared to their amorphous counterparts [49].

For further information on the use of organic semiconductors in electronic and optoelectronic devices and the differences between amorphous and crystalline materials, see the recent review by Shirota and Kageyama [86].

1.1.2 Nonlinear optics and waveguides

This thesis focuses on the growth of long, slender, single-crystal “needles” of the organic semiconductor Alq₃, tris-(8-hydroxyquinoline) aluminum, as shown in Fig. 1-2. Alq₃ exhibits highly-nonlinear optical properties due to its non-centrosymmetric crystal packing

¹Charge-mobility relates the drift of electric charges in response to an applied voltage and is akin to a diffusivity per volt.

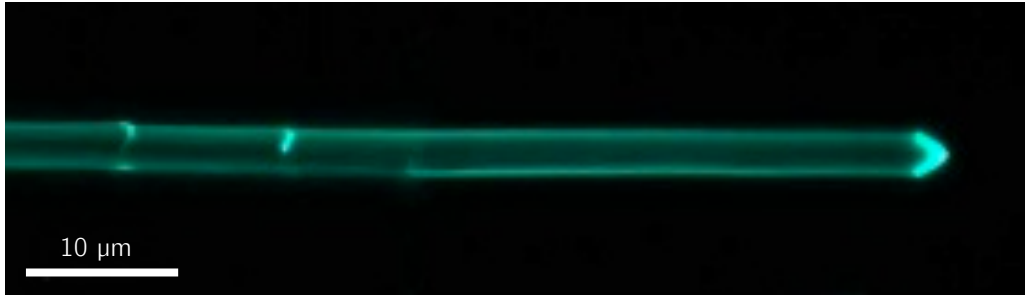


Figure 1-2: Micrograph of Alq₃ needle fluorescing in ultra-violet light. From Mascaro 2004 [58].

[51]. Furthermore, the needle-like geometry acts as an optical waveguide: the small cross-sections concentrate the intensity of the incoming light, and the long lengths increase the interaction distance to enhance nonlinear effects [88, 87].

These highly-non-linear optical effects allow Alq₃ needles to alter the phase, frequency, amplitude, or polarity of incoming light [56]. Such interactions facilitate the development of novel optoelectronics, including frequency generators and convertors, all-optical switches, and optical computing [70]. In particular, optical nonlinearities can be exploited to produce optical switches for high-bandwidth telecommunications networks [66].

1.2 Previous Work

While the predominant process for producing single-crystal silicon has existed for almost a century [31], the production of organic semiconductors is less mature. Active research includes ink-jet printing, stamping/templating, physical- and chemical-vapor deposition, solution deposition (drop-casting), and thermal and solvent-vapor annealing (see Liu *et al.* [55] for a review). Here, we focus on crystallizing and organizing organic molecules through solution-based synthesis [99]; specifically, we discuss evaporative processes and solvent-vapor annealing.

1.2.1 Evaporative processes

In solution-deposition processes, such as spin-coating and drop-casting, organic molecules and polymers are mixed with organic solvents and then deposited on substrates. As the solvent evaporates, molecule-molecule, molecule-solvent, and molecule-substrate interactions

compete and, under the right conditions, produce self-assembled structures [76]. For example, Hameren *et al.* [98] deposited drops of disk-like porphyrin dyes dissolved in chloroform onto glass substrates. As the chloroform evaporated, the receding contact line guided the self-assembly of the disk-like molecules in columnar stacks both parallel (for small volumes) and perpendicular (for large volumes) to the contact line. Similarly, experiments and simulations by Rabani *et al.* [79] demonstrated pattern formation during the evaporation of solvent from a nano-particle solution.

1.2.2 Solvent-vapor annealing

Many deposition processes produce amorphous and polycrystalline thin films, which can be annealed to increase crystalline order. When organic thin films are exposed to an atmosphere of solvent-vapor, interactions between the organic molecules and solvent imparts mobility on the thin film, as we discuss in §2.1. Researchers have successfully used solvent-vapor annealing to produce single-crystal needles (also known as fibers or wires) of P3OT² [102, 103], PDI³ [22], HBC⁴ [23] and PE-PTCDI⁵ [19].

Needle formation during solvent-annealing is driven by interactions between organic molecules, the solvent, and the substrate. Datar *et al.* [19] suggest that the solvent affinity to the surface governs the amount of solvent on the substrate (as opposed to solvent affinity to the molecule). And, they claim, more solvent leads to better molecular packing. De Luca *et al.* [23] suggest that stronger molecule-molecule interactions lead to weakly-ordered systems, while strong solvent-molecule interactions lead to high molecular-ordering; presumably because highly-ordered crystals have stronger crystalline interactions to overcome strong solvent-molecule interactions.

1.2.3 Growth of oriented Alq₃ needles

This thesis continues the work of Mascaro *et al.* [58, 59], who grew Alq₃ needles up to a centimeter long, with cross sections of less than a micron in size. The researchers first evaporated

²Poly(3-octylthiophene)

³perylene-bis(dicarboximide)

⁴hexa-*peri*-hexabenzocoronene

⁵propoxyethyl perylene tetracarboxylic diimide

thin (10–20 nm), amorphous films of Alq₃ onto silicon or glass substrates. These substrates were then annealed in a solvent vapor (chloroform or methanol) at room temperature and atmospheric pressure to produce single-crystal Alq₃ needles (similar to the needle shown in Fig. 1-1). These needles had heights and widths on the order of microns and lengths of up to a centimeter.

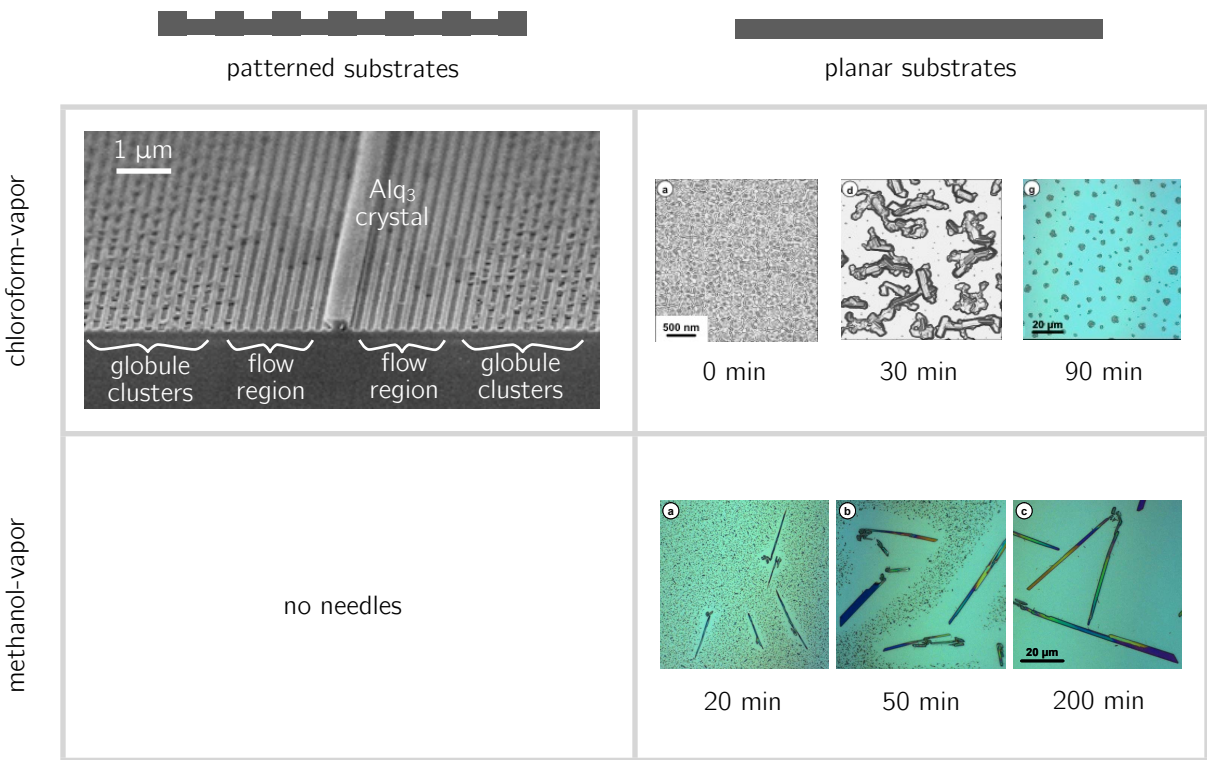


Figure 1-3: Experimental results from Mascaro [58]. Clockwise from top-left: 1) needle grown on patterned substrate during chloroform annealing, 2) small crystals grow and dissolve during chloroform annealing on planar substrates, 3) needle clusters growing on planar substrates during methanol annealing

Compared to flat substrates, the patterned substrates produced significantly-longer crystal needles. These needles grew in alignment with the square-groove pattern and spanned the length of the substrate (about 1 cm) with aspect ratios of more than 1000 to 1. On flat substrates, methanol-annealing produced long ($\sim 100 \mu\text{m}$), stable crystals. In contrast, chloroform-annealing produced smaller crystals, which later aggregated to form clusters and, at long times (approximately two hours), dissolved completely, as shown in Fig. 1-1.

1.3 Overview of thesis

In this thesis, we investigate the physical mechanisms governing the growth of Alq₃ needles from an amorphous thin film during solvent-vapor annealing. To that end, I examine the growth of needle-like crystals from a binary, fluid mixture through experiments, numerical modeling, and analytical scaling-laws. In particular, I develop a model of the general growth process as a function of substrate and solvent properties and compare this model to solvent-vapor-annealing experiments of Alq₃ on glass substrates. Modeling efforts, however, do not explore the condensation/adsorption of solvent or the solvent-Alq₃ interactions which lead to “melting” of the initially-solid thin film; changes in film morphology during solvent evaporation (as discussed in §1.2.1) are similarly ignored.

In Chapter 2 of this thesis, we review the physical processes in the solvent-vapor annealing experiment. Included in this overview is a review of the relevant literature. Chapter 3 describes the experimental setup and annealing procedure. These experiments produce real-time images of growing Alq₃ needles and measurements of needle lengths as a function of time. In Chapter 4, we model the system with a lubrication equation to describe the evolution of the thin liquid film and a convection-diffusion equation to describe the transport of Alq₃ and solvent within the thin film. Furthermore, we define a dimensionless transport coefficient, α , which describes the relative strength of diffusion and coarsening-driven convection. In Chapter 5, we derive analytical expressions for the dewetting and coarsening of the fluid film and scaling laws for the growth of needles. These scaling laws provide a physical understanding of needle growth in the diffusion-dominated and coarsening-dominated regimes. Chapter 6 presents and compares the results from experiments and simulations. In both experiments and simulations, we find that needle lengths grow as power-laws in time. In experiments, the growth exponent, γ , decreases with an increase in film thickness; in simulations, this thickness dependence maps to a variation in the transport coefficient, α . Finally, in Chapter 7, we review the primary results of this thesis and discuss future directions for this research.

Chapter 2

Physical Background

In this thesis, I grow single-crystal needles of Alq₃ using solvent-vapor annealing, as described in Chapter 3. The deposition of organic molecules has been studied elsewhere [33] and is not the focus of this thesis. Instead, we focus on what happens to the amorphous Alq₃ film upon exposure to solvent-vapor; the basic steps are as follows:

1. Solvent-vapor adsorbs onto the Alq₃ film and plasticizes it.
2. Fluid motion and diffusion transport solvent and Alq₃ through the film.
3. Alq₃-crystal needles nucleate and grow.

This thesis focuses on the motion of the fluid film, the transport of solvent/Alq₃, and the growth (but not nucleation) of needles. Nevertheless, this chapter reviews the physics of all the above steps. In addition to reviewing the physics of the system, this chapter provides a literature review for these various physical processes.

2.1 Solvent-vapor annealing

The as-deposited thin film of Alq₃ is an amorphous-solid, or glass [11]. During solvent-vapor annealing, solvent molecules adsorb onto and absorb into the glassy Alq₃-film. The addition of a low-molecular-weight additive (*i.e.*, the solvent) plasticizes the film by reducing its glass-transition temperature below room temperature.

2.1.1 Vapor equilibrium and diffusion

In a closed system, a condensed phase (*i.e.*, a liquid or solid) will vaporize until there is an equilibrium concentration of its vapor in the surrounding gas.¹ A vapor's concentration can be expressed in terms of its partial pressure

$$P_i = x_i P,$$

where P_i and x_i are the partial pressure and mole fraction of component i , and P is the total pressure of the gas. At equilibrium, the partial pressure of the vapor is equal to its saturated-vapor pressure (or equilibrium vapor pressure), P_i° .

In order to reach equilibrium, solvent-vapor near its liquid reservoir must be transported through the gas. For a small, closed system (like the annealing chamber in the present study), convection is limited, such that diffusion dominates the transport of solvent-vapor. Fick's second law describes diffusion of a component, A , with concentration c_A , as

$$\frac{\partial c_A}{\partial t} = D \frac{\partial^2 c_A}{\partial x^2}, \quad (2.1)$$

where D is the diffusivity (or diffusion coefficient) of A in air. Applying dimensional analysis to the diffusion equation, we find that diffusion carries particles a characteristic distance L over a time-scale

$$T = L^2/D. \quad (2.2)$$

2.1.2 Adsorption and condensation of solvent-vapor

In experiments, solvent-vapor is transported to and interacts with the Alq₃ film. This transport can occur by way of adsorption or condensation. Although these phenomena are closely

¹The term “gas” is preferred when a substance is in the gas phase at standard temperature and pressure; “vapor” is preferred when it is liquid or solid at standard temperature and pressure [29].

related, we will keep them distinct.² Adsorption³ is driven by the attraction of an adsorbate (*i.e.*, the adsorbing molecule) to a surface or interface; in contrast, condensation initiates when the vapor pressure is increased above the condensate's saturation pressure.

Adsorption

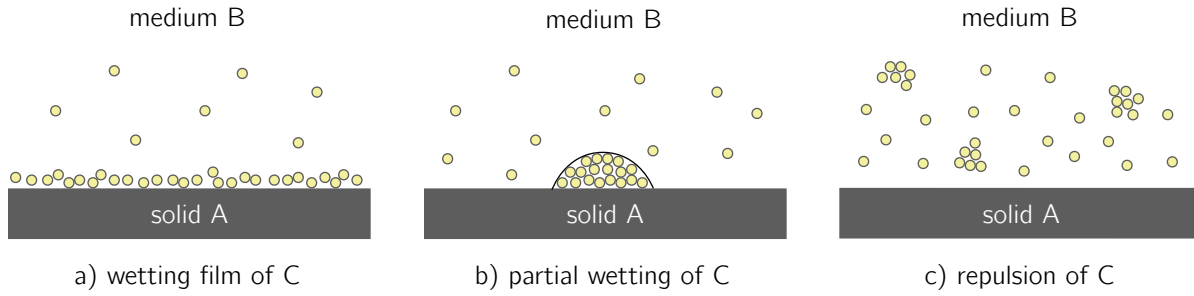


Figure 2-1: Wetting scenarios for molecules of C in a fluid B near a solid surface A. Adapted from Israelachvili [45, Fig. 9.5]

For a particle C in fluid media B in close proximity to solid A, the relative values of their interactions energies— u_A , u_B , and u_C for molecules A, B, and C—determine the behavior of the system [45]:

- a) *Adsorption*: If u_C is the intermediate energy (*i.e.*, $u_A \gtrless u_C \gtrless u_B$) particle C is attracted to the interface between A and B.
- b) *Partial wetting*: If u_A is the intermediate energy (*i.e.*, $u_B \gtrless u_A \gtrless u_C$) particles of C partially wet solid A.
- c) *Desorption*: If u_B is the intermediate energy (*i.e.*, $u_A \gtrless u_B \gtrless u_C$) particle C is repelled from the interface.⁴

²Adsorption and condensation are easily confused because their root words, adsorb and condense, are each used in descriptions of both adsorption and condensation. When a particle lands on an interface, it is adsorbed; for example, molecules can adsorb onto a solid surface to initiate condensation, or they can adsorb onto their own condensed phase. When a sufficient number of molecules adsorb onto a surface, it becomes a condensed phase.

³Adsorption and absorption are distinct processes: Adsorption is the attachment of atoms or molecules to an interface; absorption is the incorporation of those particles into the bulk phase (*i.e.*, away from the interface).

⁴Israelachvili [45, p. 145] gives a great example of how two attractive potentials (A-to-B and A-to-C) lead to repulsion: Wood is attracted to Earth by gravity. However, when water is introduced, wood is now repulsed, because water is denser than wood; *i.e.*, water is *more* attracted to Earth than the wood is.

These situations are described graphically in Fig. 2-1.

This energetic argument qualitatively describes the tendency for molecules to adsorb onto an interface. In practice, adsorption is described by adsorption isotherms, which relate the amount of adsorbed vapor (adsorbate) to the vapor pressure and the attraction of the adsorbate to the surface (see for example, the Langmuir and BET isotherms [75]). These descriptions of adsorption are applicable when the vapor pressure is below the saturated vapor pressure;⁵ above this point, condensation will dominate [26].

Condensation

Below a vapor's saturation temperature or above its saturated-vapor pressure, the vapor is supersaturated and favors the liquid state. The creation of a condensed phase, however, introduces an interface with an associated surface tension, which can either inhibit or promote condensation.

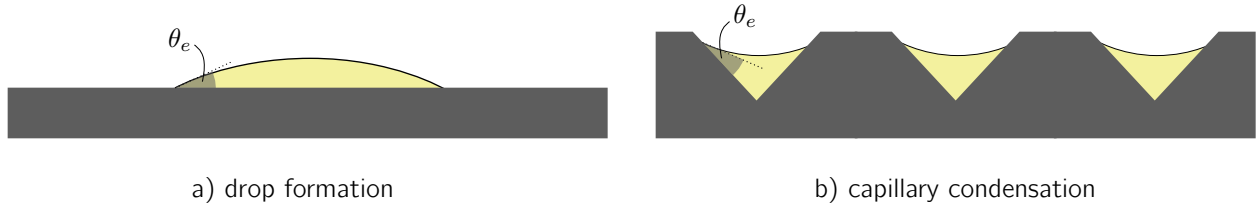


Figure 2-2: Supercritical and subcritical condensation regimes.

Partially-wetting fluids, will form drops on a flat surface, as shown in Fig. 2-2(a). Surface tension increases pressure in the drop relative to the surrounding vapor (see §2.2.3). This increased pressure inhibits condensation and leads to a critical supersaturation, above which condensation will occur [85, 27].

Conversely, partially-wetting fluids will fill capillaries and cavities in rough films and porous surfaces; the filling of an idealized, rough surface is shown in Fig. 2-2(b). This geometric effect can lead to low pressure in the fluid, such that condensation will initiate *below* the saturation pressure [26, 9]; this phenomenon is known as capillary condensation and is often discussed in conjunction with adsorption because of its dependence on surface

⁵In fact, many adsorption isotherms grow without bound as the pressure approaches the saturated vapor pressure.

properties (*i.e.*, its roughness).

This thesis does not attempt to model solvent condensation, but the interested reader can find other work on thin-film hydrodynamics with condensation (*e.g.*, [93]) and evaporation (*e.g.*, [44, 89, 100]).

2.1.3 Glass-transition and plasticization

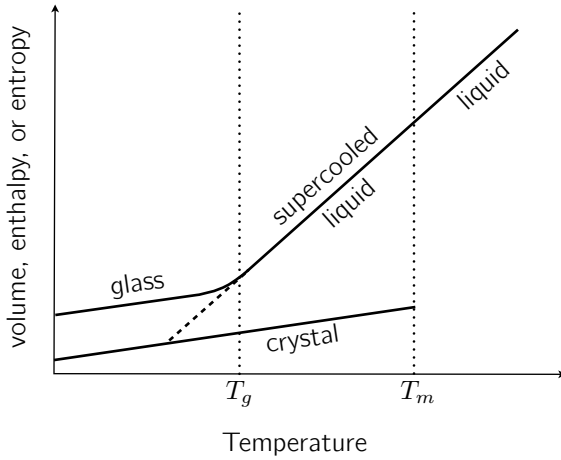


Figure 2-3: Schematic of phase diagram for glass transition. The structure of a crystalline solid is fundamentally different from that of a liquid, which leads to a jump in the volume, enthalpy, and entropy. An amorphous solid—*i.e.*, a glass—is structurally the same as a liquid and transitions smoothly from the liquid state. In reality, there are a range of possible glass-transition temperatures, which depend on the rate of cooling; this has been ignored to avoid complexity. Adapted from [11, 24].

In solvent-vapor experiments, the amorphous film of Alq₃ undergoes a glass transition upon exposure to solvent-vapor. The glass-transition is distinct from melting as it applies specifically to amorphous materials (whereas melting applies to crystalline materials) [2, 24]. A material can be simultaneously above its glass transition temperature and below its melting temperature, as shown in Fig. 2-3; in this state, a supercooled liquid can coexist with a crystalline solid. Since this supercooled phase is metastable, it will readily solidify if the crystal phase has nucleated.

An amorphous solid can be “melted” by raising its temperature above the glass-transition temperature, as discussed above; alternatively, introducing solvents, or other additives, can reduce the glass-transition temperature. In polymers, this reduction of the glass-transition temperature is known as plasticization [81]. The term plasticize has been extended to col-

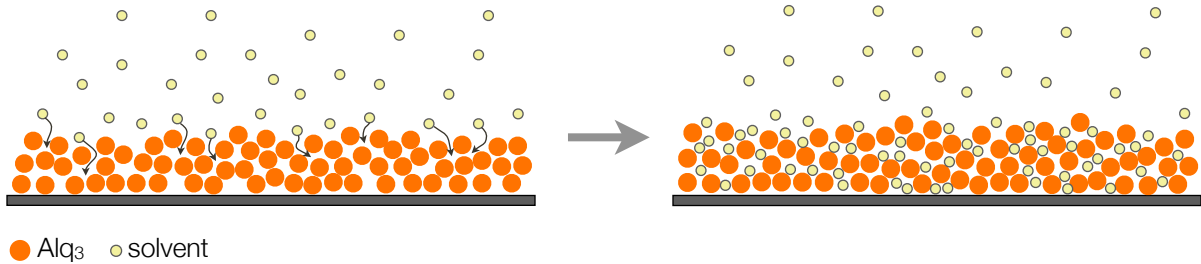


Figure 2-4: Schematic of absorption. Left: solvent molecules in the vapor work into the crevices of the Alq_3 film. Right: solvent molecules shield the cohesive forces between Alq_3 molecules, and dissolve the Alq_3 film.

loidal systems, where a mixture of particles of different sizes leads to an entropically-induced plasticization effect [40]. Qualitatively, the smaller molecules provide lubrication to the larger particles [32].

There exist many models for glass-transition [2, 46] and plasticization of polymers [6], colloids [32], and molecular glasses [105]. Previous analysis suggested that the glass-transition temperature for Alq_3 drops below room temperature when it has imbibed approximately 18% methanol by volume [58]; the actual mixing behavior, however, is dependent on the details of the interactions (*i.e.*, solubility) between Alq_3 and methanol. Such analysis is beyond the scope of this thesis.

In what follows, we assume that the Alq_3 film has absorbed sufficient methanol to become liquid; thus, evolution of the Alq_3 -and-methanol film is governed by the dynamics of thin, liquid films.

2.2 The physics of thin fluid films

From experimental observations, we know that solvent-vapor combines with Alq_3 to form a thin liquid film. This section reviews some basic physical concepts related to thin films. For a thorough review, see Oron, Davis, and Bankoff [74]; Craster and Matar [17]; and Thiele [47, Ch. 2].

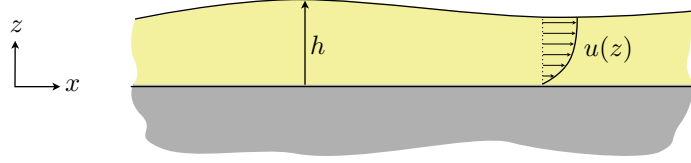


Figure 2-5: A thin liquid film bounded by a solid, no-slip surface on bottom and a free surface on top has a parabolic flow profile, as shown.

2.2.1 Thin-film evolution equation

For thin liquid films, the lubrication approximation (also known as the long-wave approximation) simplifies the Navier-Stokes equation to the thin-film evolution equation, in which viscous effects dominate over inertial effects. To describe the thin film, we define the local thickness of the film $h(x, y, z, t)$, where x and y are coordinates in the plane of the film, z is normal to the plane, and t denotes time. Conservation of mass gives⁶

$$\frac{\partial h}{\partial t} = -\underline{\nabla} \cdot \underline{Q}, \quad (2.3)$$

where $\underline{Q}(x, y, t)$ is the volumetric flux⁷ through the liquid film, and underbars denote vector quantities.

The lubrication approximation requires the characteristic film-thickness, H , to be much smaller than all relevant length scales, L , in the plane of the film—*i.e.*, $H \ll L$ —such that the Navier-Stokes equation is reduced to

$$\mu \frac{\partial^2 \underline{u}}{\partial z^2} = \underline{\nabla} p,$$

where μ is the viscosity of the liquid, $p(x, y, t)$ is the local pressure and $\underline{u}(x, y, z, t)$ is the local velocity.

The volumetric flux is found by integrating the parabolic velocity profile⁸ (see Fig. 2-5)

⁶The del operator, $\underline{\nabla}$, in the thin-film equations is a 2D operator in the plane of the film (*i.e.*, it operates in the x - and y -directions) because we have integrated over the z -direction. Often, this operator is denoted by $\underline{\nabla}_s$ (where “ s ” denotes surface).

⁷ \underline{Q} is actually the volumetric flux *per unit depth*.

⁸The parabolic velocity profile is a consequence of viscous flows and the application of free surface and no-slip boundary conditions on the top and bottom of the film.

across the film thickness, which gives

$$\underline{Q} = -\frac{h^3}{3\mu} \nabla p. \quad (2.4)$$

The negative sign reflects the fact that flow goes down pressure gradients, and the mobility, $h^3/3\mu$, suggests that flow is inhibited by thinner films and more viscous fluids. Gradients in pressure can arise from changes in film curvature (see §2.2.3 on surface tension), film thickness (see §2.2.4 on intermolecular pressure), or thermal/concentration gradients (see §C.3.1 on Marangoni effects).

2.2.2 Convection-diffusion equation for thin films

For a binary mixture of components A and B , the concentration of component A is described by a convection-diffusion⁹ equation:

$$\frac{\partial \phi_A}{\partial t} + \underline{\nabla} \cdot (\underline{u} \phi_A) = D \nabla^2 \phi_A, \quad (2.5)$$

where ϕ_A is the concentration of component A , \underline{u} is the velocity field, and D is the interdiffusivity of A and B . In this thesis, concentration has units of volume fraction,¹⁰ and we assume, for simplicity, that volume is not a function of concentration. Under these conditions, the concentration of component B is simply $\phi_B = (1 - \phi_A)$.

For thin films, we can simplify the convection-diffusion equation given by Eq. (2.5). If diffusion across the film thickness is much faster than flow in the plane of the film, then we can ignore variations of concentration across the film thickness. To estimate the relative speed of diffusion and flow, we nondimensionalize Eq. (2.5) to find that convection in the

⁹This equation is more-accurately called an advection-diffusion equation. Both convection and advection refer to transport by fluid motion. Convection, however, applies specifically to the transport of heat. In contrast, advection applies to the transport of any substance or conserved property. This thesis uses convection instead of advection simply because advection is less commonly used, even when more appropriate.

¹⁰The units of concentration are ambiguous. Most frequently, it has units of number density (number of atoms, molecules, or moles per unit volume), but it is also represented by number/mole fraction, volume fraction, mass density, and mass fraction [3]. To emphasize that concentration has units of volume fraction, we denote it by ϕ , as is common in problems in the literature (*e.g.*, [106]).

x -direction and diffusion in the z -direction are related by a modified Péclet number:

$$\text{Pe}' = \text{Pe} \left(\frac{H}{L} \right) = \frac{UH}{D} \left(\frac{H}{L} \right),$$

where U is the characteristic velocity in the plane of the film, H is the characteristic film thickness, and L is the characteristic length in plane of the film. For small values of Pe' (*i.e.*, $\text{Pe}' \ll 1$), diffusion across the film dominates such that ϕ_A is approximately invariant in the z -direction [60].

In the low Péclet-number limit, we follow the example of thin-film hydrodynamics (see §2.2.1) and integrate the convection-diffusion equation, Eq. (2.5), over the film thickness. Integration gives an evolution equation in terms of the mass of component A ,¹¹ $\phi_A h$, instead of the concentration, ϕ_A :

$$\frac{\partial(\phi_A h)}{\partial t} = -\underline{\nabla} \cdot \underline{J}_A, \quad (2.6)$$

where the flux of A , \underline{J}_A , is given by

$$\underline{J}_A = \phi_A \underline{Q} - Dh \underline{\nabla} \phi_A. \quad (2.7)$$

The right-hand-side denotes the flux of component A driven by fluid flow and diffusion. The negative sign on the diffusive term reflects the fact that components diffuses *down* concentration gradients.

Similar thin-film convection-diffusion equations are found in surfactant-laden thin-film flows (*e.g.*, [60]) and phase-separation in binary-mixtures with diffuse-interfaces (*e.g.*, [14, 15, 94, 69]). The convective-part of the equation is also common in particle-laden thin-film flows (*e.g.*, [106, 16]).¹²

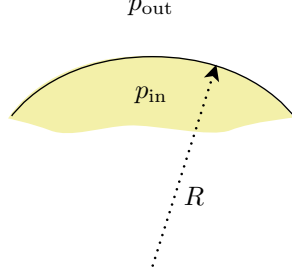


Figure 2-6: Surface tension produces a jump in pressure across a curved liquid-vapor interface. In general, a surface can have two independent curvatures, $1/R_1$ and $1/R_2$ (curvature out of the page not shown in schematic).

2.2.3 Surface tension

For a curved interface, surface tension produces a pressure jump across the interface, as given by the Young-Laplace equation [21]:¹³

$$p_{\text{in}} - p_{\text{out}} = \sigma \left(\frac{1}{R_1} + \frac{1}{R_2} \right), \quad (2.8)$$

where p_{in} and p_{out} are the pressures inside and outside the thin film, and $1/R_1$ and $1/R_2$ are the two principal curvatures of the interface. The above equation assumes positive curvature when the center of curvature is in the inner domain, as shown in Fig. 2-6.

For a nearly flat interface, we can approximate the total curvature as $1/R_1 + 1/R_2 \approx -\partial^2 h / \partial x^2 - \partial^2 h / \partial y^2$.¹⁴ To find the capillary pressure in the liquid film, let $p_{\text{out}} = 0$ (atmospheric) and $p_{\text{in}} = p$, such that

$$p = -\sigma \left(\frac{\partial^2 h}{\partial x^2} + \frac{\partial^2 h}{\partial y^2} \right). \quad (2.9)$$

¹¹Actually, $\phi_A h$ is the *volume per unit area* of component A .

¹²Note that the diffusive terms in Zhou, Bertozzi, and Hosoi [106] are from “gravity-driven” diffusion (in contrast to diffusion driven by concentration-gradients).

¹³Not to be confused with Young’s equation for contact angles of a liquid drop or with Laplace’s equation describing all sorts of equilibrium phenomena.

¹⁴The negative signs reflect the fact that the positive curvature depicted in Fig. 2-6 is concave down, which corresponds to a negative second derivative.

2.2.4 Intermolecular interactions

For a pair of molecules separated by a distance r , the Lennard-Jones potential describes the strength of their interaction as

$$V = - \left(\frac{A}{r^6} - \frac{B}{r^{12}} \right), \quad (2.10)$$

where A and B are constants proportional to the long-range attraction (van der Waals attraction) and short-range repulsion (steric effects) between the molecules. This interaction

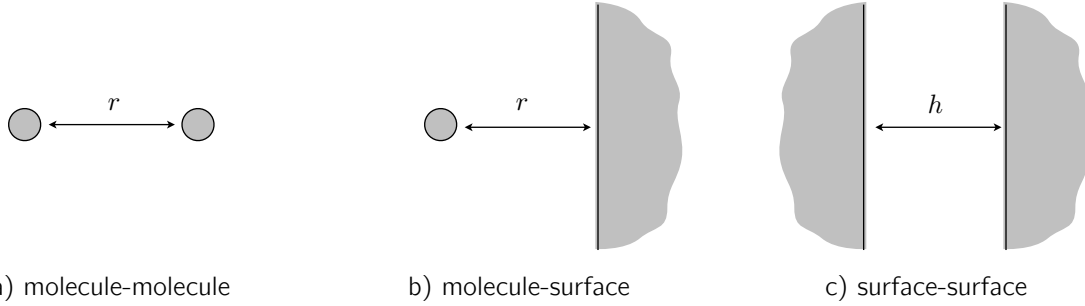


Figure 2-7: Intermolecular interactions between molecules and surfaces.

between individual molecules can be extended to surfaces (semi-infinite media). To calculate the interaction between a molecule and a surface (Fig. 2-7b), we integrate the potential over the volume of the medium, such that long-range attraction scales like r^{-3} , and short-range repulsion scales like r^{-9} . To find the interaction energy *per unit-area* between two surfaces separated by a height h (Fig. 2-7c), we integrate one more time (over the thickness of the second surface) to find

$$U \sim - \left(\frac{1}{h^2} - \frac{1}{h^8} \right). \quad (2.11)$$

Whereas V represents an intermolecular energy between two molecules, U represents an intermolecular energy *per unit area* between two surfaces. The change in exponents (from 6-12 to 2-8) means that intermolecular interactions between surfaces are significant for larger distances than for individual molecules [45]. For the experiments in this thesis, we have two semi-infinite domains (solid substrate and surrounding vapor) separated by a thin liquid film; in this case, intermolecular interactions—specifically van der Waals forces—are significant if the liquid film is between 10 and 100 nm thick [74].

Intermolecular pressure

Intermolecular interactions come into the thin-film equations as a pressure. The intermolecular pressure, Π , is related to the energy potential by $\Pi = \partial U / \partial h$; thus, the intermolecular pressure corresponding to the Lennard-Jones potential scales as h^{-3} and h^{-9} .

Note that the Lennard-Jones potential, Eq. (2.10), describes long-range van der Waals attraction and short-range Pauli repulsion.¹⁵ The general form for an intermolecular pressure combining long-range attraction and short-range repulsion is given by

$$\Pi(h) = \frac{a_n}{h^n} - \frac{a_m}{h^m}. \quad (2.12)$$

The power of the exponents in Π can be associated with various physical effects, as summarized in Tbl. 2.1. In this thesis, we assume that the coefficients a_n and a_m are invariant, such that the substrate and liquid properties are uniform.¹⁶ The intermolecular potential¹⁷ corresponding to Eq. (2.12) is expressed as

$$U = -\frac{a_n}{(n-1)h^{n-1}} + \frac{a_m}{(m-1)h^{m-1}}.$$

This intermolecular potential, and its corresponding pressure, are plotted in Fig. 2-8.

When the pressure given by Eq. (2.12) has only a single term (either attractive or repulsive), it is called the disjoining pressure, as introduced by Derjaguin in 1939 [25]. When the pressure combines attractive and repulsive terms, it can be dubbed the disjoining pressure [38], generalized disjoining pressure [74], disjoining-conjoining¹⁸ pressure [73, 39], thermomolecular pressure [101], or intermolecular pressure [84]. This thesis uses the term intermolecular pressure.

Although some investigations examine the film evolution due to a single attractive or repulsive term in the intermolecular pressure, the present study requires both attractive

¹⁵Note that the r^{-12} exponent is semi-empirical and was originally chosen because it is computationally-convenient (since it is the square of r^{-6}).

¹⁶Variations in substrate properties can cause interesting dewetting phenomenon, as discussed in [82, 48, 47].

¹⁷Some papers refer to the intermolecular pressure as “intermolecular potential” (*e.g.*, [48]); here intermolecular potential refers to an energy potential.

¹⁸Where “disjoining” refers to the repulsive term and “conjoining” refers to the attractive term.

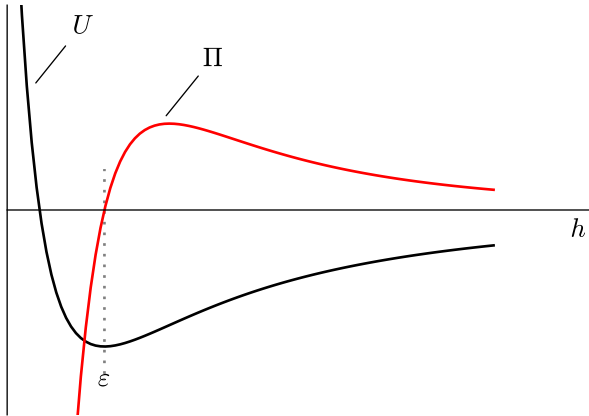


Figure 2-8: Intermolecular potential and pressure

term	description
h^{-1}	hydrogen-bonding-dependent structural contribution [90]
h^{-2}	ion-electrostatic, overlapping double-layer contribution [90]
h^{-3}	van der Waals (dispersion) force [38, 39, 90],
h^{-4}	short-range repulsion [38] and retarded van der Waals force [20, 82]
h^{-9}	short-range repulsion conjugate to r^{-12} term of Lennard-Jones potential [38].
$\exp(h/l)$	polar (double-layer) interactions [20, 13].

Table 2.1: Physical interpretation of terms in intermolecular pressure

and repulsive terms.¹⁹ Without attractive interactions, there is no instability in the film. Without a repulsive term, the system cannot be modeled using hydrodynamics, since a purely attractive term would become singular as the film dewets²⁰ [82]. In contrast, when both attractive and repulsive terms are present, “dewetting” produces drops separated by an ultra-thin liquid film.

¹⁹When the intermolecular potential is purely attractive, one can study the evolution of the thin film up to the point of dewetting (but not its evolution after dewetting); *e.g.*, Kao, Golovin, and Davis [48]. When the potential is purely repulsive, gravity will limit the growth of this repulsive potential; *e.g.*, de-Gennes [20] and Bonn *et al.* [9].

²⁰A purely attractive intermolecular potential would reduce the film thickness to zero, but since the potential scales as h^{-n} , it blows up as $h \rightarrow 0$.

Equilibrium film thickness, ε

At a film thickness $h = \varepsilon$, long-range attraction balances short-range repulsion leading to a minimum in energy, such that $\partial U/\partial h = 0$. At this equilibrium film thickness, the intermolecular pressure is zero, as shown in Fig. 2-8.

We can rewrite Eq. (2.12) in terms of ε as follows:

$$\Pi(h) = \kappa \left[\left(\frac{\varepsilon}{h} \right)^n - \left(\frac{\varepsilon}{h} \right)^m \right], \quad (2.13)$$

where h is the height of the film. Using the fact that the intermolecular pressure is zero at $h = \varepsilon$, we find that (see Gomba and Homsy [39] for a detailed explanation)

$$\varepsilon = \left(\frac{a_m}{a_n} \right)^{1/(m-n)}.$$

Combining this expression for ε with Eq. (2.12) and Eq. (2.13) allows us to write κ in Eq. (2.12) as

$$\kappa = \left(\frac{a_m^n}{a_n^m} \right)^{1/(n-m)} = \frac{a_n}{\varepsilon^n}. \quad (2.14)$$

Hamaker constant

Van der Waals interactions are represented by an intermolecular pressure that scales as h^{-3} and has a coefficient

$$a_3 = A_{132}/6\pi, \quad (2.15)$$

where A_{132} is the Hamaker constant for phases 1 and 2 separated by a thin layer of phase 3 [45]. The Hamaker constant captures the polarizabilities and geometry of the three phases. If phase 2 is vapor, then its Hamaker constant is $A_{22} = 0$, such that the combining relations (see Israelachvili [45]) simplify to

$$A_{132} = \sqrt{A_{33}}(\sqrt{A_{33}} - \sqrt{A_{11}}).$$

Thus, A_{132} is positive—and van der Waals interactions are attractive—if $A_{11} < A_{33}$. In this thesis, we denote the Hamaker constant as A_{SLV} for a solid substrate and a vapor separated

by a thin liquid film.

The magnitude of A_{SLV} is typically 10^{-20} to 10^{-19} J, but this value can be either positive or negative. Unfortunately, the literature is not consistent on whether a positive or negative Hamaker constant reflects an attractive or repulsive intermolecular potential, as described in the following section.

A note on the sign of the intermolecular pressure

The literature is not at all consistent in derivations of intermolecular interactions. The literature disagrees on

- whether a positive Hamaker constant, A_{SLV} , denotes attraction or repulsion
- the sign relating the energy potential and the Hamaker constant, $U \sim \pm A_{\text{SLV}}$
- the sign relating the pressure and energy, $\Pi \sim \pm U$
- the sign relating the intermolecular pressure and liquid pressure, $p_{\text{liquid}} \sim \pm \Pi$

These sign differences can be separated into two cases:²¹

1. attractive A_{SLV} , $U \sim -A_{\text{SLV}}$, $\Pi \sim \frac{\partial U}{\partial h}$, $p_{\text{liquid}} \sim \Pi$
2. repulsive A_{SLV} , $U \sim A_{\text{SLV}}$, $\Pi \sim -\frac{\partial U}{\partial h}$, $p_{\text{liquid}} \sim -\Pi$

The first case encompasses books and papers by Israelachvili [45, Ch.11]; Glasner and Witel斯基 [38]; Oron and Bankoff [73]; Kao *et al.* [48]; and Wettlaufer and Worster [101]. The second case of sign conventions is used in de Gennes *et al.* [21, Ch.4]; de Gennes [20]; and Bonn *et al.* [9].

There are two main sources for the sign differences in the literature. First, the disjoining pressure was introduced by Derjaguin [25] to describe the thickening of adsorbed films due to intermolecular interactions. In this case, a positive disjoining pressure—as the name suggests—arises from repulsive intermolecular interactions. These interactions, however,

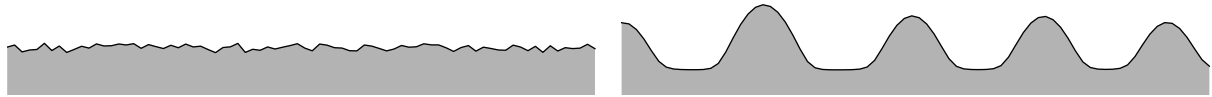
²¹Gomba and Homsy [39] is an outlier: $\Pi \sim -\frac{\partial U}{\partial h}$ and $p_{\text{liquid}} \sim -\Pi$ like case 2, but the Hamaker constant is attractive.

necessitate a negative liquid pressure (see Fig. 2-8); thus, “disjoining pressure” and pressure would have opposite sign.

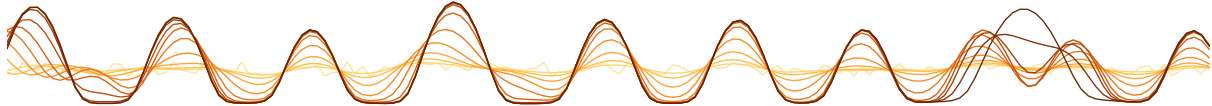
A second source of confusion arises because it is unclear what body the intermolecular pressure acts on (*i.e.*, action-reaction pairs). For example, Wettlaufer and Worster [101] refer to the intermolecular pressure²² as the pressure exerted by intermolecular interactions *on* the liquid. By Newton’s third law, the pressure *in* the liquid must be equal and opposite; thus, intermolecular pressure can refer to the pressure exerted *by* the liquid on the surrounding environment.

In this thesis, intermolecular pressure refers to the pressure *in the liquid* due to intermolecular interactions, and a positive A_{SLV} denotes an attraction between surfaces.

2.2.5 Dewetting fluid films



(a) A thin liquid film with an initially uniform, but rough, rough thickness (left) dewets to form drops separated by an ultra-thin film.



(b) Time-lapse plot (strobe plot) of the thickness profile as the liquid film breaks up in to drops. Lighter and darker colors suggest earlier and later times, respectively.

Figure 2-9: Dewetting instability of thin liquid films

The competition between intermolecular forces and surface tension drives the initially-uniform film toward the formation of drops, as shown schematically in Fig. 2-9. Micrographs from experiments also show drop-like regions far from needles (*e.g.*, the right side of Fig. 1-1). This dewetting process has been investigated both theoretically [83, 72, 4, 38] and experimentally, for both polymer films [80, 104, 52, 4, 8], and metallic films [7]). Two qualitatively different regimes of dewetting are discussed below: spinodal dewetting and

²²Actually, what I call the intermolecular pressure they call the thermomolecular pressure.

nucleation-driven dewetting.

Spinodal dewetting

For an initially-uniform (but rough) thin film, the attractive term in the intermolecular pressure, Eq. (2.13), drives slightly-thinner regions toward the substrate. When the equilibrium thin-film thickness, ε , is below a critical value, the initially-uniform liquid film is unstable and will break up into droplets separated by an ultra-thin film [38, 74]; this thinning instability is known as dewetting.²³ From linear-stability analysis, the wavelength for the instability—*i.e.*, the spacing between drops—is given by $\lambda \sim h_0^2$ and grows over a characteristic time $\tau \sim h_0^5$ [82] (these relations will be derived in detail in §5.1.1).

Because of the similarities between the thin-film equation and the Cahn-Hilliard equation, many researchers have taken to calling this dewetting instability “spinodal-dewetting”, as an analogy to “spinodal-decomposition”.²⁴ Similarities and differences between these equations and dewetting/decomposition are discussed in [65, 73, 38, 93].

Nucleation-driven dewetting

Since spinodal dewetting grows with a characteristic time that scales as h_0^5 , the dewetting instability is slow to develop for thick films. As a result, finite perturbations in the initial film thickness can trigger the nucleation of holes [95, 92, 4, 82]. The growth of these holes can further trigger a cascade of drops and holes, as shown in Fig. 2-10.

This nucleation of holes is analogous to the nucleation of phases in phase separation, just as spinodal dewetting is analogous to spinodal decomposition. A brief discussion of these similarities is provided in §A.1.

²³Although this process is called “dewetting”, there is still a fluid layer connecting adjacent droplets. In fact, I even call this ultra-thin film a “wetting layer”.

²⁴The term “spinodal” refers to the curve where the curvature of the free energy goes to zero and separates meta-stable regions (where nucleation drives phase-separation) and unstable regions (where infinitesimal perturbations drive phase-separation). The etymological origin of the term comes from “spinode”, *i.e.*, a cusp. If the free energy is plotted as functions of volume and entropy, it forms a cusp at the spinodal [10].

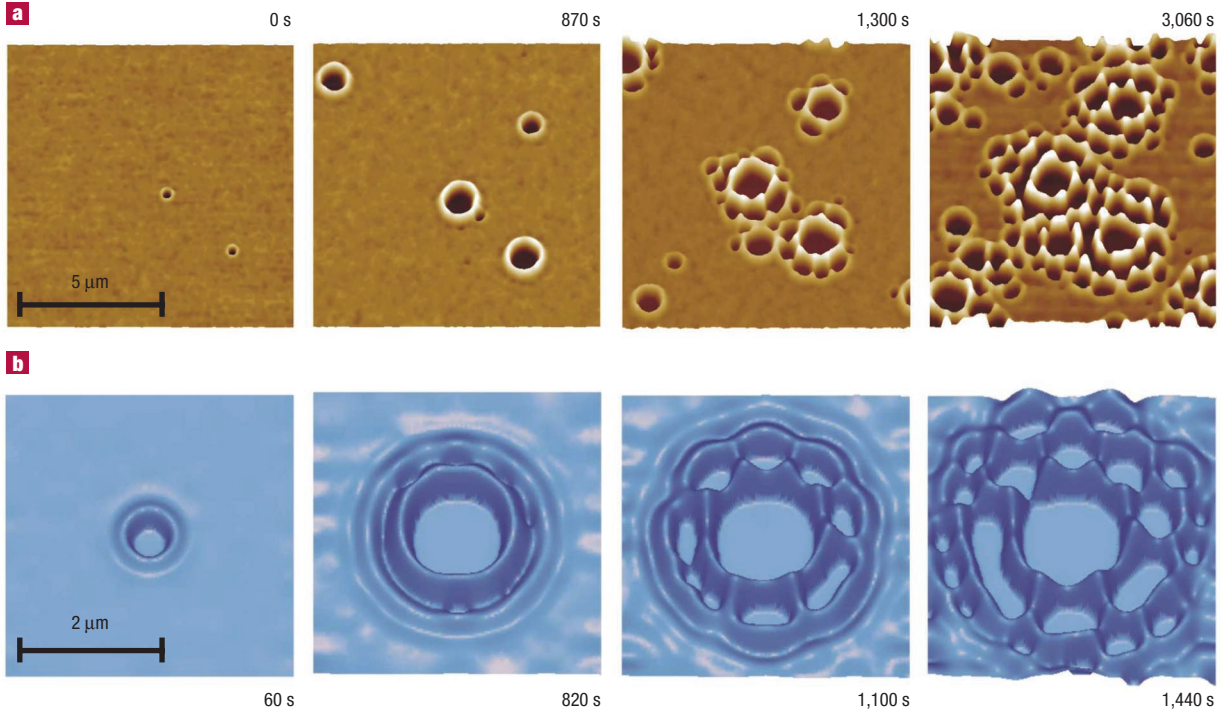


Figure 2-10: Hole formation from Becker *et al.* [4]. The top sequence shows AFM images of a 4.9 nm thick polystyrene film dewetting from a silicon substrate. The bottom sequence shows a numerical simulation with properties matching the experiments.

2.2.6 Drop coarsening

After a uniform film breaks up into drops, surface tension drives small, finely-spaced drops toward the formation of larger, coarsely-spaced drops, as described theoretically in [38] and measured experimentally in [54, 8]. This coarsening process can occur through either coalescence or collapse of drops [37]—also dubbed drop migration and Ostwald ripening, respectively [36]. In dynamic coalescence, drops migrate toward each other until they collide and merge; while in Ostwald ripening, pressure differences between adjacent drops drive flow through the ultra-thin film connecting adjacent drops.²⁵ These two methods of coarsening are illustrated in Fig. 2-11.

In §5.1.2, we reproduce scaling laws for coarsening that were originally derived by Glasner and Witelski [38].

²⁵Flow through the ultra-thin film is also (confusingly) dubbed diffusion-driven mass transfer [37].

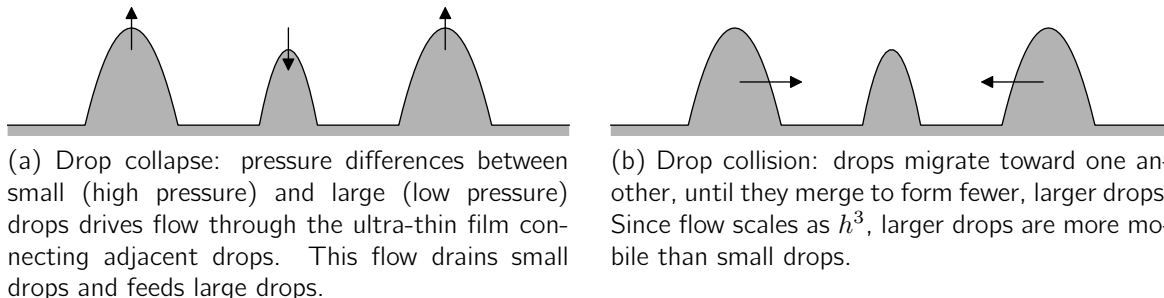


Figure 2-11: Schematic of drop collapse and collision. Reproduced from [37, Fig. 13]

2.3 Nucleation and solidification

After plasticization, Alq₃ can crystallize into a more energetically-favorable state (see Fig. 2-3). Hence, when an Alq₃ molecule is transported to the vicinity of a nucleated needle, it will bind to the crystal and expel its no-longer-needed solvent molecules. In analogy to thermally-driven solidification, solvent concentration plays the role of thermal energy and solvent that is expelled during crystallization plays the role of latent heat [53].

2.3.1 Nucleation of solids

When a liquid is supercooled, it is (by definition) energetically-favorable for the liquid to solidify. This driving force is quantified by Δf : the *bulk* free-energy²⁶ change per unit volume going from liquid to solid. Since the system tends toward lower energy, Δf must be negative for solidification to be favorable.

But supercooling alone is not sufficient for solidification because a small seed of solid will entail an energetic penalty for its liquid-solid interface; this penalty is proportional to the interfacial energy,²⁷ σ . Thus, for a solid nucleating from its liquid phase, the total free-energy change for nucleation is given by [3, §19.1]

$$\Delta\mathcal{F} = V\Delta f + S\sigma, \quad (2.16)$$

²⁶The qualification “bulk”, in “bulk free-energy”, implies that we ignore the energy costs of creating an interface.

²⁷Interfacial energy, surface energy, and surface tension are equivalent concepts and have units of energy per unit area. In practice, surface tension usually specifies liquid/vapor interfaces, while surface energy applies to either liquid/vapor or solid/vapor interfaces; interfacial energy is preferred for all other interfaces (*e.g.*, an interface between two phases in an alloy).

where V is the volume of the solid phase and S is the surface area of the solid/liquid interface. This energy expression suggests that small seeds will dissolve because of a high surface-to-volume ratio, while large seeds are energetically-favorable and will grow.

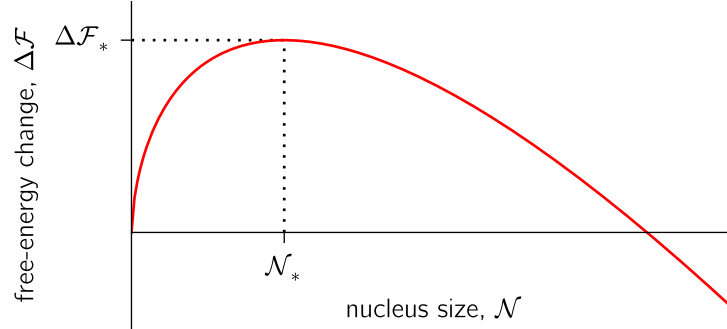


Figure 2-12: Total-free-energy change vs. the nucleus size

For a nucleated cluster with size N (*e.g.*, the number of molecules in the cluster), the *total* free-energy change is

$$\Delta\mathcal{F} \approx N\Delta f + N^{2/3}\sigma,$$

where the volume and surface-area of the cluster scale as N and $N^{2/3}$. This free-energy change is plotted in Fig. 2-12.

The nucleated cluster will grow if adding a molecule to it lowers $\Delta\mathcal{F}$; thus, the critical nucleus size, N_* , maximizes the total free energy change, as shown in Fig. 2-12, and the critical free-energy change is $\Delta\mathcal{F}_* \equiv \Delta\mathcal{F}(N_*)$. Thermal motion in the liquid allows the formation of solid seeds despite positive (*i.e.*, unfavorable) energy change. From empirical studies, nucleation is observable if the critical nucleation energy is $\Delta\mathcal{F}_* \lesssim 76 k_B T$, where $k_B T$ captures the thermal energy at temperature T and k_B is Boltzmann's constant.

A thorough review of nucleation phenomena is provided in Balluffi *et al.* [3, Ch. 19] and Kelton [50].

2.3.2 Interface equilibrium

For all but the fastest growing solids, local equilibrium applies at the interface, and solidification is diffusion limited [3].²⁸ At local equilibrium, the temperature at the interface is fixed at the melting temperature T_m for thermally-driven solidification; while for phase-separation-driven solidification, the concentration is fixed at ϕ_{solid} and ϕ_{tip} on the solid and liquid sides of the interface [53], as shown in Fig. 2-13. In this thesis, ϕ_{solid} is small (Alq₃-rich), and ϕ_{tip} is comparatively large (solvent-rich).

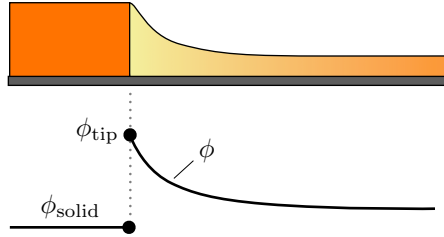


Figure 2-13: Local thermodynamic equilibrium fixes the concentration on the solid and liquid sides of the solid/liquid interface.

2.3.3 Interface growth velocity (the Stefan Condition)

For diffusion-limited solidification, growth of the interface is governed by the Stefan condition. In the following, we restrict discussion to solidification due to species diffusion.²⁹

The Stefan condition is essentially an expression of conservation of mass and relates the interface position to the fluxes in and out of the interface [3, §20.1.1]. Consider a one-dimensional crystal with height h_{solid} and solvent concentration ϕ_{solid} growing at velocity v_n normal to the interface. Over a time Δt , the growing crystal absorbs material with a concentration ϕ_{solid} and rejects material with a concentration ϕ_{tip} , such that

$$\Delta m_{\text{crystal}} = v_n(\phi_{\text{solid}} - \phi_{\text{tip}})h_{\text{solid}}\Delta t.$$

This mass must be supplied/rejected by flux into/out-of the interface. Assuming flux is only

²⁸If the interface is not at equilibrium, growth is limited by the rates at which atoms can be absorbed or emitted. This phenomenon is known as interface-limited growth (see *e.g.*, [3, §20.2.2]).

²⁹Alternatively, the Stefan condition can be derived for thermally-driven solidification.

due to diffusion through the liquid, we find³⁰

$$v_n(\phi_{\text{solid}} - \phi_{\text{tip}})h_{\text{solid}}\Delta t = - \left(-D \frac{\partial \phi}{\partial n} h_{\text{solid}} \Delta t \right),$$

where D is the diffusivity of solvent through the liquid and $\partial\phi/\partial n$ is the concentration gradient normal to the interface. Note: the above assumes that the height of the liquid, at the solid/liquid interface, matches that of the solid (for a discussion of this assumption, see §6.6.5). Rearranging the equation above gives the solidification velocity

$$v_n = \frac{D}{(\phi_{\text{solid}} - \phi_{\text{tip}})} \frac{\partial \phi}{\partial n}. \quad (2.17)$$

³⁰The minus sign inside the parentheses on the right-hand-side, arises because diffusion goes down concentration gradients; the second minus sign arises because growth requires flux *toward* the interface, opposite the direction of growth.

Chapter 3

Experiments

This chapter describes solvent-vapor annealing experiments, which promotes the growth of Alq₃ needles (as shown in Fig. 3-1) from amorphous thin-films of Alq₃.



Figure 3-1: Micrograph of region around Alq₃ needle after annealing. Experiments show three regions of interest (from left to right): 1) single-crystal needles of Alq₃, 2) thin wetting films surrounding needles (featureless regions), and 3) droplet regions.

3.1 Experimental procedure

The experimental procedure used to grow Alq₃ needles is outlined in Fig. 3-2. Before deposition, half-inch-square glass substrates were cleaned according to the procedure described in §C.4. Next, thin, amorphous Alq₃-films, 15–60 nm-thick, were evaporated onto the glass-substrates at low pressure ($< 10^{-6}$ Torr) with deposition rates of 1.5–2.5 Å/s. After deposition, the substrates—along with a container of methanol—were placed in a sealed chamber at room temperature and pressure, for 1–3 hours. During this annealing period, a small area of the substrate (1.4×1 mm) was imaged using an optical microscope.

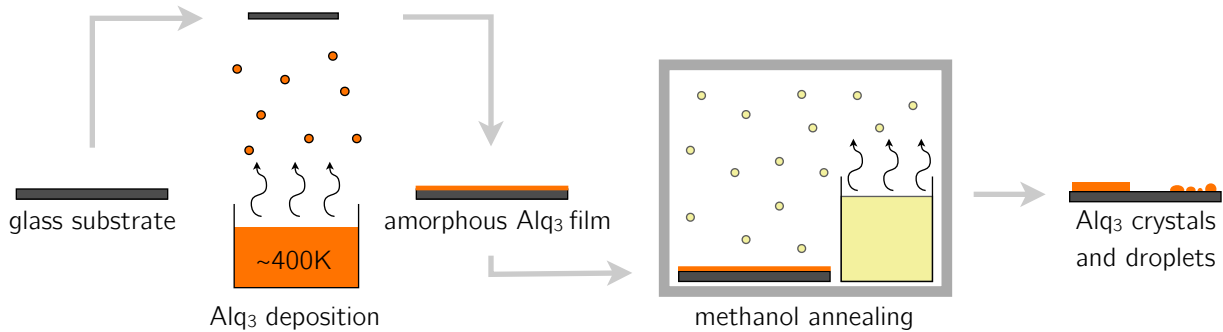


Figure 3-2: Growth of Alq₃ needles: a thin, amorphous film of Alq₃ is evaporated onto a half-inch-square glass substrate. The substrate is then placed in a sealed chamber along with a container of methanol. The solvent-vapor fills the chamber and interacts with the Alq₃ film to produce droplets and needles.

parameter	value
Alq ₃ deposition rate	1.5–2.5 Å/s
Alq ₃ film thickness	15–60 nm

Table 3.1: Experimental parameters

3.2 Annealing chamber

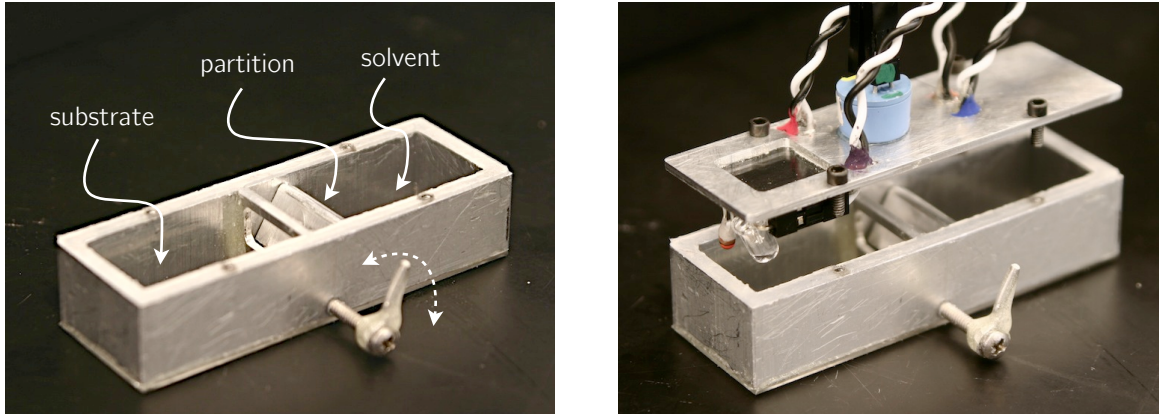


Figure 3-3: Annealing chamber with separate compartments for the substrate and solvent. A movable partition separates the compartments. The lid of the chamber has four electrical connectors for sensors and other electrical components.

The annealing chamber was built from a section of 3×1 inch extruded aluminum tubing with 1/8-inch-thick walls. As shown in Fig. 3-3, the chamber is divided into two equally-sized compartments: one for the substrate and one for the solvent. A glass cover slip was glued onto the bottom of the chamber with a solvent-resistant epoxy, JB Weld™.

A removable lid was fabricated from a 1/16-inch-thick aluminum plate and is attached

to the chamber body by four $2\text{-}56 \times 1/4$ inch hex screws. The lid has a glass viewport on the substrate side and four electrical connectors: two on the substrate side and two on the solvent side. The glass viewport and glass bottom-plate allow imaging of substrates during solvent-vapor annealing. Thermistors connected to the lid measured the temperature in each compartment, and a UV LED¹ illuminates the substrate.²

The solvent- and substrate-sides of the annealing chamber are separated by a movable partition. The partition is hinged with a $5\text{-}40 \times 1.5$ inch bolt, which extends outside of the chamber.³ A small lever-arm attached to the bolt facilitates opening and closing the partition. Four neodymium magnets attached to the partition⁴ ensure a tight seal between the solvent- and substrate-sides of the annealing chamber when the partition is closed.

3.3 Solvent-annealing setup

Since methanol vapors are toxic [1], solvent is added to the annealing chamber in a fume hood. After, adding a glass substrate (with the Alq₃ thin film facing up), the lid is attached to seal the chamber. Note that, the partition between the solvent- and substrate-sides of the annealing chamber should be closed to reduced solvent-annealing during this set-up phase.

After sealing the chamber, it is moved from the fume hood to a NikonTM TE2000-U microscope, as shown in Fig. 3-4. Images of the substrate are captured by a camera (AbrioTM imaging system with 1392×1024 pixel resolution) affixed to the microscope. Substrates were typically annealed for 1–3 hours, although some annealing experiments lasted almost two days.

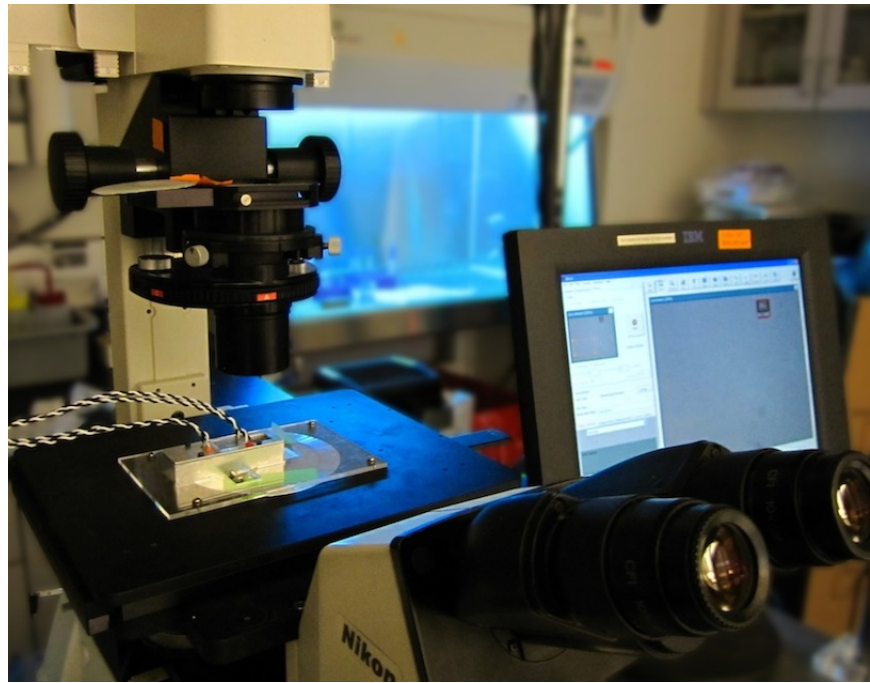


Figure 3-4: Experimental setup: annealing chamber placed under a microscope during annealing. A camera is affixed to the microscope, and the output is displayed on a computer monitor (right).

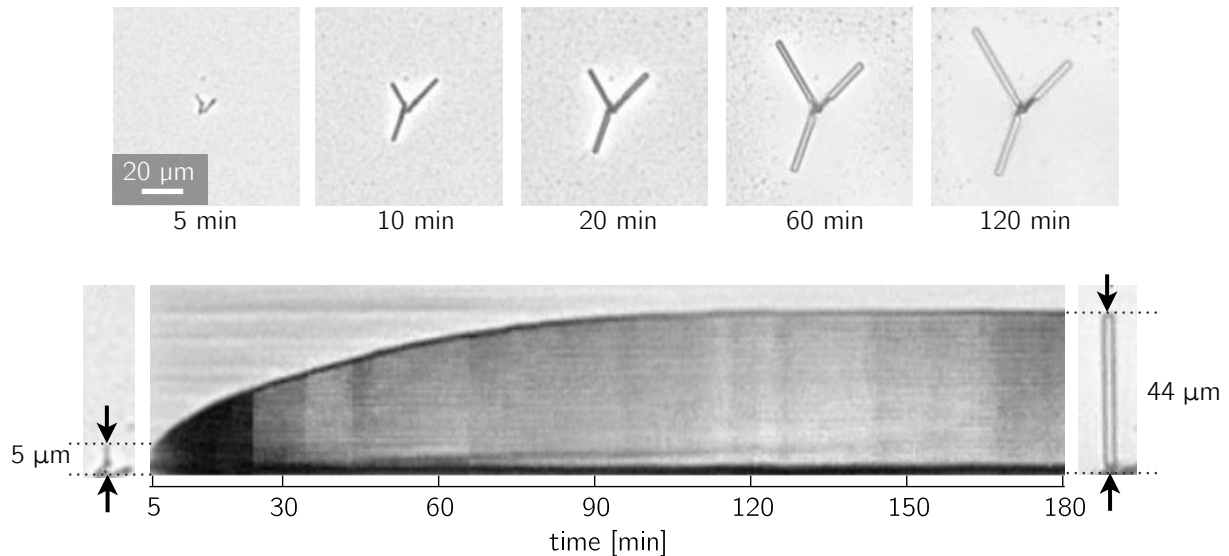


Figure 3-5: Top: cluster of needles growing during solvent-annealing. Top-left needle from the cluster is tracked over time in bottom image. Bottom: slice of micrograph-pixels along the axis of a needle as a function of time. The dark curved line is the tip of the needle as a function of time and shows the needle growing from $5\text{ }\mu\text{m}$ to $44\text{ }\mu\text{m}$ over the course of the 3 hour anneal. To the left and right of the pixel-slice plot are images of the needle 5 minutes and 180 minutes into the annealing process; the arrows are aligned with the pixel-slice for those image-frames.

3.4 Needle-length measurements

The length of a needle can be tracked in experiments by taking a 1D-slice of pixels along the needle's long-axis. When sequential pixel-slices are placed side-by-side, we can easily visualize the evolution of the needle length. The dark, curved line in the bottom image of Fig. 3-5 gives the position of the needle tip as a function of time. Since the pixel-slices start at the base of the needle, the height of the tip corresponds to the length of the needle.

¹ultra-violet light-emitting-diode

²Alq₃ fluoresces in UV light (by emitting light in the green spectrum). This UV LED was not used during normal experiments.

³Using a bolt as a hinge is a simple way to ensure a good seal (with the aid teflon tape) because of the tight tolerance between bolts and drill taps.

⁴Two magnets are placed near the top of the movable partition, and two more are placed near the top of the fixed partition.

Chapter 4

Mathematical model of thin-film crystal growth

This chapter describes the evolution equations for a thin film with dimensionless thickness, h , and dimensionless solvent-concentration, ϕ , as shown in Fig. 4-1.

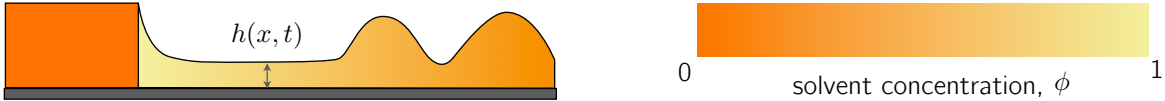


Figure 4-1: Schematic of thin film with thickness, h , and solvent-concentration, ϕ

To reduce the number of parameters in the problem, we nondimensionalize equations by the fluid viscosity, μ ; fluid density, ρ ; interdiffusivity of solvent and Alq₃, D ; a characteristic length in the x -direction, L ; and the initial thin-film thickness, \tilde{h}_0 . In what follows, tildes (*e.g.*, \tilde{h}) denote dimensional counterparts to dimensionless variables, which are defined in Tbl. 4.1.¹

¹Note that this convention applies to all following chapters, but not the preceding chapters. In particular, equations presented in Chapter 2 are dimensional (but are not denoted by tildes).

physical variable	dimensionless expression
time	$t = \frac{\tilde{t}}{\rho \tilde{h}_0 L / \mu}$
spacial coordinate	$x = \frac{\tilde{x}}{L}$
film thickness	$h = \frac{\tilde{h}}{h_0}$
equilibrium thickness	$\varepsilon = \frac{\tilde{\varepsilon}}{h_0}$
fluid velocity	$u = \frac{\tilde{u}}{\mu / \rho h_0}$
pressure	$p = \frac{\tilde{p}}{3\mu^2 L / \rho \tilde{h}_0^3}$
solvent concentration	$\phi = \frac{\tilde{\phi} - \tilde{\phi}_{\text{solid}}}{\tilde{\phi}_{\text{tip}} - \tilde{\phi}_{\text{solid}}}$

Table 4.1: Dimensionless variables in the mathematical model. Note that tildes denote dimensional variables, and variables to the right of a slash (/) are in the denominator (in contrast to the normal order of operations).

4.1 Thin-film evolution equation

For one-dimensional flow, conservation of mass for the fluid film—described by Eq. (2.3)—can be simplified to

$$\frac{\partial h}{\partial t} = -\frac{\partial Q}{\partial x}. \quad (4.1)$$

Similarly, the fluid flux—described by Eq. (2.4)—can be simplified to

$$Q = -h^3 \frac{\partial p}{\partial x}. \quad (4.2)$$

Note that the expression above is dimensionless, such that viscosity has been scaled out of the equation.

Substituting Eq. (4.2) into Eq. (4.1) gives a dimensionless equation for the evolution of the thin, fluid film:

$$\frac{\partial h}{\partial t} = \frac{\partial}{\partial x} \left(h^3 \frac{\partial p}{\partial x} \right). \quad (4.3)$$

4.2 Solvent-mass evolution equation

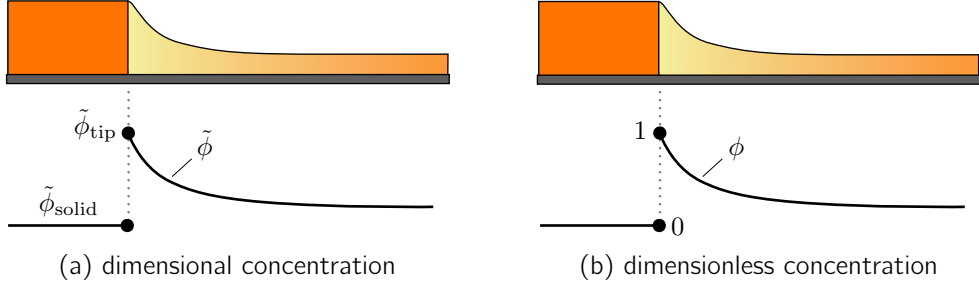


Figure 4-2: Local solvent concentration near the needle tip. The needle is Alq₃-rich and thus, a low solvent concentration $\tilde{\phi}_{\text{solid}}$. When the concentration is nondimensionalized, as shown in Tbl. 4.1, the concentration goes to 1 on the liquid side of the needle tip and 0 in the solid.

The dimensionless solvent-concentration, ϕ , is defined in Tbl. 4.1 and shown schematically in Fig. 4-2. For one-dimensional flow, conservation of mass for the solvent—described by Eq. (2.6)—can be simplified to

$$\frac{\partial(\phi h)}{\partial t} = -\frac{\partial J}{\partial x}, \quad (4.4)$$

and the solvent flux, given by Eq. (2.7), becomes

$$J = \phi Q - \mathcal{D}h \frac{\partial \phi}{\partial x}. \quad (4.5)$$

Note that these dimensionless equations assume that *volume is not concentration dependent*, as discussed in 2.2.2. The dimensionless diffusivity (*i.e.*, diffusion coefficient), \mathcal{D} , is

$$\mathcal{D} = \frac{\rho D \tilde{h}_0}{\mu L}, \quad (4.6)$$

where D , ρ , and μ are the diffusivity, density, and viscosity of the fluid.

Substituting Eq. (4.5) into Eq. (4.4) gives a dimensionless equation for the evolution of solvent mass:

$$\frac{\partial(\phi h)}{\partial t} = \frac{\partial}{\partial x} \left(\phi h^3 \frac{\partial p}{\partial x} + \mathcal{D}h \frac{\partial \phi}{\partial x} \right). \quad (4.7)$$

4.3 Pressure in the thin liquid film

Pressure in the film arises from two effects: surface tension and intermolecular pressure.² The intermolecular pressure captures various intermolecular interactions, as summarized in Tbl. 2.1. Based on the literature on dewetting films [38, 35, 74], we combine a long-range, attractive, van der Waals interaction, with exponent $n = 3$, and a short-range, repulsive interaction, with exponent $m = 4$.³

For the 3-4 potential, Eq. (2.14) gives $\kappa = a_3/\tilde{\varepsilon}^3 = A_{\text{SLV}}/6\pi\tilde{\varepsilon}^3$, such that the intermolecular pressure from Eq. (2.13) becomes

$$\tilde{\Pi}(\tilde{h}) = \frac{A_{\text{SLV}}}{6\pi\tilde{\varepsilon}^3} \left[\left(\frac{\tilde{\varepsilon}}{\tilde{h}} \right)^3 - \left(\frac{\tilde{\varepsilon}}{\tilde{h}} \right)^4 \right], \quad (4.8)$$

where $\tilde{\varepsilon}$ is the equilibrium film thickness, at which long-range van der Waals attraction balances short-range repulsion.

Using the dimensionless parameters defined in Tbl. 4.1, we find

$$\Pi(h) = \mathcal{A} \left[\left(\frac{\varepsilon}{h} \right)^3 - \left(\frac{\varepsilon}{h} \right)^4 \right], \quad (4.9)$$

where the dimensionless Hamaker constant is given by

$$\mathcal{A} = \frac{\rho A_{\text{SLV}}}{18\pi\mu^2\varepsilon^3 L}. \quad (4.10)$$

The intermolecular pressure described above can be combined with surface-tension effects (see §2.2.3) into a single dimensionless pressure:

$$p = -\mathcal{S} \frac{\partial^2 h}{\partial x^2} + \mathcal{A} \left[\left(\frac{\varepsilon}{h} \right)^3 - \left(\frac{\varepsilon}{h} \right)^4 \right], \quad (4.11)$$

²Surface tension and intermolecular interactions are reviewed in detail in §2.2.3 and §2.2.4.

³For further discussion about this choice of exponents, see §6.6.6.

where \mathcal{S} is a dimensionless surface tension given by⁴

$$\mathcal{S} = \frac{\rho\sigma\tilde{h}_0^4}{3\mu^2L^3}. \quad (4.12)$$

Dimensionless parameter	Symbol	Definition	Order of magnitude
Surface tension	\mathcal{S}	$\frac{\rho\sigma\tilde{h}_0^4}{3\mu^2L^3}$	10^{-8}
Intermolecular attraction	\mathcal{A}	$\frac{\rho A_{SLV}\tilde{h}_0^3}{18\pi\mu^2\tilde{\varepsilon}^3 L}$	10^{-6}
Diffusivity	\mathcal{D}	$\frac{\rho D\tilde{h}_0}{\mu L}$	10^{-6}
Transport coefficient	α	$\frac{18\pi\mu D\tilde{\varepsilon}^3}{A_{SLV}\tilde{h}_0^2}$	1

Table 4.2: Relevant dimensionless groups for the binary thin film. The order of magnitude estimate for parameter values is based on the material properties of methanol (see Tbl. C.2).

4.4 Needle velocity

Needle growth is assumed to be diffusion-limited as discussed in §2.3.3. The needle velocity given by Eq. (2.17) can be rewritten using the dimensionless parameters defined in Tbl. 4.1, such that⁵

$$v_{tip} = -\mathcal{D} \left. \frac{\partial \phi}{\partial x} \right|_{tip}. \quad (4.13)$$

4.5 Rescaled governing equations

Following Kao, Golovin, and Davis [48], we can eliminate the dimensionless parameters \mathcal{A} and \mathcal{S} from the pressure equation, Eq. (4.11), by introducing length and time scales proportional to the most-unstable wavelength and characteristic time of spinodal-dewetting (see physics

⁴By a strange coincidence, \mathcal{S} has the form of the inverse square of the Ohnesorge number, which measures viscous forces relative to the square root of inertia and surface tension forces. Inertia popped into the equation by way of the viscous velocity scale, ν/L .

⁵The multiplier $(\phi_{solid} - \phi_{tip})^{-1}$ from Eq. (2.17) disappears because $(\phi_{solid} - \phi_{tip}) = -1$ by definition (see Fig. 4-2).

of spinodal-dewetting in §2.2.5):

$$\hat{x} = \sqrt{\frac{\mathcal{A}}{\mathcal{S}}} x, \quad \hat{t} = \frac{\mathcal{A}^2}{\mathcal{S}} t. \quad (4.14)$$

Substituting these new scales into Eq. (4.3), Eq. (4.7), and Eq. (4.11) gives the rescaled evolution equations for the thin film and solvent-mass, and the pressure equation:

$$\frac{\partial h}{\partial \hat{t}} = \frac{\partial}{\partial \hat{x}} \left(h^3 \frac{\partial \hat{p}}{\partial \hat{x}} \right), \quad (4.15a)$$

$$\frac{\partial(\phi h)}{\partial \hat{t}} = \frac{\partial}{\partial \hat{x}} \left(\alpha h \frac{\partial \phi}{\partial \hat{x}} + \phi h^3 \frac{\partial \hat{p}}{\partial \hat{x}} \right), \quad (4.15b)$$

$$\hat{p} = -\frac{\partial^2 h}{\partial \hat{x}^2} + \left[\left(\frac{\varepsilon}{h} \right)^3 - \left(\frac{\varepsilon}{h} \right)^4 \right]. \quad (4.15c)$$

Here, the solvent evolution equation introduces the dimensionless, transport coefficient

$$\alpha = \frac{\mathcal{D}}{\mathcal{A}}. \quad (4.16)$$

This transport coefficient measures the speed of diffusion relative to the speed of coarsening. Note that rescaling by \hat{x} and \hat{t} has altered the pressure equation, but leaves h , ε , and ϕ unchanged.

Lastly, we substitute the rescaled coordinate and time into Eq. (4.13) to find the rescaled needle velocity⁶

$$\hat{v}_{\text{tip}} = -\alpha \left. \frac{\partial \phi}{\partial \hat{x}} \right|_{\text{tip}}. \quad (4.17)$$

4.5.1 Simulation parameters

This rescaling has reduced three parameters— \mathcal{A} , \mathcal{S} , and \mathcal{D} —to a single parameter, α . The rescaled \hat{x} and \hat{t} and the transport coefficient, α , can be rewritten in terms of dimensional

⁶Note that $\hat{v}_{\text{tip}} = \partial \hat{x}_{\text{tip}} / \partial \hat{t}$, such that $\hat{v}_{\text{tip}} = (\sqrt{\mathcal{S}}/\mathcal{A}\sqrt{\mathcal{A}}) v_{\text{tip}}$.

variables:

$$\hat{x} = \sqrt{\frac{A_{\text{SLV}}}{6\pi\sigma\tilde{\varepsilon}^3\tilde{h}_0}} \tilde{x}, \quad (4.18)$$

$$\hat{t} = \frac{A_{\text{SLV}}^2 \tilde{h}_0}{108\pi^2\mu\sigma\tilde{\varepsilon}^6} \tilde{t}, \quad (4.19)$$

$$\alpha = \frac{18\pi\mu D\tilde{\varepsilon}^3}{A_{\text{SLV}}\tilde{h}_0^2}, \quad (4.20)$$

where \tilde{x} and \tilde{t} are the *dimensional* coordinate and time.

The resulting mathematical model contains four dimensionless parameters:

- α , the transport coefficient, which measures diffusion relative to coarsening
- h_{solid} , the height of the solid needle
- ϕ_0 , the initial solvent-concentration
- ε , the equilibrium film-thickness

4.6 Numerical implementation

The governing equations were solved numerically using centered-finite-differences and fully-implicit time-steps [78]. An adaptive, PID control-scheme [97] varied the time-steps to minimize solution times. The numerical simulation is broken up into two steps: 1) solving the governing equations and 2) advancing the needle tip.

To calculate the thickness and concentration profiles at a given time step, we solve the governing equations, Eq. (4.3), Eq. (4.7), and Eq. (4.11).⁷ During this time, we enforce no-flux boundary conditions at both the right edge of the fluid domain and the needle tip, which enters from the left edge of the domain. Note that the tip-position is fixed in place during this time.

After evolving the film-thickness and solvent-concentration, we advance the needle tip using the tip velocity, given by Eq. (4.13). The advancing needle consumes fluid with a composition ϕ_{solid} . This consumption alters the thickness and concentration of the cells

⁷Note that we solve the dimensionless equations instead of the non-rescaled equations. The dimensionless equations are in a form that allow concentration-dependent Hamaker constant, A_{SLV} , and surface tension, σ . These dependencies, however, were not explored in this thesis

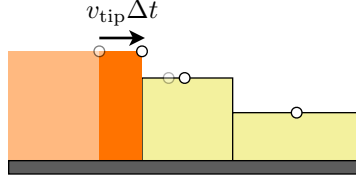


Figure 4-3: Finite-difference discretization near the needle tip. Growth of the needle distorts the finite-difference mesh.

nearest the needle tip; the film-thickness and solvent-concentration far from needle remain fixed. In addition, the growing needle shrinks the fluid domain and distorts the finite-difference mesh nearest the tip, as shown in Fig. 4-3. Details of the boundary condition at the needle tip are discussed in §B.7.

Further details of the numerical implementation, including finite-difference equations, are discussed in Appendix B.

Chapter 5

Analytical Results

In this chapter, we seek analytical solutions to the mathematical model presented in Chapter 4. In the first section, we derive relations for spinodal-dewetting and droplet-coarsening. In the following four sections, we derive simple scaling-laws to describe the growth of Alq₃-needles. To that end, we simplify the system by considering high and low limits of the transport coefficient, α , and large and small values of the needle height, h_{solid} .

5.1 Dewetting and Coarsening

In this section, we derive relations for spinodal-dewetting and droplet-coarsening. Dewetting relations are derived from linear-stability analysis, as has been done in other studies of dewetting thin, liquid films (see *e.g.*, Oron, Davis, and Bankoff [74]). The coarsening analysis follows the analysis Glasner and Witelski [38].

5.1.1 Dewetting instability

Here, we compute the most unstable wavelength, and time-scale of the spinodal-dewetting instability (as described in §2.2.5) using linear-stability analysis.

Dispersion relation

Consider a film height with a small sinusoidal perturbation:¹

$$h = 1 + \delta e^{i\hat{k}\hat{x} + \hat{\omega}\hat{t}},$$

where $\delta \ll 1$ is the amplitude of the sinusoidal perturbation with wavenumber \hat{k} and growth rate (of the instability) $\hat{\omega}$. Substituting this h into the thin-film equations (Eq. (4.15a) and Eq. (4.15c)), and keeping the terms that are linear in δ , gives the dispersion relation²

$$\hat{\omega} + \hat{k}^2(-3\varepsilon^3 + 4\varepsilon^4) + \hat{k}^4 + \mathcal{O}(\delta) = 0. \quad (5.1)$$

This dispersion relation is plotted in Fig. 5-1.

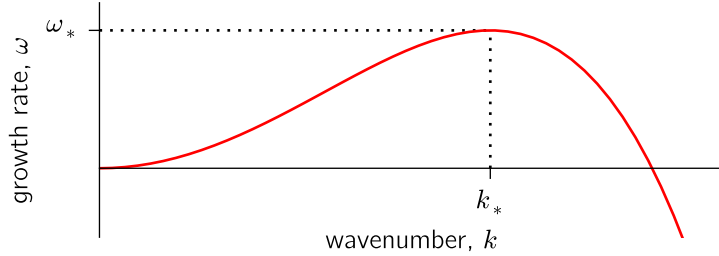


Figure 5-1: Dispersion relation for dewetting instability

Most unstable wavelength

The maximum growth rate is given by $\partial\omega/\partial k = 0$ (as shown in Fig. 5-1), which leads to the most unstable wavenumber:

$$\hat{k}_* = \sqrt{\frac{3\varepsilon^3 - 4\varepsilon^4}{2}}. \quad (5.2)$$

Because the term inside the square root cannot be negative, instability requires that $\varepsilon < 3/4$; otherwise, the film is stable and does not dewet.

¹Recall that h is the *dimensionless* film thickness, and thus, has an initial value of 1.

²The h^{-3} and h^{-4} terms required the Taylor-series expansion $(1+u)^{-1} \approx 1 - u + \mathcal{O}(u^2)$, in which u is a small parameter.

The most unstable wavelength of the instability is deduced from the wavenumber:

$$\hat{\lambda}_* = \frac{2\pi}{\hat{k}_*} = 2\pi \sqrt{\frac{2}{3\varepsilon^3 - 4\varepsilon^4}}. \quad (5.3)$$

This wavelength sets the initial size of droplets as the thin film transforms from its initially-uniform thickness.

Characteristic time scale for dewetting

To calculate the growth rate of the dewetting instability, we substitute the wavenumber, Eq. (5.2), into the dispersion relation, Eq. (5.1), which gives the growth rate $\hat{\omega}_* = (3\varepsilon^3 - 4\varepsilon^4)^2/4$. The corresponding time scale for dewetting is simply

$$\hat{\tau}_* = \frac{1}{\hat{\omega}_*} = \frac{4}{(3\varepsilon^3 - 4\varepsilon^4)^2}. \quad (5.4)$$

Dimensional wavelength and time-scale of dewetting

The wavelength given in Equation (5.3) has been nondimensionalized by a characteristic length L , and rescaled by $\sqrt{\mathcal{A}/\mathcal{S}}$ (see Eq. (4.14)); thus, the dimensional, most-unstable wavelength for the dewetting instability, $\tilde{\lambda}_*$, is related by

$$\tilde{\lambda}_* = \hat{\lambda}_* L \sqrt{\frac{\mathcal{S}}{\mathcal{A}}}. \quad (5.5)$$

Similarly, the time-scale of dewetting has been nondimensionalized by a characteristic time $\rho\tilde{h}_0L/\mu$ (see Tbl. 4.1) and rescaled by $\mathcal{A}^2/\mathcal{S}$ (see Eq. (4.14)); thus, the dimensional, characteristic time-scale for dewetting is

$$\tilde{\tau}_* = \hat{\tau}_* \frac{\rho\tilde{h}_0L}{\mu} \frac{\mathcal{S}}{\mathcal{A}^2}. \quad (5.6)$$

5.1.2 Drop coarsening

Here, we compute the typical pressure, separation, and volume of drops—given by $\langle P \rangle$, $\langle L \rangle$, and $\langle V \rangle$ —during the course of drop coarsening.

Pressure evolution equation

Following the work of Glasner and Witelski [38], we derive an equation describing the evolution of the pressure of the k th droplet (see Fig. 5-2).

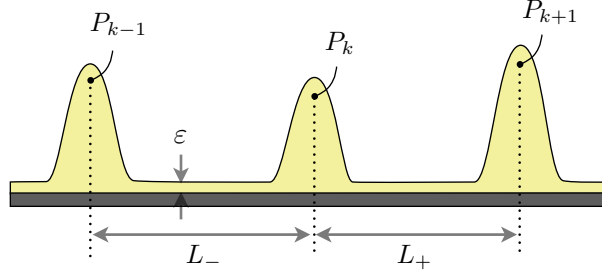


Figure 5-2: Schematic of a collapsing droplet. The k th drop is slightly smaller than adjacent drops; thus, it has a higher pressure. This pressure gradient drives flow away from the drop leading to its collapse.

From mass conservation, we know that the change in volume of the k th drop, ∇_k , is equal to the net flux into the drop, such that

$$\frac{\partial \nabla_k}{\partial t} = -(Q_+ - Q_-), \quad (5.7)$$

where Q_+ is the flux between the k and $k + 1$ drops, and Q_- is the flux between the $k - 1$ and k drops. If the thickness of the ultra-thin film connecting droplets is approximately, ε ,³ then the volumetric flux (given by Eq. (4.2)) simplifies to

$$Q_+ \approx -\varepsilon^3 \frac{P_{k+1} - P_k}{L_+}.$$

To derive the pressure evolution equation, we note that for sufficiently-large drops, surface tension dominates intermolecular interactions, such that a drop is approximately parabolic; this approximation gives a direct relation between the droplet volume (per unit depth) and

³Note that the thickness of the wetting layer must be thicker than ε to balance the positive pressure in adjacent drops. The intermolecular pressure rises sharply for small changes in h , so the deviation from ε is small.

drop pressure:⁴ $\nabla_k \sim P_k^{-2}$. Recalling the chain rule of differentiation, we find that

$$\frac{\partial \nabla_k}{\partial t} = \frac{\partial \nabla_k}{\partial P_k} \frac{\partial P_k}{\partial t} \sim \frac{\partial P_k}{\partial t} P_k^{-3}.$$

Combining the three previous equations gives

$$\frac{dP_k}{dt} \sim \varepsilon^3 P_k^3 \left[\frac{P_{k+1} - P_k}{L_+} - \frac{P_k - P_{k-1}}{L_-} \right]. \quad (5.8)$$

Collapse of k th drop

If the collapsing droplet, k , is much smaller than the typical droplet, then $P_k \gg \langle P \rangle$, where the pressure of the typical drop is $\langle P \rangle \approx P_{k+1} \approx P_{k-1}$. Thus, the pressure evolution equation, Eq. (5.8), simplifies to

$$\frac{dP_k}{dt} \sim -\frac{1}{\langle L \rangle} P_k^4,$$

where $L_+ \approx L_- \approx \langle L \rangle$, and $\langle L \rangle$ is the average spacing between droplets. Integration gives

$$P_k^{-3} \sim \frac{1}{\langle L \rangle} (T_c - t),$$

where T_c is the time of drop collapse.

If the initial pressure of the drop is equal to the average droplet pressure, $\langle P \rangle$, then the collapse time scales like

$$T_c \sim \langle P \rangle^{-3} L.$$

From §5.1.2, we know the droplet volume scales like $\langle V \rangle \sim \langle P \rangle^{-2}$. Additionally, conservation of mass⁵ tells us that $\langle V \rangle \sim N^{-1}$ and $\langle L \rangle \sim N^{-1}$. Substituting these scalings gives

$$T_c \sim N^{-3/2} N^{-1} \sim N^{-5/2}.$$

⁴The drop is parabolic, such that $\langle h \rangle \sim \frac{1}{2} \langle p \rangle (\langle w \rangle^2 - x^2)$. The width of the drop, $\langle w \rangle \sim \langle p \rangle^{-1}$, such that $\langle m \rangle = \int_{-\langle w \rangle}^{\langle w \rangle} \langle h \rangle dx \sim \langle p \rangle^{-2}$. See Glasner and Witelski [38, §II] for details.

⁵Imagine a distribution of equally-sized, evenly distributed droplets. If every-other drop collapses and coalesces with its neighbor, there will be half the number of drops. The new super droplets will be twice the volume; and the spacing between drops will be twice as great.

Scaling laws

Averaged out over many droplet collapses, the rate of change of droplets scales like $dN/dt \sim -N/T_c \sim -N^{7/2}$. Integrating in time gives

$$N \sim t^{-2/5}. \quad (5.9)$$

Using this scaling, we find that the typical drop pressure, drop spacing, and drop volume scale as

$$\begin{aligned} \langle P \rangle &\sim t^{-1/5}, \\ \langle L \rangle &\sim t^{2/5}, \\ \langle V \rangle &\sim t^{2/5}. \end{aligned} \quad (5.10)$$

This section has focused on the formation and evolution of drops in the thin film. In contrast, the remaining sections in this chapter focus on the growth of needles.

5.2 High α -values: diffusion-dominated needle growth

In the high- α limit, transport is dominated by diffusion, such that the solvent-mass equation, Eq. (4.15b), simplifies to⁶

$$\frac{\partial \phi}{\partial \hat{t}} = \alpha \frac{\partial^2 \phi}{\partial \hat{x}^2}. \quad (5.11)$$

The above is simply the diffusion equation in one dimension.

To find the tip position as a function of time, we assume a semi-infinite domain (the fluid domain extends to infinity). The diffusion equation, Eq. (5.11), with boundary and initial conditions:

$$\begin{aligned} \phi(\hat{x}, 0) &= \phi_0, \quad \text{for } \hat{x} > \hat{x}_{\text{tip}}, \\ \phi(\hat{x}_{\text{tip}}, \hat{t}) &= 1, \\ \phi(\infty, \hat{t}) &= \phi_0, \end{aligned}$$

⁶Since diffusion is much faster than convection, changes in concentration dominate those in the film-thickness, such that $\partial(\phi h)/\partial t \approx h \partial \phi / \partial t$.

can be solved with an error function of the form

$$\phi(\hat{x}, \hat{t}) = a_1 + a_2 \operatorname{erf} \left(\frac{\hat{x}}{\sqrt{4\alpha\hat{t}}} \right),$$

where a_1 and a_2 are constants that depend on the boundary and initial conditions. Applying the boundary condition $\phi(\hat{x}_{\text{tip}}, \hat{t}) = 1$, we find that

$$1 = a_1 + a_2 \operatorname{erf} \left(\frac{\hat{x}_{\text{tip}}}{\sqrt{4\alpha\hat{t}}} \right).$$

For the above relation to be valid at *all* times (as the boundary condition requires), the time dependence must disappear from the argument of the error function, such that

$$L_{\text{needle}} \sim \hat{t}^{1/2}. \quad (5.12)$$

Here, $L_{\text{needle}} \equiv \hat{x}_{\text{tip}}$, if $\hat{x}_{\text{tip}}(t=0) = 0$.

For an exact expression of one-dimensional, diffusional growth, see *Kinetics of Materials* [3, §20.1.2].

5.3 Low α -values: coarsening-dominated needle growth

For low α -values, droplets collapse rapidly compared to diffusion and drive fluid flow through the liquid film. This flow carries solvent through the film faster than diffusion; nevertheless, it would be misleading to suggest that diffusion is negligible in this limit because the needle velocity is a function of the concentration gradient at the tip.

As shown in Fig. 5-3, a meniscus region connects the needle tip to an ultra-thin film—which we dub the “wetting layer”—with a thickness of approximately ε . The meniscus has a length, L_m , and the concentration at the edge of the meniscus is ϕ_m (see Fig. 5-3). In the following analysis, we seek a needle length that scales like a power law in time. To that end, we assume that L_m and $\Delta\phi = 1 - \phi_m$ (the difference in concentration⁷ between the needle

⁷Why do we define $\Delta\phi$ (instead of ϕ_m) as a power-law, you ask. A power-law can describe quantities that grow without bound (positive exponents) or approach zero (negative exponents). Whereas $\Delta\phi$ asymptotes to zero, ϕ_m approaches one; thus, $\Delta\phi$ is more suited to power-law relations.

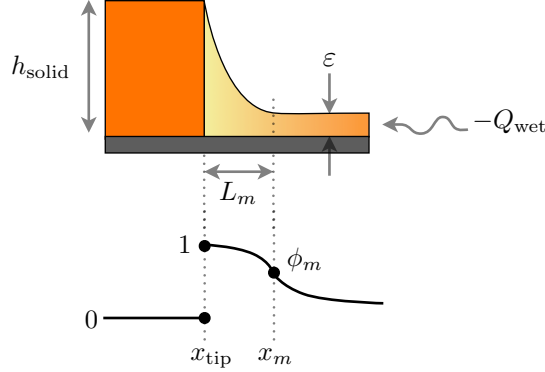


Figure 5-3: A meniscus connects the needle tip to a thin wetting layer with approximate thickness ε . Fluid flux across the right edge of the meniscus, x_m , is given by Q_{wet} . On the left edge, Alq₃ leaves the the meniscus as it solidifies into the solid crystal needle.

tip and meniscus edge) grow like power laws:⁸

$$L_m \sim t^a, \quad (5.13a)$$

$$\Delta\phi \sim t^{-b}, \quad (5.13b)$$

where exponents a and b are positive. As solvent builds up in front of the needle, ϕ_m approaches 1, such that $\Delta\phi \rightarrow 0$; this leads to the decaying power law shown above.

5.3.1 Mass conservation at the growing needle tip

When a droplet near the needle collapses, fluid in that drop is driven toward the needle tip. However, not all of that fluid can be incorporated into the needle since it has a specific composition, $\phi_{\text{solid}} = 0$. Since the needle is solvent-poor, left-over solvent builds up in front of the needle tip and slows needle growth. Thus, needle growth is governed by a balance between the flux of fluid toward and diffusion of solvent away from the needle tip. In addition, the meniscus at the tip of the needle can grow to incorporate fluid from collapsing drops. Applying mass conservation gives⁹

$$v_{\text{tip}} h_{\text{solid}} + \dot{V}_m \approx -Q_{\text{wet}}, \quad (5.14)$$

⁸In simulations, L_m and $\Delta\phi$ exhibit power-law behavior, so this is a pretty good assumption.

⁹Rigorous analysis would show that there should be a $v_{\text{tip}}\varepsilon$ term on the right-hand-side because we take a reference frame that moves with the needle tip. But moving this term to the left-hand-side gives $v_{\text{tip}}(h_{\text{solid}} - \varepsilon) \approx v_{\text{tip}}h_{\text{solid}}$.

where Q_{wet} is the flux through the wetting layer, v_{tip} is the needle velocity, and $\dot{\mathbb{V}}_m$ is the time derivative of the meniscus volume.

The needle velocity, given by Eq. (4.17), can be approximated as¹⁰

$$v_{\text{tip}} \approx -\alpha \frac{\phi_m - 1}{L_m} \sim \frac{\Delta\phi}{L_m} \sim t^{-a-b}. \quad (5.15)$$

When the needle tip is large, the majority of the meniscus is much higher than the equilibrium thin-film height, ε . Thus, surface-tension effects dominate intermolecular forces, such that the meniscus is approximately parabolic:

$$h \approx (h_{\text{solid}} - \varepsilon) \left(\frac{x - x_m}{L_m} \right)^2 + \varepsilon.$$

To solve for the fluid volume in the meniscus, integrate the thickness profile:

$$\mathbb{V}_m = \int_{x_{\text{tip}}}^{x_m} h \, dx = \frac{1}{3}(h_{\text{solid}} + 2\varepsilon)L_m.$$

Thus, the time-rate of change of volume is

$$\dot{\mathbb{V}}_m = \frac{1}{3}(h_{\text{solid}} + 2\varepsilon)\dot{L}_m \sim t^{a-1}. \quad (5.16)$$

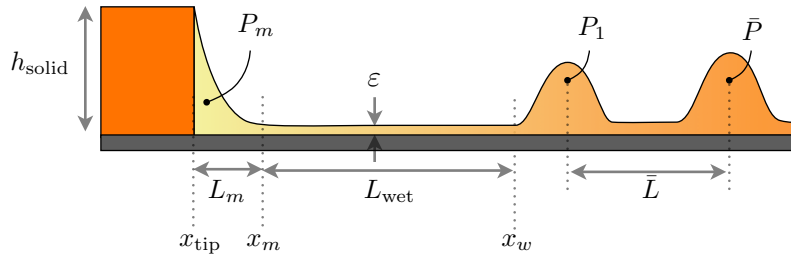


Figure 5-4: Schematic of needle growing from left to right. A meniscus, with pressure P_m , connects the needle tip and a thin wetting layer. Fluid flow to the needle is driven by the pressure difference between the meniscus and the drop closest to the needle tip—i.e., the first drop.

The fluid flow through the wetting layer depends on the length of the wetting layer, L_{wet} ; the pressure in the meniscus, P_m ; and the pressure of the first drop, P_1 (see Fig. 5-4). Thus,

¹⁰Note that the negative sign cancels because $\phi_m - 1 = -\Delta\phi$.

the fluid flux, given by Eq. (4.2), can be approximated by

$$Q_{\text{wet}} = -h^3 \frac{\partial \hat{P}}{\partial \hat{x}} \sim -\varepsilon^3 \frac{P_1 - P_m}{L_{\text{wet}}}. \quad (5.17)$$

The positive curvature of the meniscus at the needle creates a low pressure region, while the negative curvature of the drop closest to the needle tip—*i.e.*, the first drop—creates a high pressure region. Thus, flow is driven toward the needle, such that Q_{wet} is negative.

In the following sections, we derive expressions for this fluid flux, which depends on the height of the needle relative to the fluid film.

5.4 Needle growth for low α -values and small h_{solid}

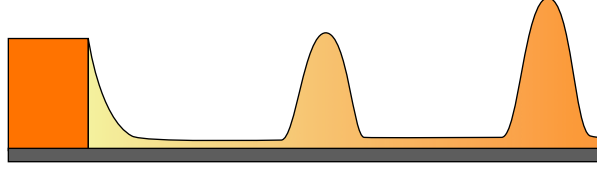


Figure 5-5: Schematic of a small needle: needles that are roughly the same size as the typical droplet are dubbed “small”.

When the height of the needle, h_{solid} , is roughly the same size as (or smaller than) the typical drop, as shown in Fig. 5-5, we say the needle is “small”. In this limit, the pressure in the meniscus is comparable to that of the typical drop, $\langle P \rangle$, and the distance from the needle tip to the first drop is comparable to the typical drop spacing, $\langle L \rangle$; thus, the flux through the film—given by Eq. (5.17)—simplifies to $Q_{\text{wet}} \sim -\varepsilon^3 \langle P \rangle / \langle L \rangle$. From Eq. (5.10), $\langle P \rangle \sim t^{-1/5}$ and $\langle L \rangle \sim t^{2/5}$, such that

$$Q_{\text{wet}} \sim t^{-3/5}.$$

Moderate meniscus pressures correspond to meniscus lengths that are insensitive to pressure variations, as can be deduced from Eq. (5.19). Thus, the change in meniscus volume is

negligible in this small h_{solid} regime, and Eq. (5.14) simplifies to

$$v_{\text{tip}} \sim Q_{\text{wet}} \sim t^{-3/5}.$$

Finally, integrating once in time gives a needle length that scales as

$$L_{\text{needle}} \sim t^{2/5}. \quad (5.18)$$

5.5 Needle growth for low α -values and large h_{solid}



Figure 5-6: Schematic of a large needle: needles that are larger than the typical droplet are dubbed “large”.

Here, we solve for the needle length as a function of time for α -values much smaller than 1 and large needle heights, h_{solid} . Here, “large” needle heights suggest that the needle is much larger than the typical drop, as shown in Fig. 5-6.

5.5.1 Flux through the wetting layer

In this section, we derive a power-law relation for the flux through the wetting layer, Q_{wet} , given by Eq. (5.17). For large h_{solid} , the *magnitude* of the pressure in the meniscus is large compared to that in the drops; *i.e.*, $|P_m| \gg |P_1|$. Thus, to derive an expression for the flux through the wetting layer, we need expressions for the meniscus pressure, P_m , and the length of the wetting layer, L_{wet} .

Meniscus pressure

If the needle tip is large, the meniscus height is far from the ultra-thin-film thickness (which is approximately ε), such that surface tension dominates and the meniscus is approximately

parabolic; thus, we can relate the meniscus pressure to the length of the meniscus:

$$P_m \sim -\frac{h_{\text{solid}} - \varepsilon}{L_m^2}. \quad (5.19)$$

Since only L_m is time-dependent, we can write

$$P_m \sim -t^{-2a}. \quad (5.20)$$

Collapse time of the first-drop

At early times $|P_m| \gg |P_1|, |\langle P \rangle|$, such that the pressure evolution equation, Eq. (5.8), simplifies to

$$\frac{dP_1}{dt} \sim \frac{\varepsilon^3}{L_{\text{wet}}} P_1^3 P_m. \quad (5.21)$$

The wetting layer grows when the k th first-droplet collapses, at which time $L_{\text{wet}}^{k+1} = L_{\text{wet}}^k + \langle L \rangle^k$, as depicted in Fig. 5-7. Before the collapse, the length of the wetting layer is roughly constant.¹¹ In addition, we will assume that the thickness of the wetting layer, is approximately ε (a time-varying thickness is discussed in §6.4.1).

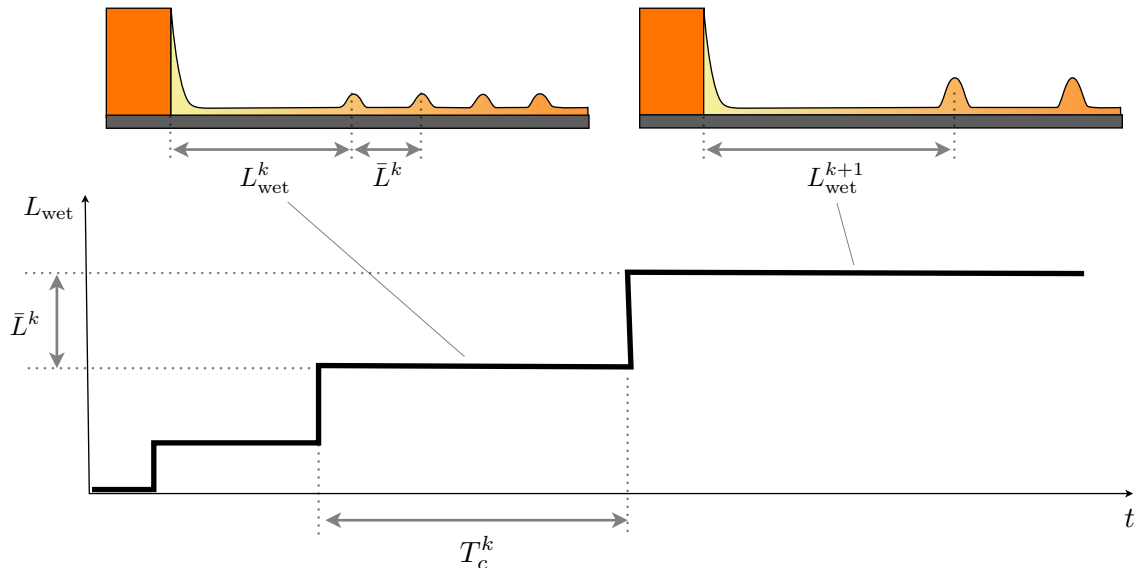


Figure 5-7: Growth of the wetting layer, which separates the needle tip from the droplet region. The wetting layer grows in discrete steps since the collapse of the nearest drop leads to a finite increase in the wetting layer.

¹¹This assumption is true only if the droplet collapses much faster than the meniscus and the needle grow.

In the differential equation for P_1 , we can separate variables and integrate to find

$$P_1^{-2} \sim -\frac{1}{L_{\text{wet}}} t^{1-2a} + C.$$

As the droplet collapses, the pressure should diverge (since small droplets have high pressure); thus, the droplet pressure can be written as

$$P_1 \sim \left[\frac{1}{L_{\text{wet}}} (T_c - t)^{1-2a} \right]^{-1/2},$$

where T_c is the time period for the collapse of the k th-first-drop. Here, t is measured starting when the previous first-drop ($k - 1$) collapses; thus at $t = 0$, the k th drop should have the same pressure as a typical drop,¹² *i.e.*, $P_1(t = 0) = \langle P \rangle$, such that

$$T_c \sim (L_{\text{wet}} \langle P \rangle^{-2})^{1/(1-2a)}.$$

Growth of wetting layer

For large needles, the pressure in the meniscus is large (in magnitude) and negative. This large pressure leads to faster droplet collapses near the needle tip, thus building up a large wetting layer between the needle tip and the first drop.

The wetting layer grows in discrete steps each time a droplet collapses, as depicted in Fig. 5-7. This discrete growth can be approximated as a continuous process:

$$\frac{dL_{\text{wet}}}{dt} \sim \frac{\langle L \rangle}{T_c}. \quad (5.22)$$

Far away from the needle tip, the dynamics are governed by coarsening effects alone, such that the typical drop spacing scales as $\langle L \rangle \sim t^{2/5}$, and pressure scales as $\langle P \rangle \sim t^{-1/5}$ (as derived in §5.1.2). Substitution of these scalings and the meniscus pressure (from Eq. (5.20))

¹²When the $k - 1$ drop is the first-drop, the k th drop is shielded from the low pressure meniscus by the $k - 1$ drop; thus, k th drop should behave like a typical drop and have a typical pressure $\langle P \rangle$.

into Eq. (5.22) gives

$$\frac{dL_{\text{wet}}}{dt} \sim \langle L \rangle \left(L_{\text{wet}}^{-1} \langle P \rangle^2 \right)^{1/(1-2a)} \sim L_{\text{wet}}^{-1/(1-2a)} t^{-4a/(5-10a)}.$$

Separating variables and integrating gives

$$L_{\text{wet}} \sim t^{(5-14a)/(10-10a)}. \quad (5.23)$$

5.5.2 Needle growth

For large needle tips $|P_m| \gg |\langle P \rangle|$, such that $Q_{\text{wet}} \sim \varepsilon^3 P_m / L_{\text{wet}}$. Now, substitute scalings for P_m and L_{wet} (Eq. (5.20) and Eq. (5.23)) to get

$$Q_{\text{wet}} \sim -t^{-(5+6a-20a^2)/(10-10a)}. \quad (5.24)$$

Note that Q_{wet} is negative because the flux moves in the negative x -direction.

We now return to the mass conservation equation, Eq. (5.14), and substitute in the power-law scalings for the needle velocity, Eq. (5.15); meniscus mass, Eq. (5.16); and flux, Eq. (5.24); which gives

$$t^{-a-b} + t^{a-1} \sim t^{-(5+6a-20a^2)/(10-10a)}.$$

All terms balance when $a \approx 0.29$ and $b \approx 0.42$, such that the needle velocity scales like $v_{\text{tip}} \sim t^{-0.71}$. Finally, integrating once in time gives a needle length which scales as

$$L_{\text{needle}} \sim t^{0.29}. \quad (5.25)$$

This scaling law, along with those derived above, are summarized in Tbl. 5.1.

	scaling law
high α	$L_{\text{needle}} \sim t^{1/2}$
low α , small needle	$L_{\text{needle}} \sim t^{2/5}$
low α , large needle	$L_{\text{needle}} \sim t^{0.29}$

Table 5.1: Scaling laws for needle growth for high α -values (all needle heights) and for low α -values—both small and large needle heights.

Chapter 6

Results and Discussion

6.1 Overview

This chapter presents the results of experiments and simulations, with comparisons to the analytical results from Chapter 5.

6.1.1 Experiments

Figure 6-1 shows a glass substrate after a 3 hour anneal. The substrate is covered with thousands of microscopic Alq₃ needles. Micrographs of the substrate show crystals growing within a few minutes of beginning the annealing process. The crystal needles tend to grow in clusters surrounding a common nucleation point. These nucleation sites were not seeded; instead, it appears they come from imperfections during deposition or, possibly, from particulate contamination during handling.

In the following experiments, the thickness of the deposited Alq₃ film, \tilde{h}_{Alq} ,¹ is varied from 15–60 nm; the influence of \tilde{h}_{Alq} on simulation parameters is discussed in §6.1.3. No other experimental parameters are varied in this thesis. The following discussion assumes that solvent-vapor saturates the annealing chamber at short times compared to the time scale of the experiment.² Further details of the experimental setup and data analysis are

¹ \tilde{h}_{Alq} should not be confused with the initial thickness \tilde{h}_0 , which is the thickness of the film *after* solvent is combined with Alq₃.

²The small annealing chamber (see Fig. 3-3) limits air flow, so that solvent-vapor transport is dominated by diffusion. For diffusion in vapor, the diffusivity is on the order of $D \approx 0.1 \text{ cm}^2/\text{s}$ ($10^{-5} \text{ m}^2/\text{s}$) [68]. The

presented in Chapter 3.

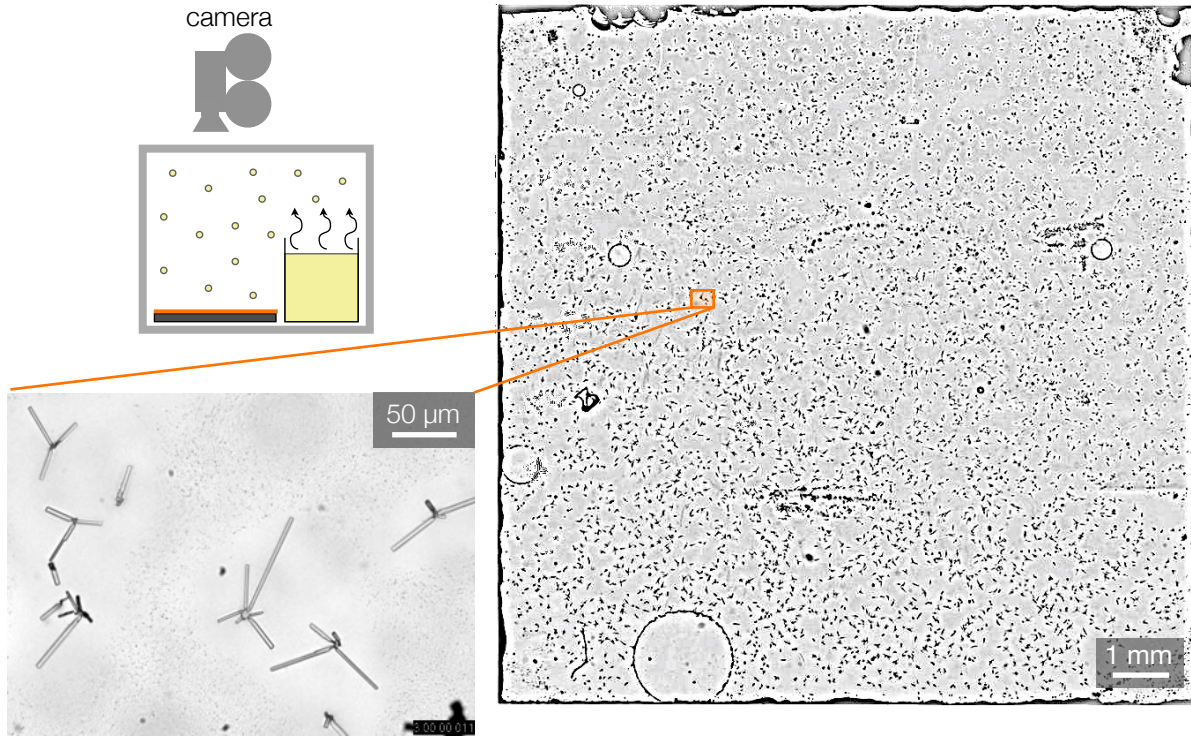


Figure 6-1: Glass substrate after annealing for 3 hours. Needles usually grow in clusters, surrounding a region favorable to nucleation, as shown in the magnified image in the bottom-left. The clear, circular regions on the substrate mark where methanol accidentally splashed onto the substrate during setup.

6.1.2 Simulations

The numerical simulations solve the evolving thin-film thickness and solvent concentration, as described in Chapter 4. At the start of the simulation, a seed of solid Alq₃ is placed at the left edge of the domain³ (*i.e.*, $0 \leq x \leq x_{\text{tip}}$); as a result, nucleation is not examined in this study. All simulations presented here are initialized with a uniform solvent-concentration in the fluid domain (*i.e.*, $\phi_0 = \text{constant}$ for $x > x_{\text{tip}}$). The thin-film thickness was initialized with $h_0 = 1 + \delta(x)$, where $\delta(x)$ are spatially-varying, small, random values⁴ that add noise (*i.e.*, roughness) to the initial condition.

³In other words, a node at the left edge of the domain was given values $h = h_{\text{solid}}$ and $\phi = \phi_{\text{solid}}$ at $t = 0$.
⁴In practice, $\delta(x)$ has a uniform distribution with a magnitude of 0.1 (*i.e.*, approximately 1/10th of the initial film thickness).

The resulting solutions depend on the main parameters of the simulation: ε , ϕ_0 , h_{solid} , and α ; the following results explore a range of values as described in Tbl. 6.1.

Parameter	Description	Values
α	transport coefficient	10^{-4} – 10^1
h_{solid}	height of crystal needle	1–64
ϕ_0	initial concentration	0.1–0.9
ε	equilibrium film thickness	0.05–0.75

Table 6.1: Range of dimensionless parameters explored in simulations

6.1.3 Comparing simulations and experiments

Exact comparison between simulations and experiments is limited because of limited thermodynamic data for solvent-Alq₃ interactions; this problem is common in solvent-molecule solutions, as noted by Rabani *et al.* [79]. Instead, we leave material properties as fitting parameters in comparisons between simulations and experiments.

In experiments, we vary the thickness of the deposited Alq₃ film, \tilde{h}_{Alq} . On the other hand, simulations depend on the thickness of the mixture (*i.e.*, Alq₃ plus solvent) \tilde{h}_0 . In much of the following, we assume that $\tilde{h}_0 \sim \tilde{h}_{\text{Alq}}$.⁵ Thus, the Alq₃ thickness, \tilde{h}_{Alq} , can influence any of the simulation parameters in Tbl. 6.1:

- The transport coefficient (Eq. (4.18)): $\alpha \sim \tilde{h}_0^{-2} \sim \tilde{h}_{\text{Alq}}^{-2}$. This dependence is discussed further in §6.2.3.
- The height of the crystal: $h_{\text{solid}} = \tilde{h}_{\text{solid}}/\tilde{h}_0 \sim \tilde{h}_{\text{Alq}}^{-1}$.
- The initial concentration, ϕ_0 , could vary with \tilde{h}_{Alq} if the increase in Alq₃ is not matched by a proportional increase in solvent condensation during annealing.
- The equilibrium film thickness: $\varepsilon = \tilde{\varepsilon}/\tilde{h}_0 \sim \tilde{h}_{\text{Alq}}^{-1}$

⁵This assumption is equivalent to assuming that solvent-vapor condensation is dominated by Alq₃-solvent interactions. Thus, doubling the Alq₃-film thickness would double the amount of solvent condensation.

6.2 Needle Growth

In experiments, we measure the growth of needles while varying the initial Alq₃-film thickness, \tilde{h}_{Alq} . In simulations, we examine needle growth as a function of each simulation parameter (ε , ϕ_0 , h_{solid} , and α), while holding all other parameters constant. §C.2 provides additional details on growth regimes observed in simulations.

6.2.1 Evolution of needle lengths in experiments

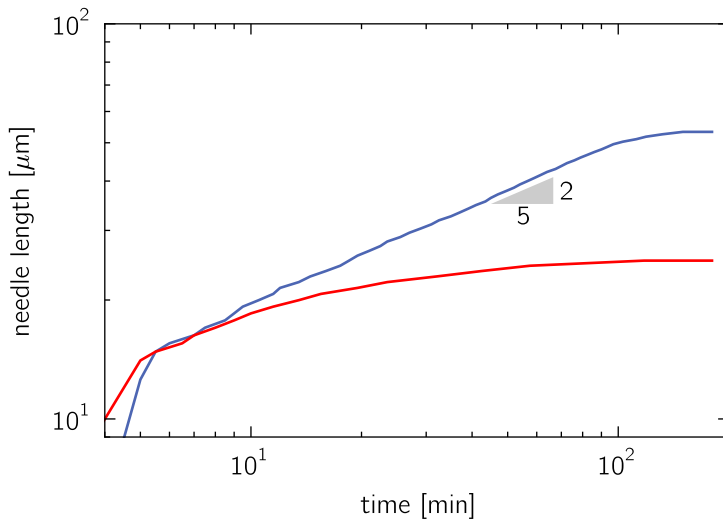


Figure 6-2: Evolution of needle lengths for a 15 nm thick Alq₃ film. The blue curve shows the steady growth of an unobstructed needle; the red curve shows the evolution of a needle that is obstructed by other growing needles.

In experiments, needle lengths are measured during solvent-vapor annealing, as described in §3.4. Figure 6-2 shows the evolution of two representative needles growing from a 15 nm Alq₃-film. The blue curve (which is the same needle as in Fig. 3-5) shows the steady growth of a needle, with a slope of 2/5. Because both axes of the plot are logarithmic, this curve suggests a power-law growth

$$L_{\text{needle}} \sim t^\gamma$$

with a growth-exponent $\gamma = 2/5$. Since $0 < \gamma < 1$, needle growth slows down over time; this slowing-of-growth reflects the depletion of liquid Alq₃ over time (due to solidification). At

late times, the growth saturates (*i.e.*, the needle stops growing) as nearby Alq₃ is consumed by adjacent needles.

The red curve in Fig. 6-2 shows the evolution of a needle that is obstructed by other growing needles; this needle grows more slowly and is poorly-fit by a power-law. In the following analysis, obstructed needles have been filtered from the data. This filtering facilitates comparison with simulations, in which we ignore needle interactions. An example of this filtering is shown in §C.1.

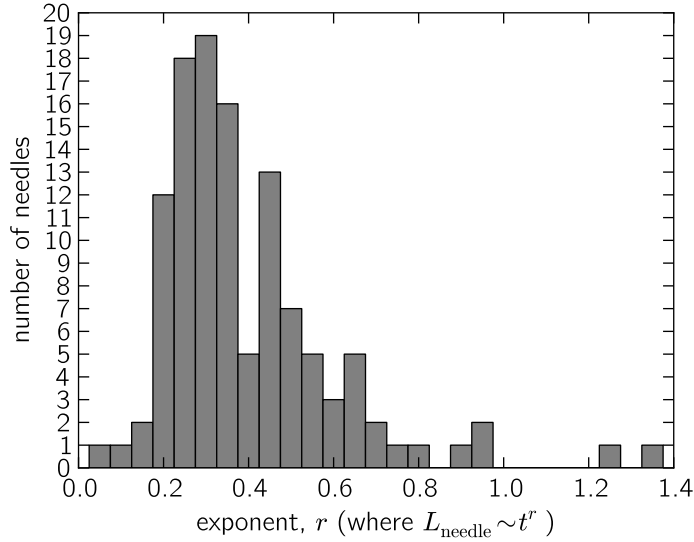


Figure 6-3: Histogram of growth exponents from solvent-annealing experiments on a 30 nm Alq₃ film.

Despite filtering out interaction-effects, needles exhibited variable growth-exponents under identical experimental conditions. Thus, we measure the growth of many needles and look for statistically significant growth-exponents. Figure 6-3 compares the growth exponent, γ , for 117 Alq₃-needles growing from a solvent-annealed Alq₃-film with initial thickness $\tilde{h}_{\text{Alq}} = 30 \text{ nm}$.

6.2.2 Influence Alq₃ film thickness, \tilde{h}_{Alq}

In experiments, varying the thickness of the deposited Alq₃-film affects the growth rates, nucleation phenomena, and crystal morphology, as shown in Fig. 6-4. Here, we discuss its influence on the growth of needles; nucleation phenomena and crystal morphology are discussed in §6.5.

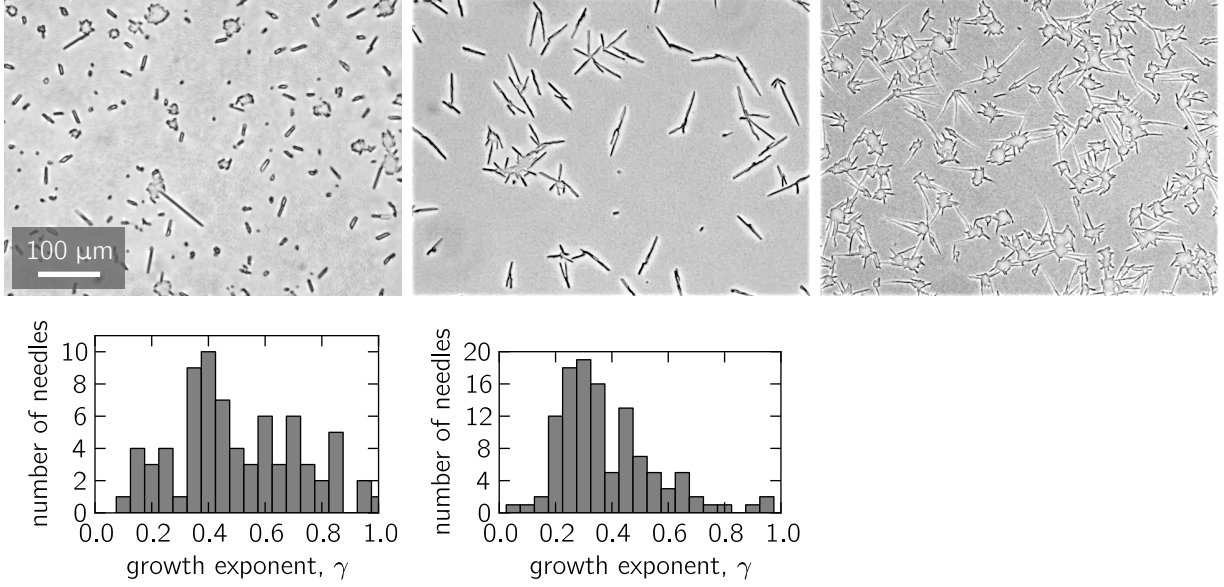


Figure 6-4: Micrographs and histograms for various Alq_3 film-thicknesses; increasing thickness from left to right. Thinner films produced more rectangular needles, while thicker films produced tapered, slightly-curved needles. In addition, thicker films produced more clustering. These images are taken 45 minutes after the first-noticeable nucleation events.

Figure 6-4 shows micrographs of growing needles and histograms of their growth exponents, γ , for $\tilde{h}_{\text{Alq}} = 15, 30, and 60 nm . Despite the wide range of γ -values, the histograms show a strong peak at $\gamma \approx 0.4$ for $\tilde{h}_{\text{Alq}} = 15 \text{ nm}$ and $\gamma \approx 0.3$ for $\tilde{h}_{\text{Alq}} = 30 \text{ nm}$. Unfortunately, needle length measurements for thick films (*i.e.*, $\tilde{h}_{\text{Alq}} = 60 \text{ nm}$) were not possible due to branching of the crystals; see §6.5 for details.$

6.2.3 Influence of transport coefficient, α

In simulations, the transport coefficient, α , is analogous to an inverse Sherwood number, with convection driven by droplet coarsening (which, itself, is driven by the strength of intermolecular attraction).⁶ Diffusion dominates at high values of α ; while, convection—fluid flow driven by the collapse of droplets—dominates at low α -values.

Figure 6-5 shows simulation results for $h_{\text{solid}} = 16$, $\phi_0 = 0.5$, and $\varepsilon = 0.5$. At low α -values, coarsening dominates diffusion; the growth exponent asymptotes to a value of

⁶Note, however, that for a given α , droplet collapse will slow down, such that the average flow rate due to coarsening will be a function of time. Thus, regardless of α -value, diffusion will dominate at sufficiently-late times. See §C.2.1 for details.

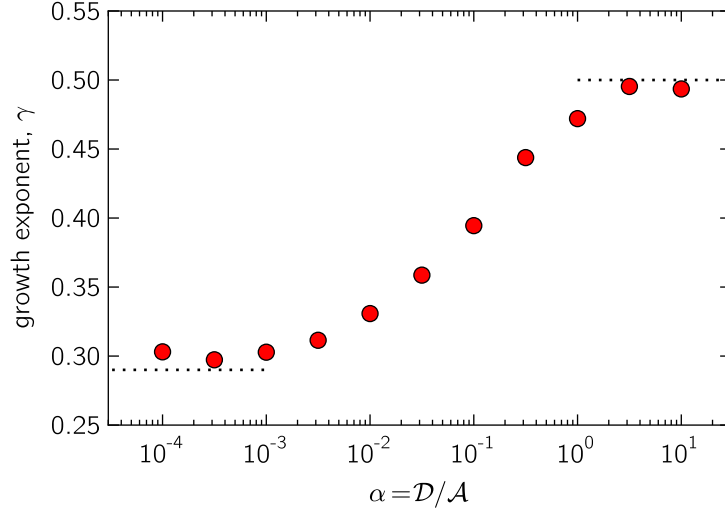


Figure 6-5: Growth exponent as a function of α ($h_{\text{solid}} = 16$). For high α -values, diffusion dominates and the growth approaches a power law of $t^{1/2}$; while, for low α -values, coarsening dominates and needle growth approaches $t^{0.29}$.

approximately $\gamma = 0.29$, as discussed in §5.5. At high α -values, diffusion dominates, and the growth exponent asymptotes to a value of approximately $\gamma = 0.5$, as discussed in §5.2. In between these asymptotes, both coarsening and diffusion are significant in the transport of Alq₃ to the needle.

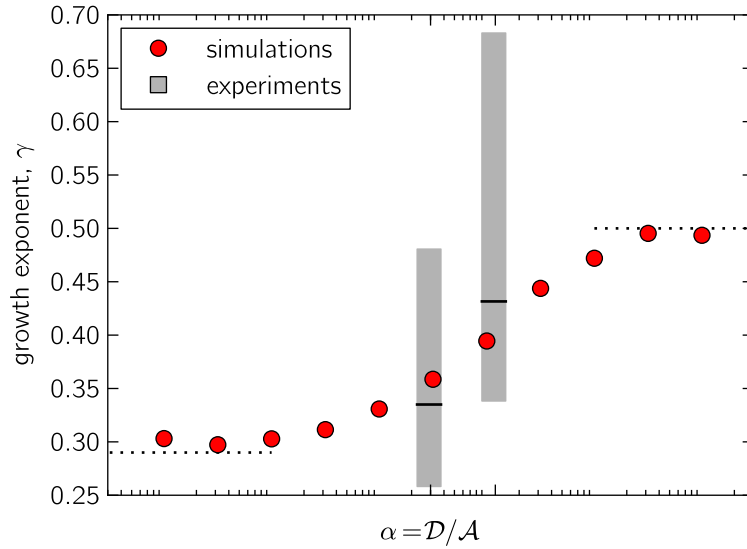


Figure 6-6: Growth exponents from experiments as a function of α . The gray box extends from the lower to upper quartile of the experimental data; while the line bisecting the box marks the median of the data. The red dots mark growth-exponents from simulations.

6.2.4 Comparing needle growth in simulations and experiments

As discussed in §6.1.3, we can compare simulations and experiments by assuming that the transport coefficient scales as

$$\alpha = A \tilde{h}_{\text{Alq}}^{-2}, \quad (6.1)$$

where A is an unknown constant representing the unknown material properties in α (see Tbl. 4.2). Using this assumption, Fig. 6-6 compares the simulation results for varying α with the experimental results for varying \tilde{h}_{Alq} , where A in Eq. (6.1) is a fitting parameter. The gray box extends from the lower to upper quartile of the experimental data; the horizontal line bisecting the box marks the median of the data.⁷ The red dots mark growth-exponents from simulations.

The median of the experimental data matches the trend predicted in simulations, but there is a noticeable difference in values. In addition, the variance of γ in experiments is large compared to the range of exponents predicted in simulations. The variance is likely caused by the randomness of nucleation: the location, orientation, and time of nucleation is random. This randomness can lead to needles that interfere with each other (as discussed in §C.1), local concentrations that are not initially-uniform, and needles with different widths/thicknesses. None of these variations are considered in the present study.

6.2.5 Influence of needle thickness, h_{solid}

In simulations, the growth exponent is dependent on needle thickness, as discussed in Chapter 5. When the transport coefficient, α , is small, we find that the growth exponent asymptotes to a value of $\gamma = 0.4$ for small needles (see §5.4) and approximately $\gamma = 0.29$ for large needles (see §5.5). Simulation results for needle heights ranging from $h_{\text{solid}} = 1$ to 64 match the asymptotic predictions, as shown in Fig. 6-7.

In experiments, the needle is significantly thicker than the initial Alq₃-film thickness. Figure 6-8 shows the tip of a needle grown from a 15 nm Alq₃-film. To capture this image, the substrate was tilted 60° from horizontal.⁸ As a result of this tilt, the needle thickness

⁷In other words, the experimental data in Fig. 6-6 is plotted as a box-and-whisker plot, minus the whiskers.

⁸With no substrate-tilt, you have a top-down view and could not see the needle thickness. With a 90°, tilt you could measure the thickness directly, but you would only be able to focus on the very edges of the

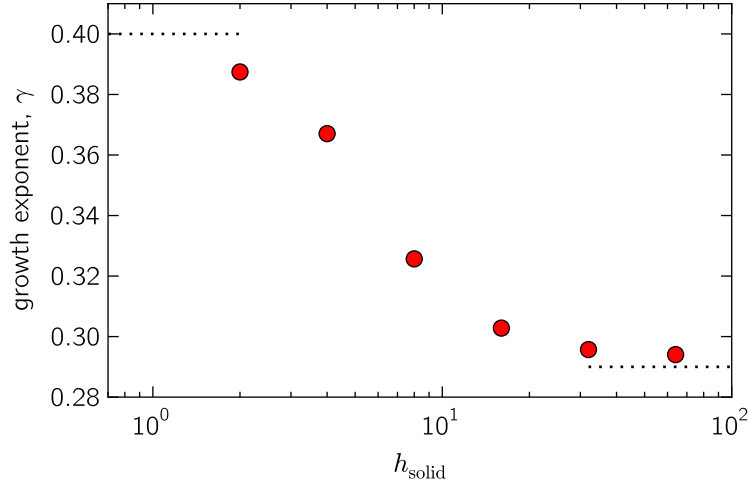


Figure 6-7: Growth exponent as a function of h_{solid} for low α -values. For thin needles, the growth approaches a power law of $t^{2/5}$; while, for low α -values, it approaches $t^{0.29}$. For all simulations, $\alpha = 0.001$ and $\phi_0 = 0.5$. For $h_{\text{solid}} = 2$, $\varepsilon = 0.65$ to decrease the time required to reach equilibrium (see 6.2.7), such that drop collapses do not interfere with the growth-exponent (see C.2.3); for all other simulations, $\varepsilon = 0.5$.

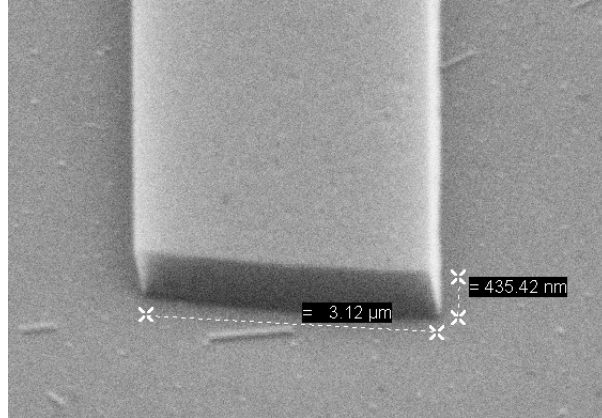


Figure 6-8: SEM (scanning electron microscope) image of needle tip for a 15 nm Alq₃-film. The substrate is tilted 60° from horizontal.

(which reads ~ 435 nm in the micrograph) is foreshortened. Accounting for the foreshortening due to tilt, we find $h_{\text{solid}} \approx (435 \sin 60^\circ) \text{ nm} \approx 500 \text{ nm}$.

The needle in Fig. 6-8 is approximately 30 times as thick as the original Alq₃-film. Note, however, that during solvent-annealing, methanol combines with Alq₃, such that the thickness of the mixture (*i.e.*, methanol + Alq₃) can be significantly thicker than the initial Alq₃-film thickness. This thesis does not directly compare the effect of the needle thickness in experiments and simulations; note, however, that thicker Alq₃-films correspond to thinner

substrate.

dimensionless needle-heights, h_{solid} .

6.2.6 Influence of initial concentration, ϕ_0

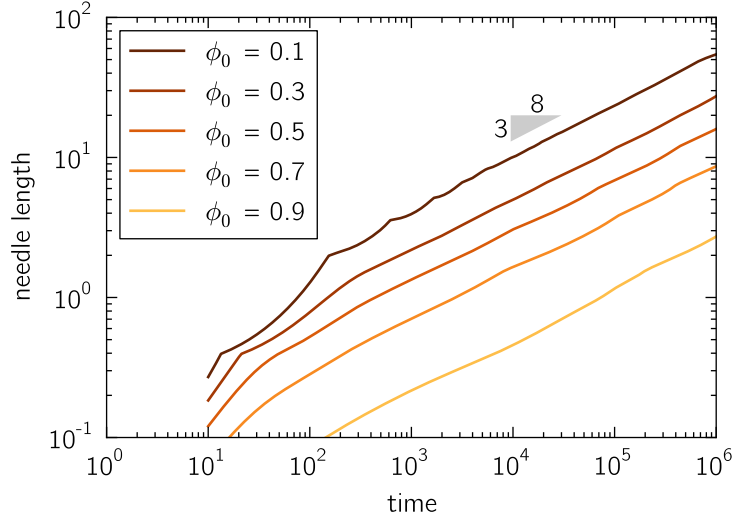


Figure 6-9: Needle evolution for different initial concentrations, ϕ_0 , and $\alpha = 0.01$, $h_{\text{solid}} = 4$, and $\varepsilon = 0.5$. The growth exponent is the same for all ϕ_0 , but films with lower solvent concentrations grow faster than those with higher concentrations. The jagged behavior for $\phi_0 = 0.1$ for early time is a result of numerical instabilities for fast-growing needles.

In simulations, the initial concentration, ϕ_0 , does not affect the growth exponent, but it does alter the needle velocity. From the Stefan condition (Eq. (2.17)), we know the needle velocity is proportional to the concentration gradient. The dimensionless concentration is 1 at the tip; thus, lower values of ϕ_0 produce sharper concentration gradients and faster growing needles, as shown in Fig. 6-9.

Although the needle grows faster for lower ϕ_0 , the growth exponent, γ , is unaffected; in other words, the slopes in Fig. 6-9 are the same for all ϕ_0 . Instead, if we say that needle lengths grow as $L_{\text{needle}} \approx At^\gamma$, then Fig. 6-9 shows that A is a function of ϕ_0 .

Note that the above considers the variation of concentration *while holding all other parameters constant*. In practice, varying the concentration can alter the material properties of the mixture; this, in turn, would alter the transport coefficient, α .

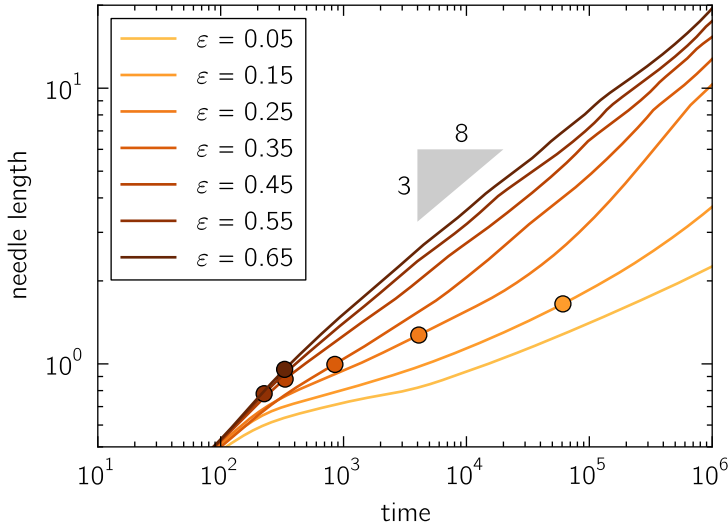


Figure 6-10: Needle evolution for different equilibrium thickness, ε , and $\alpha = 0.01$, $h_{\text{solid}} = 4$, and $\phi_0 = 0.5$. The growth exponent is the same for all ε , but films with smaller equilibrium thicknesses have a longer transient. Circular markers denote the characteristic dewetting time, $\hat{\tau}_*$, for each curve.

6.2.7 Influence of equilibrium film thickness, ε

In simulations, the equilibrium film thickness, ε , does not affect the growth exponent, but it does alter the duration of the transient regime, as shown in Fig. 6-10. This transient period is related to spinodal dewetting (see §2.2.5). The characteristic time for dewetting, $\hat{\tau}_*$, is a function of ε , as described by equation Eq. (5.4). $\hat{\tau}_*$ is marked on each curve (with a filled circle). Note that $\hat{\tau}_*$ denotes a characteristic time for dewetting to *start*; the transient regime extends beyond this time until dewetting is complete.

Recall that the thin film is linearly unstable for an equilibrium film thickness $\varepsilon < 3/4$ (as discussed in 5.1.1). For $\varepsilon > 3/4$, the film remains flat and diffusion dominates since fluid flow is minimal. Figure 6-10 only considers simulations in the unstable regime where the thin film breaks up into drops.

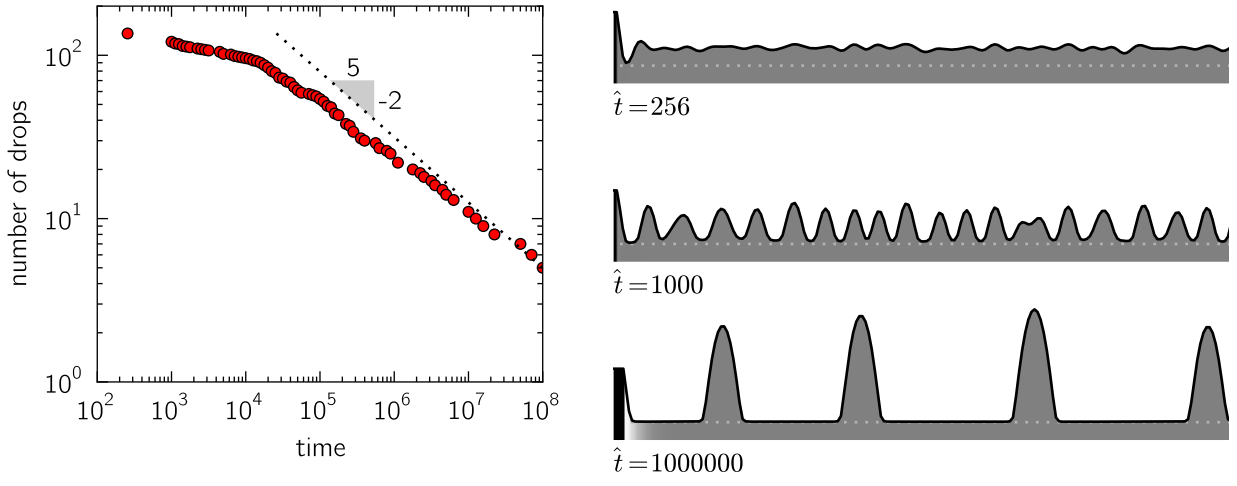
6.3 Dewetting and coarsening

In the presence of an attractive intermolecular pressure, thin fluid films are subject to a dewetting instability, which causes a thin film to break up into many, small droplets (for an extended discussion, see §2.2.5 and §5.1.1). Over time, these small droplets tend to combine

to form fewer, larger droplets in order to reduce surface energy; this process is known as coarsening (as discussed in §2.2.6 and §5.1.2).

6.3.1 Dewetting and coarsening in simulations

We can predict a characteristic time for dewetting, $\hat{\tau}_*$, based on Eq. (5.4). For the majority of simulations in this thesis $\varepsilon = 0.5$ (with the exception of the data presented in §6.2.7), such that the characteristic time for dewetting instability to develop is $\hat{\tau}_* = 256$. As shown in Fig. 6-11(b), this characteristic time marks the *initiation* of dewetting—drops are just beginning to form at this time.



(a) Number of drops in a film of dimensionless length 3000. After a transient period, the number of drops roughly decays as $N \sim t^{-2/5}$, as predicted.

(b) Region of film near the needle tip showing the initiation of dewetting at $\hat{t} = \hat{\tau}_* = 256$ (top), and how coarsening affects the drop size and spacing at $\hat{t} = 1000$ and $\hat{t} = 10^6$.

Figure 6-11: Droplet dewetting and coarsening in simulation with dimensionless domain size 3000 and needle height $h_{\text{solid}} = 2$.

Coarsening drives small drops to coalesce into fewer, larger droplets as shown in Fig. 6-11(b). In the absence of a growing needle tip, coarsening diminishes the number of drops, N , such that $N \sim t^{-2/5}$ (Eq. (5.9)). For thin needles—where the needle height is comparable to drop heights—the needle does not noticeably affect coarsening, and coarsening proceeds as if the needle is not present, as shown in Fig. 6-11(a).

6.3.2 Dewetting and coarsening in experiments

In experiments, the initially-uniform thin film breaks up into dark drops, as shown in Fig. 3-1. To get an approximation for the spacing between drops, we can substitute the material parameters for *methanol* (see Tbl. C.2) into Eq. (5.5), such that $\tilde{\lambda}_0 \approx 1$ to $10\ \mu\text{m}$. In experiments, the smallest-observed wavelength was $\tilde{\lambda}_0 \approx 1\ \mu\text{m}$, which is roughly the resolution of the images captured during annealing (as discussed in §6.6.1). The initial instability could, however, produce smaller drops/wavelengths that are not observed because of this optical limitation.

Coarsening in experiments is minimal: The wavelength of drops appears to double over the course of most experiments.⁹ The slow coarsening behavior matches that of thermally-annealed polymer films, which exhibit coarsening that is slowed compared to experimental time scales [92].

As discussed in §2.2.6, coarsening is caused by either drop collapse or drop collision; this difference is governed by the equilibrium thin-film thickness,¹⁰ ε (see Glasner [37]). Collision dominates for small ε , and collapse dominates as $\varepsilon \rightarrow 1$. To match experiments, simulation parameters are set to limit coarsening to the collapse-dominated regime.

6.4 Growth of the wetting layer

For very large needles, we predict that the wetting layer grows faster than the typical separation between drops. The analysis in §5.5.1, however, has a major flaw: it relies on a time-invariant thickness of the wetting layer. This section accounts for a time-varying ε and compares the growth of the wetting layer from simulations to that predicted in §5.5.1. In experiments, the wetting layer at the needle tip is no more than a few micron in length; because of optical limitations (see §6.6.1), the wetting layer was not measured in experiments.

⁹Drop sizes after the initial dewetting appear to be smaller than the resolution of the images, so it is difficult to measure coarsening in these experiments.

¹⁰A dimensionless parameter, C , is defined in Glasner [37]: $C \equiv K/\ln R \sim 1/\varepsilon\sqrt{|\ln \varepsilon|}$. When $C \lesssim 10$, collisions are negligible compared to collapse. When $C \gtrsim 10$, collisions become more common and $C \gtrsim 100$, collisions dominate.

6.4.1 Variation of the wetting-layer thickness for large h_{solid}

When the magnitude of the meniscus pressure (P_m) is large, the low pressure at the meniscus reduces the thickness of the wetting layer below the equilibrium value, such that $h_{\min} < \varepsilon$ (see Fig. 6-12). This variation is negligible when calculating the flux, Q_{wet} : $Q_{\text{wet}} \sim \varepsilon^3/L_{\text{wet}}$, but, since $L_{\text{wet}} \sim \varepsilon^3$, the dependence on ε cancels.¹¹ Variations in ε do, however, alter the scaling of L_{wet} .

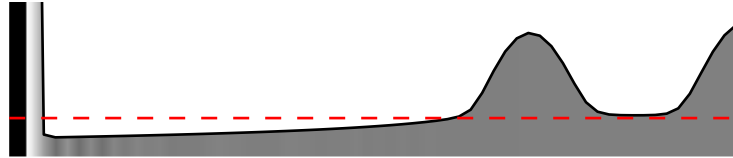


Figure 6-12: Wetting-layer for very large needle heights. The red, dashed line marks the equilibrium film-thickness, ε . Needle and meniscus (left) extend above the frame. The large needle height produces a wetting layer that drops well below ε to match to the low pressure in the meniscus. Note that the film connecting the two drops on the left has a thickness $\sim \varepsilon$.

Since the wetting layer is nearly flat, the pressure is dominated by intermolecular forces, such that $\Pi(h_{\min}) \approx P_m(h_{\min})$. For large-negative and large-positive pressures, the thickness and pressure are readily related by power laws,¹² but this is not true for pressures around zero. To *approximate* a power law, we take the logarithm of the intermolecular pressure, Eq. (4.9), and expand that expression using a Taylor series.¹³

$$r = \frac{d(\log P)}{d(\log h)} \Big|_{h=h_{\min,0}} = \frac{-3h_{\min,0}^{-3} + 4h_{\min,0}^{-4}}{h_{\min,0}^{-3} - h_{\min,0}^{-4}},$$

such that $h_{\min} \sim P_m^{1/r}$. For large, negative pressures, films are much thinner than the equilibrium thickness, ε , and $h_{\min} \sim P_m^{-1/4}$. As the pressure approaches zero, the thin film approaches ε , and r approaches infinity, such that $h_{\min} \rightarrow P_m^0$ (*i.e.*, h_{\min} is approximately constant, with respect to pressure). But for moderate pressures,¹⁴ $-8 < r < -5$, such that

¹¹Equation (5.21) gives $L_{\text{wet}} \sim \varepsilon^3 \dot{P}_1^{-1} P_m^3 \sim \varepsilon^3$.

¹² $P_m \sim h^{-4}$ when $h \ll 1$, and $P_m \sim h^{-3}$ when $h \gg 1$

¹³Actually, you have to replace h with $\eta = \log h$ and expand the logarithm of the intermolecular pressure about some arbitrary value of $\eta_0 = \log h_{\min,0}$. Otherwise, you'd get an expression for $d(\log P)/dh$ instead of $d(\log P)/d(\log h)$.

¹⁴These pressures and film thicknesses are quite reasonable in theory. Recall that $P_m \sim -h_{\text{solid}}/L_m^2$; in simulations, the length of the meniscus rarely goes below unity and the height of the solid goes from 2 to 32. For $r = -5$, $P_m = -8$ and $h_{\min} = \varepsilon/2$, and for $r = -8$, $P_m = -0.5$ and $h_{\min} = 0.8\varepsilon$.

$P_m^{-1/8} < h_{\min} < P_m^{-1/5}$. Now replace ε in Eq. (5.21) with a time varying h_{\min} , such that L_{wet} gives $t^{0.34} < L_{\text{wet}} < t^{0.44}$.¹⁵

6.4.2 Growth of the wetting layer in simulations

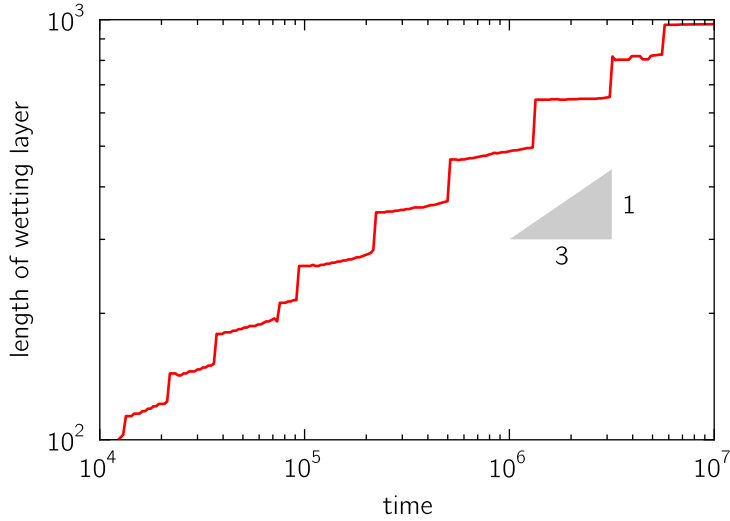


Figure 6-13: Growth of wetting layer, which separates the needle tip and the droplet region. The discrete jumps in the length correspond to the collapse of the drop nearest the needle tip; after a collapse, the wetting-layer length increases discontinuously by the spacing separating the first and second drops.

As shown in Fig. 6-13, the predicted scaling of the wetting layer, $t^{0.34} < L_{\text{wet}} < t^{0.44}$, matches well with simulations. Note that the wetting layer grows by discrete increments: when the drop nearest the needle collapses, L_{wet} extends to the next-nearest drop. See Fig. 5-7 for a graphical description.

6.5 Crystal nucleation and morphology in experiments

In experiments, multiple crystal needles tend to nucleate around a common nucleation site, as shown in Fig. 6-14. These needles are rectangular in shape for thin films, but for thicker films, the needle shape becomes irregular.

¹⁵As noted before, the flux through the wetting layer is relatively unchanged, remaining between $t^{0.29}$ and $t^{0.30}$ in this range.

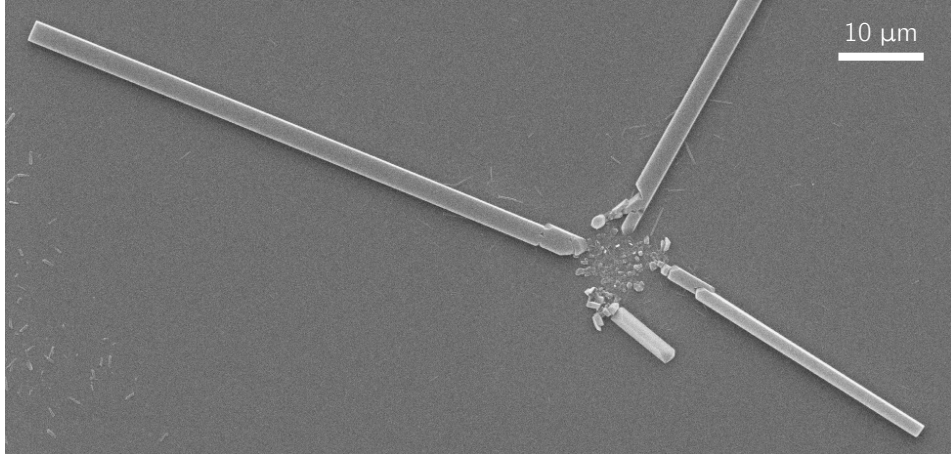


Figure 6-14: SEM image of needles growing from a common nucleation site after solvent-annealing a film with $\tilde{h}_{\text{Alq}} = 15 \text{ nm}$.

6.5.1 Nucleation sites and hole formation

Experiments reveal that crystal needles tend to nucleate in clusters. These nucleation sites are observed well before the first observable needles, as shown in Fig. 6-15. At early times, the nucleation sites appear as clear spots with an irregular edge, *i.e.*, a splotch.

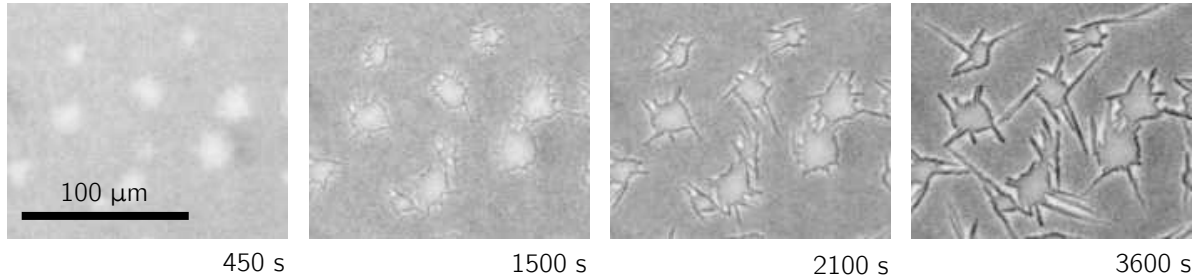


Figure 6-15: Possible hole formation in thick Alq_3 films. For a 60 nm thick Alq_3 -film, annealing produced clear, roughly-circular regions at early times. The edges of these clear regions served as nucleation sites for needles.

One possible cause of these splotches is the nucleation of holes in the fluid film, as discussed in §2.2.5. Although splotches were sometimes observed in thin films, as shown in Fig. 6-16, they were more common and more densely packed in thicker films, as shown in Fig. 6-15. This trend matches theoretical predictions, which suggest that thicker films are more likely to dewet due to nucleation of holes rather than spinodal-dewetting.

The splotches shown in Fig. 6-16 are similar in appearance to the holes in the simulations and experiments of Becker *et al.* [4] (see Fig. 2-10). Their simulations and experiments

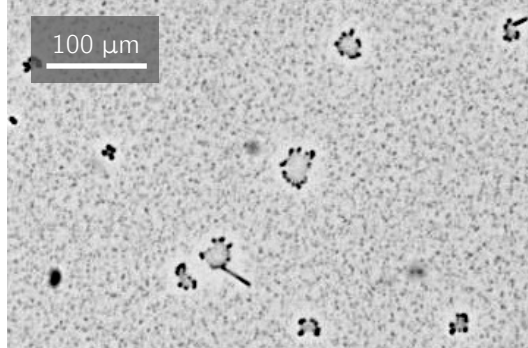


Figure 6-16: Micrograph of splotches on a substrate after annealing a 15 nm Alq₃ film for 1 hour. Although not apparent here, these splotches tend to be nucleation sites for needles, as shown in Fig. 6-15.

demonstrated that growing holes form a ridge of excess fluid around the hole-perimeter. This build-up of fluid could explain how needles can grow to be significantly thicker than the initial Alq₃ film, as discussed in §6.2.5.

6.5.2 Influence of solvent concentration on nucleation

In addition to the solvent-vapor annealing experiments, we conducted wetting experiments, where one end of the substrate contacted a reservoir of liquid solvent, as shown in Fig. 6-17. These experiments suggest that nucleation is concentration-dependent. Near the liquid reservoir, crystal nucleation was minimal, while farther away, many crystals nucleated. Very far away (not shown), the film took on the appearance of droplets with no noticeable needles. These results suggest that there is an optimal concentration for needle nucleation: for low solvent-concentration, the driving force for nucleation is high (analogous to high supercooling in melts), but the mobility of Alq₃ is low; conversely, for high solvent-concentration, the mobility is high, but the driving force is low. Thus, we expect higher nucleation at intermediate concentrations, as demonstrated in these wetting experiments.

6.5.3 Anisotropy of needle growth

In experiments, Alq₃ tends to solidify into single-crystal, high-aspect-ratio needles, as shown in Fig. 6-14. Note that Alq₃-needle formation is not specific to these experiments. Alq₃-needle formation is exhibited in single-crystals grown from physical-vapor deposition [96] and liquid solutions of Alq₃ and solvent [12]. Thus, it is likely that Alq₃ has a kinetic anisotropy

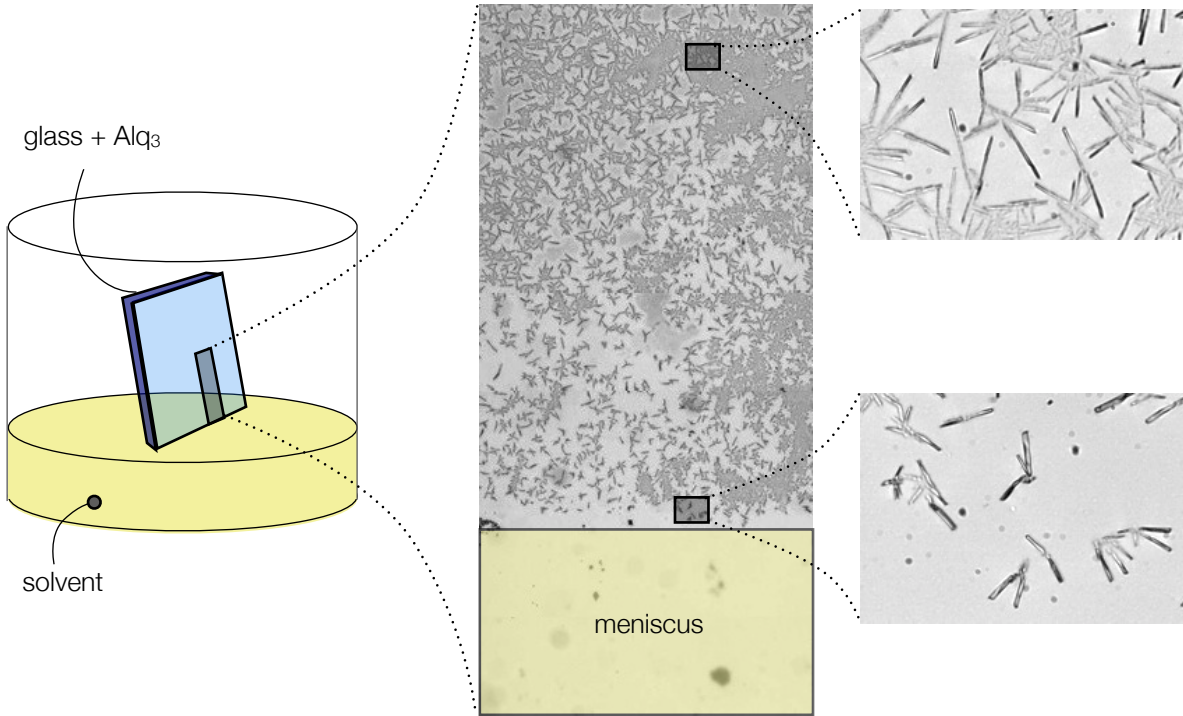


Figure 6-17: Micrograph from wetting experiment. Glass substrate is held vertically above liquid solvent. Solvent wets the substrate creating a concentration gradient with more solvent near the bottom edge and less solvent up the substrate.

(*e.g.*, an anisotropic surface energy) that leads needle growth [41] (for an extended discussion, see Balluffi, Allen, and Carter [3, §14.2]).

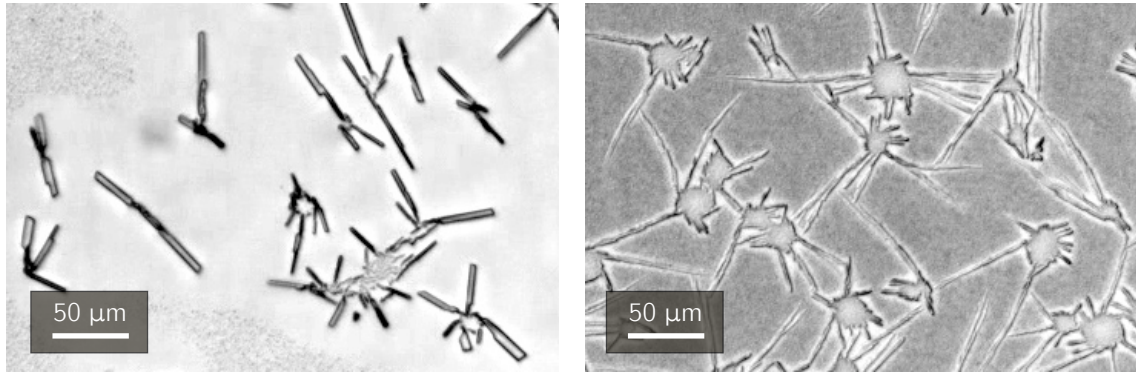
6.5.4 Splintering needles for thick Alq_3 -films

Needle widths varied little between $\tilde{h}_{\text{Alq}} = 15 \text{ nm}$ and $\tilde{h}_{\text{Alq}} = 30 \text{ nm}$, as shown in Fig. 6-4.¹⁶ This result is similar to experiments by Datar *et al.* [19], who observed that thicker films of PE-PTCDI¹⁷ produced longer—but not thicker/wider—needles.

When $\tilde{h}_{\text{Alq}} = 60 \text{ nm}$, however, there was a noticeable change in the crystal morphology, as shown in Fig. 6-18(b). These needles tended to have sharp (as opposed to flat) needle tips. These needles were also more likely to branch, or “splinter”, than those for thinner Alq_3 -films. This splintering produced curved needles, as each splinter was slightly misaligned with the original needle.

¹⁶The width-variation between needles on the *same* substrate is noticeable, but on average, the width is relatively constant with respect to \tilde{h}_{Alq} —except for $\tilde{h}_{\text{Alq}} = 60 \text{ nm}$.

¹⁷propoxyethyl perylene tetracarboxylic diimide



(a) Rectangular needles for Alq₃-film thickness $\tilde{h}_{\text{Alq}} = 30 \text{ nm}$.
(b) Irregular, “splintered” needles for Alq₃-film thickness $\tilde{h}_{\text{Alq}} = 60 \text{ nm}$.

Figure 6-18: Crystal morphology for different Alq₃-film thicknesses, \tilde{h}_{Alq} . Most of the substrate in (a) is clear in contrast to (b), which is covered with droplets (gray in images). This difference suggests that the needles in (a) consume what little Alq₃ is on the thinner

Granasy *et al.* [41] showed that high supercooling (lower solvent-to-Alq₃ ratios) can distort the formation of needle-like crystals in crystallizing fluids. If solvent condensation is not proportional to the Alq₃-film thickness, thicker films could lead to lower solvent-concentrations and thus, higher supercooling.

6.6 Open issues

6.6.1 Resolution of micrographs taken during solvent annealing

All micrographs taken *during* solvent annealing were captured using an optical microscope; thus, the highest resolution possible is on the order of a micron because the resolution is limited by diffraction [43, §10.2.6].

This limitation is particularly unfortunate when measuring liquid drops. Initially, the substrate is covered by an Alq₃-film with uniform thickness. When this film dewets, we expect to see drops with a typical spacing given by Eq. (5.5) at a characteristic time Eq. (5.6). These measurements would provide an experimental measure of the film thickness (after solvent mixing) since $\tilde{\lambda}_* \sim \tilde{h}_0^2$ and $\tilde{\tau}_* \sim \tilde{h}_0^5$ [82].

The drop size can also be useful for measuring the intermolecular pressure. The pressure in the ultra-thin film must (approximately) equal the pressure in the drop. By relating drop

heights to drop pressure using surface tension, one can extract the functional form of the intermolecular pressure. Kim *et al.* [52] used this technique to measure the intermolecular pressure in polymer films.

In the present study, imaging (during solvent-vapor annealing) is limited to optical microscopy because the substrate must be surrounded by a solvent-vapor atmosphere. This constraint makes it difficult for microscopy techniques that require a physical probe (*e.g.*, atomic force microscopy) or a low-pressure environment (*e.g.*, scanning electron microscopy). Although these techniques can (and were) used *after* annealing, the resulting micrographs are not an accurate measurement of the film morphology *during* solvent-vapor annealing.

6.6.2 Faster-than- $t^{1/2}$ needle growth in experiments

In experiments, some needles grew faster than $t^{1/2}$ (see *e.g.*, Fig. 6-3). This behavior may be explained by a two-dimensional, needle-growth analysis.

For one-dimensional needle growth, solvent that is not incorporated into the growing Alq₃-needle is rejected in front of the needle. This build-up of solvent inevitably leads to a slowing of needle growth.

In two-dimensions, a needle can grow towards regions with more Alq₃, and leave behind Alq₃-depleted fluid (which, can go around the sides of the needle tip). In this manner, the concentration profile in front of the needle tip can reach a steady-state. With the concentration profile fixed in time, the concentration gradient at the needle tip will be time-invariant, and the needle velocity will be constant. In other words, the needle tip will grow linearly in time—significantly faster than 1D-diffusion-limit, $L_{\text{needle}} \sim t^{1/2}$. A more complete analysis of this behavior is presented in Balluffi *et al.* [3, §20.2.2].

This result suggests an explanation for variations in growth-exponents: skinnier (small needle-width) needles could promote 2D transport, while wider needles could promote 1D transport (our one-dimensional model is equivalent to the growth of a semi-infinite plane in two dimensions). Unfortunately, optical resolutions (see §6.6.1) limited measurement of needle widths, which were at most a few micron.

6.6.3 The lubrication approximation

In this thesis, we make the assumption that $H \ll L$ (see §2.2.1) and use lubrication theory to derive the thin-film equations (Eq. (4.15)). Experiments show drops that are about a micron in diameter (see *e.g.*, Fig. 3-1), and the height of drops is on the order of a micron since optical microscopes are diffraction limited.¹⁸ These measurements suggest slopes close to unity, which does not match the long-wave approximation.

Nevertheless, there is evidence to suggest that lubrication theory is a good approximation even when the small-slope assumption fails [17]. In particular, simulations of the Stokes equations by Mazouchi and Homsy [61] revealed surprising agreement with lubrication theory despite sharp steps in topography.

6.6.4 Concentration-dependent material properties

The dimensionless governing equations—Eq. (4.3), Eq. (4.7), and Eq. (4.11)—allow concentration-dependent material properties in the form of concentration-dependent dimensionless parameters $\mathcal{S}(\phi)$, $\mathcal{A}(\phi)$, $\mathcal{D}(\phi)$, and $\varepsilon(\phi)$. Similarly, the numerical code developed for this thesis (and the finite-difference equations presented in Appendix B) is written to allow concentration-dependent material properties.¹⁹ Nevertheless, the simulation *results* presented in this thesis are in terms of the rescaled governing equations, Eq. (4.15), which only allow for constant α -values.

6.6.5 Meniscus at the needle tip

Experiments show that the fluid wets the needle (see *e.g.*, Mascaro *et al.* [59, Fig. 3c]). In this thesis, we assume that the fluid wets the needle *tip* such that the height of the liquid, at the solid/liquid interface, matches that of the solid; *i.e.*, $h_{\text{tip}} = h_{\text{solid}}$. Alternatively, the fluid could creep onto the top of the needle such that height of the fluid at the needle tip is

¹⁸Measuring drop sizes after the experiment is not ideal since drop sizes could change significantly when the solvent has evaporated.

¹⁹Hamaker constant A_{SLV} , dimensional equilibrium-thickness $\tilde{\varepsilon}$, surface tension σ , and diffusivity D can be non-constant (*e.g.*, concentration-dependent or spatially-varying). Note, however, that the finite-difference equations assume constant viscosity, μ , and density ρ .



Figure 6-19: Comparison of menisci at the needle tip. (Left) A meniscus where the fluid wets the tip of needle, such that the height of the fluid matches that of the needle. (Right) A meniscus where the fluid wets the entire needle, such that the height of the fluid at the needle tip is larger than the needle.

greater than that of the needle; *i.e.*, $h_{\text{tip}} > h_{\text{solid}}$. These two scenarios are depicted on the left and right of Fig. 6-19.

Note, however, that the fluid on top of the needle should be very thin due to intermolecular forces; *i.e.*, it should be on the order of ε . If $h_{\text{solid}} \gg \varepsilon$, these two wetting scenarios are indistinguishable. In either case, the shape of the meniscus is governed by the pressure in the film, as discussed in §5.5.1.

6.6.6 Intermolecular pressure exponents

In this thesis, the intermolecular pressure is described by a 3-4 potential (see §4.3), as is common in the literature on dewetting films [38, 35, 74]. Other popular potentials include the 2-3 potential [90, 39] and the 3-9 potential [38, 39].

The 3-9 potential represents the Lennard-Jones potential (integrated three times) and leads to a very thin equilibrium thickness, ε ; so thin, in fact, that it produces an adsorbed film, in which transport is governed by diffusion rather than hydrodynamics [73, §VI]. Experimental images from Mascaro *et al.* [59] suggest films that are tens of nanometers thick; sufficiently thick for continuum methods.

In the 2-3 potential, the h^{-2} -term represents the effects of a “diffuse electric double-layer”, which captures ionic-electrostatic and charge-dipole interactions [91]. In experiments, we have a polar solvent, methanol (Alq_3 is non-polar); thus, the 2-3 potential may be a better representation. This change in potential alters the wavelength and time-scale of the dewetting instability described in §5.1.1. Nevertheless, all other results in this thesis are unaffected by a change of exponents; the dynamics of the system are governed by coarsening, which is not dependent on the exact form of the intermolecular pressure (see §5.1.2).

6.6.7 Retarded van der Waals interactions

We use an intermolecular pressure (Eq. (4.9)) with an attractive van der Waals term that scales as h^{-3} . This relation, however, assumes that van der Waals interactions between any pair of molecules are not screened by the presence of other molecules; *i.e.*, van der Waals interactions are non-retarded. For films thicker than about 10 nm, retardation makes the strength of interactions significantly weaker, such that van der Waals interactions come into the pressure as h^{-4} [82].

Chapter 7

Conclusions and Outlook

In order to integrate single-crystal organic semiconductors into practical (opto)electronic devices, we need to understand the physics of crystal growth from thin films. In this thesis, we investigated the growth of single-crystal needles of Alq₃ from amorphous Alq₃-films that were annealed in methanol vapor. To understand the growth process, we developed a physical model describing solidification from thin-film liquid mixtures. Finally, we derived scaling laws that provide physical insight into the growth behavior in numerical simulations.

Growing Alq₃ needles were imaged during solvent-vapor annealing. Upon solvent-vapor annealing, the initially-uniform Alq₃-film formed drops and nucleated crystal needles. Needle growth exhibited a power-law behavior, with the needle length scaling as $L_{\text{needle}} \sim t^\gamma$. To understand this behavior, we developed a mathematical model to describe these morphological changes—both drop formation and needle growth—during solvent-vapor annealing. The governing equations were solved numerically, and the resulting 1D simulations qualitatively matched experimental observations.

The governing equations were rescaled to produce a dimensionless transport coefficient, α , which relates diffusion to coarsening. For high α -values (diffusion-dominated regime), the needle length scaled as $L_{\text{needle}} \sim t^{1/2}$; this growth matches the theory of 1D, diffusion-dominated solidification. For low α -values (coarsening-dominated regime), we identified two sub-regimes: 1) small needles (*i.e.*, $h_{\text{solid}} \lesssim \langle h_{\text{drop}} \rangle$) with needle lengths scaling as $L_{\text{needle}} \sim t^{2/5}$, and 2) large needles (*i.e.*, $h_{\text{solid}} \gg \langle h_{\text{drop}} \rangle$), with $L_{\text{needle}} \sim t^{0.29}$. Needle growth in these low α -regimes were dominated by fluid flux driven by droplet collapse, *i.e.*,

coarsening. In order to test the validity of this analysis, we varied the thickness of the Alq₃ film, \tilde{h}_{Alq} , since $\alpha \sim \tilde{h}_0^{-2} \sim \tilde{h}_{\text{Alq}}^{-2}$. The measured growth-exponents fell into the predicted range, and increased with increasing α , as predicted.

The remaining parameters in the system—equilibrium thickness, ε , and initial solvent-concentration, ϕ_0 —did not influence the growth-exponent, γ , but altered the behavior nonetheless. Increasing ε decreased the dewetting time, $\hat{\tau}_*$, as predicted from linear-stability analysis. Increasing the solvent-concentration, ϕ_0 , reduced the concentration gradient at the needle tip and thus, slowed needle growth by reducing the coefficient A , in $L_{\text{needle}} \approx At^\gamma$.

Simulations reproduced predicted dewetting and coarsening behavior. Dewetting initiates at the predicted time scale and wavelength. For small needles, the fluid film coarsens such that the number of drops scale as $N \sim t^{-2/5}$, as predicted by Glasner and Witelski [38]. For large needles, low pressure at the needle tip promotes drop collapse and forms a wetting layer, which grows as $t^{0.34} < L_{\text{wet}} < t^{0.44}$.

This thesis describes the fundamental physical processes that govern the growth of Alq₃ needles. Although experiments were conducted on a single system—Alq₃-methanol-glass—the results should be applicable to many molecule-solvent-substrate systems. In other words, the behavior of the system is governed by a set of dimensionless parameters, which could be tuned using different molecules, solvents, and substrates.

Future Work

This thesis suggests a number of future directions.

Controlling nucleation Preliminary experiments suggest that there is an optimal solvent-concentration for nucleation. Thus, one could control nucleation by controlling annealing pressure and temperature to adjust vapor-concentration; similarly, cooling the substrate promotes condensation of solvent vapor.

Material properties for Alq₃/methanol mixture This thesis does not make a direct comparison between experiments and simulations because many material properties are unknown. In particular the equilibrium film-thickness, surface-tension, viscosity, diffusivity,

and Hamaker constant for the Alq₃/methanol mixture are unknown. Knowing these properties could guide solvent selection.

Simulations with concentration-dependent material properties Preliminary simulations with concentration-dependent, dimensionless Hamaker constants (*i.e.*, $\mathcal{A}(\phi)$) demonstrate wetting-layer formation at the needle tip. This result suggests a systematic study of simulations with $\mathcal{A}(\phi)$, $\mathcal{S}(\phi)$, $\mathcal{D}(\phi)$, and $\varepsilon(\phi)$.

Two-dimensional simulations As discussed in §6.6.2, one-dimensional transport limits growth rates to $t^{1/2}$ (or slower). Modifying the simulations for a two-dimensional domain would allow the growing needle tip to consume Alq₃ from a larger area and reject solvent behind the growing tip. 2D simulations would more accurately model experimental observations.

Alq₃-solvent solubility The needles grown in this thesis did not coarsen as the P30T¹ needles in Xiao *et al.* [102] or dissolve like the Alq₃-chloroform needles in Mascaro [58]. This suggests that methanol is less soluble in Alq₃ than chloroform. Simulations in this thesis did not exhibit needle shrinkage, which requires interacting needles (for coarsening) or the addition of solvent during growth.²

¹poly(3-octylthiophene)

²Simulations conserved the initial mass of Alq₃ and solvent. With solvent-condensation after $t = 0$, the solvent-concentration could exceed the concentration at the needle tip and lead to shrinkage.

Appendix A

Phase transitions and equilibria

The physics discussion presented in Chapter 2 is organized relative to the steps in the experiment. There is, however, further insight to be gained by presenting a unified discussion of the various phase transitions and equilibria that occur during the experiment.

A.1 Nucleation of drops, holes, and solids

When phase-change is energetically favorable, nucleation of the lower-energy phase will lower the bulk energy, but it also creates an interfacial boundary between the two phases. This interface adds an energetic penalty. As a result, there tends to be a critical nucleus where the energy reduction due to phase change balances the energy increase due to the creation of the phase boundary (as discussed in §2.3.1). In the present study, nucleation phenomena can be found during condensation (*e.g.*, the water drops on the side of a cold glass), dewetting (as discussed in §2.2.5), and solidification (as discussed in §2.3.1).

A.2 Coarsening in liquid drops and separated phases

In Chapter 2, we discussed coarsening of drops. Similar coarsening phenomena is observed during phase-separation; for example, the growth of carbon-dioxide bubbles in beer, the solidification of solid particles from its melt, and the phase separation of alloys. Here we compare the coarsening of liquid drops (found in solvent-annealing experiments) to coarsen-

ing in a phase-separated mixture.

A.2.1 Coarsening of a phase-separated mixture

Consider a spherical particle (with radius R) of one phase growing in a bulk phase. The Stefan condition (recall §2.3.3) states that the growth of the particle (*i.e.*, the radial velocity of the surface, v_r) is proportional to the concentration gradient normal to spherical particle:

$$v_r \sim \frac{\partial \phi}{\partial r}$$

Integrating this velocity over the surface of the spherical particle gives the mass change of this seed

$$\frac{\partial m}{\partial t} \sim v_r R^2 \sim R^2 \frac{\partial \phi}{\partial r} \quad (\text{A.1})$$

The concentration gradient scales as

$$\frac{\partial \phi}{\partial r} \sim \frac{\langle \phi \rangle - \phi(R)}{R}$$

where $\langle \phi \rangle$ is the mean-field concentration, and $\phi(R)$ is the equilibrium concentration around the growing particle.

For a flat interface, local equilibrium requires that the concentration on the bulk-side of the interface is fixed at ϕ_{flat} . For curved interfaces, this equilibrium value is altered due to the Gibbs-Thomson effect, such that $\phi(R) \approx \phi_{\text{flat}}(1 + 2\gamma\Omega/kTR)$. Thus, we can simplify the concentration-gradient to

$$\frac{\partial \phi}{\partial r} \sim \frac{1}{R(\langle \phi \rangle - R)} \sim R^{-2} \quad (\text{A.2})$$

To find a rate equation for the seed radius, we relate the mass and the sphere radius by geometry, $m \sim R^3$, and apply the chain rule, which gives

$$\frac{\partial R}{\partial t} \sim \frac{\partial m}{\partial t} \frac{\partial R}{\partial m} \sim \frac{\partial m}{\partial t} R^{-2} \quad (\text{A.3})$$

By combining Eq. (A.1), Eq. (A.2), and Eq. (A.3), we find

$$\frac{\partial R}{\partial t} \sim R^{-2} \quad (\text{A.4})$$

Separating variables and integrating gives

$$R \sim t^{1/3} \quad (\text{A.5})$$

A.2.2 Comparison between coarsening of drops and particles

Although coarsening of liquid drops (§5.1.2) and coarsening of phase-separated particles (§A.2.1) are physically similar, the resulting scaling laws are quite different. For a more direct comparison, we rewrite the equations from §5.1.2 in terms of the drop size H . We can relate the drop height to the drop-pressure, ¹ drop-volume, and separation distance² as

$$P \sim H^{-1}$$

$$m \sim H^2$$

$$\langle L \rangle \sim \langle H \rangle^2$$

The resulting scaling laws for both drop-coarsening and particle-coarsening are summarized in Tbl. A.1. The main difference between scaling laws stems from their differences in dimensionality: The mass of a drop is proportional to the square of its height; in contrast, the mass of a particle is proportional to the cube of its radius. Another difference lies in the driving force: for drop-coarsening, fluid flows between adjacent drops with separation L (which scales as H^2); for particle-coarsening, diffusion exchanges mass between a particle and a mean-field. Note that the distance from a particle to the mean-field is approximately R , while the distance to the characteristic distance to nearest particle is approximately R^3 .

¹ $H \sim PW^2$, where the width of the drop scales like $W \sim P^{-1}$. See Glasner and Witelski [38, §II] for details.

²Note that the drop mass should scale the same as the separation distance: given a series of equally-spaced drops with equal mass, the collapse of every-other drop would double the drop separation and double the size of the remaining drops (assuming the mass from the collapsed drops is equally distributed).

	drops	particles
characteristic size	H	R
evolution equation	$\frac{\partial H}{\partial t} \sim \frac{\partial m}{\partial t} \frac{\partial H}{\partial m}$	$\frac{\partial R}{\partial t} \sim \frac{\partial m}{\partial t} \frac{\partial R}{\partial m}$
driving force	$\frac{\partial m}{\partial t} \sim \frac{P - \langle P \rangle}{\langle L \rangle} \sim \frac{1}{H^3}$ $P \sim H^{-1}$	$\frac{\partial m}{\partial t} \sim \frac{\phi - \langle \phi \rangle}{R} \sim \frac{1}{R^2}$ $\phi \sim R^{-1}$
mass relation	$m \sim H^2$	$m \sim R^3$
size evolution	$H \sim t^{1/5}$	$R \sim t^{1/3}$

Table A.1: Comparison of drop-coarsening and particle-coarsening

Appendix B

Finite-difference formulations

For posterity, I present a detailed record of the finite-difference formulations used in this thesis. There is no reason to read through this chapter unless you are interested in reimplementing this solver, or you want to check my error-prone math.

The majority of the analysis in this thesis uses the rescaled equations of motion (*i.e.*, Eq. (4.15)), but the numerical simulations are implemented with the dimensionless equations Eq. (4.3), Eq. (4.7), and Eq. (4.11). Using these un-rescaled equations, the numerical solver can handle concentration-dependent surface-tension, Hamaker constant, and diffusivity.

B.1 Nomenclature



Figure B-1: Nodes (circles) and interfaces (dotted lines) on the computational mesh.

To simplify the notation for describing finite differences, we adopt the notation shown in Fig. B-1. Node values are points on a mesh at $j = 0$ to N . Following the notation of Patankar [77], we label the values at the j th node with subscript P (present node or point), the $j + 1$ node with subscript E (east), and the $j - 1$ node with subscript W (west). In addition, we denote the interfaces to the east and west of P with subscripts e ($j + \frac{1}{2}$) and w

$(j - \frac{1}{2})$, respectively. For certain calculations (e.g., third derivatives), more node values are needed, so we also introduce subscripts $E2$ ($j + 2$) and $W2$ ($j - 2$) to label second-nearest neighbors. This set of node points ($E2, E, P, W, W2$) is referred to as a finite-difference stencil.

At times, it is convenient to write equations in terms of the i th interface with a node labeled R to its right, and L to its left. Combining this interface-centered notation with the node-centered notation above, we find that $(u_R)_e = u_E$, $(u_L)_w = u_W$, and $(u_L)_e = (u_R)_w = u_P$. In other words, $(u_R)_e$ translates to “ u -value to the right of the eastern interface”. Although, this notation may seem cumbersome, it significantly simplifies some of the expressions below.

B.2 Newton's Method of root-finding

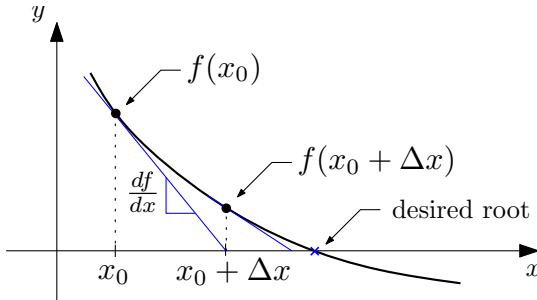


Figure B-2: Arbitrary function, $f(x)$ near root. To find the root, choose an initial point x_0 and find the slope df/dx at that point. By extending a line with slope df/dx to the x -axis, we march closer to the root.

Suppose we are given some continuous function $f(x)$, which we can differentiate to give df/dx . Our goal is to find the point(s), x_r , where $f(x_r) = 0$; in other words, we want the root(s) of $f(x)$. We first choose an arbitrary point along the curve, x_0 . Assuming $f(x)$ has a root and $f(x_0) \neq 0$ (otherwise, we need to look no further), there is some Δx for which

$$0 = f(x_r) \approx f(x_0 + \Delta x). \quad (\text{B.1})$$

We can approximate Eq. (B.1) using the first two terms of the Taylor series expansion:

$$f(x_0) + \left. \frac{df}{dx} \right|_{x_0} \Delta x \approx 0$$

Solving for Δx , we have

$$\Delta x = \frac{-f(x_0)}{\frac{df}{dx}|_{x_0}}. \quad (\text{B.2})$$

We can see from Fig. B-2, that $f(x_0 + \Delta x) \neq 0$, but this new point is *closer* to zero¹. We then iterate, to find the desired zero.

The algorithm is summarized below.

1. Given $f(x)$, find df/dx .
2. Choose a starting point x_0 .
3. Calculate $\Delta x = \frac{-f(x_0)}{\frac{df}{dx}|_{x_0}}$.
4. Calculate $f(x_0 + \Delta x)$.
 - If this is close enough to zero, DONE.
 - Otherwise, let $x_0^{\text{new}} = x_0 + \Delta x$ and start over from step 3.

Of course, the definition of “close enough” to zero depends on the problem and the desired accuracy.

B.3 Jacobian

The description of root finding in §B.2 applies to a function of one variable. For multiple variables (*e.g.*, h_j and ϕ_j : the height and concentration of the thin film at mesh point, j), the derivative, $df/dx|_{x_0}$, is replaced by the Jacobian, $\underline{\underline{\mathbf{J}}}$ —the matrix of first-order partial derivatives. (Note that $\underline{\underline{\mathbf{J}}}$ denotes the Jacobian, while J denotes solvent flux.) Note also, that we consider a pair of coupled equations, such that f becomes a vector

$$\underline{f}^T = \begin{bmatrix} \cdots & (f_h)_j & (f_\phi)_j & \cdots \end{bmatrix}$$

Thus, Eq. (B.2) becomes

$$\Delta \underline{u} = -\underline{\underline{\mathbf{J}}}^{-1} \underline{f}(\underline{u}_0) \quad (\text{B.3})$$

¹It will not always be the case that $f(x_0 + \Delta x)$ is closer to zero than $f(x_0)$ – this has to do with the stability of this root-finding method (see Hamming [42]).

where the Jacobian and vector of unknowns have the form

$$\underline{u}^T = [\dots \ h_{j-1} \ \phi_{j-1} \ h_j \ \phi_j \ h_{j+1} \ \phi_{j+1} \ \dots] \quad (\text{B.5})$$

$$\Delta \underline{u}^T = \begin{bmatrix} \dots & \Delta h_{j-1} & \Delta \phi_{j-1} & \Delta h_j & \Delta \phi_j & \Delta h_{j+1} & \Delta \phi_{j+1} & \dots \end{bmatrix} \quad (\text{B.6})$$

The remainder of this appendix is dedicated to solving for the derivatives that make up the Jacobian.

B.4 Discretization of thin-film equations in 1D

The nonlinearity of Eq. (4.3) and Eq. (4.7) suggests that a numerical solution would be appropriate. To that end, we discretize these equations using centered finite-differences in space and backward-Euler steps in time.

B.4.1 Discretization of film thickness equation

We can solve the thin-film equation as a flux-conservative, initial-value problem [78, §19.1] by rewriting Eq. (4.1) as

$$f_h = \frac{h_P - h_P^{\text{old}}}{\Delta t} + \frac{1}{\Delta x} (Q_e - Q_w) = 0 \quad (\text{B.7})$$

Note that Q_w for node P is equivalent to Q_e for node $P - 1$. Thus, instead of writing out separate expressions for Q_e and Q_w , we write a single Q_i , which is the flux at the i th interface.

$$Q_i = -p'_i h_i^3, \quad p'_i = \frac{p_R - p_L}{\Delta x} \quad (\text{B.8})$$

The pressure to the right of the i th interface is

$$p_R = -\mathcal{S}_R h''_R - \mathcal{A}_R \psi_R \quad (\text{B.9})$$

where $\psi_R = (\varepsilon/h_R)^n - (\varepsilon/h_R)^m$, such that $\mathcal{A}\psi$ is the intermolecular pressure Eq. (4.9). For p_L , simply replace all subscripts R with the subscript L .

Combining the last few expressions together gives

$$Q_i = \frac{h_i^3}{\Delta x} (\mathcal{S}_R h''_R + \mathcal{A}_R \psi_R - \mathcal{S}_L h''_L - \mathcal{A}_L \psi_L) \quad (\text{B.10})$$

The value of the thin-film thickness at an interface, and its second finite-difference can be calculated as

$$h_i = \frac{h_R + h_L}{2}, \quad (\text{B.11a})$$

$$h''_R = \frac{h_{R2} - 2h_R + h_L}{\Delta x^2}, \quad \text{and} \quad h''_L = \frac{h_R - 2h_L + h_{L2}}{\Delta x^2} \quad (\text{B.11b})$$

Note that the interface values, h_i , should never be used to compute second (or higher order) derivatives, as discussed in §B.4.2.

The Jacobian for the thin-film equation (Eq. (B.7)) is found by taking derivatives with respect to all h -values (*i.e.*, h_P , h_E , h_W , h_{E2} , h_{W2}) and ϕ -values (*i.e.*, ϕ_P , ϕ_E , ϕ_W). A list of these terms, plus a table of the front factors multiplying these terms is given in Tbl. B.1 and Tbl. B.2. The tables simplify the terms by defining

$$\frac{\partial \psi}{\partial h} \equiv -nh^{-(n+1)} + mh^{-(m+1)} \quad (\text{B.12})$$

$$p'_i \equiv \mathcal{S}_R h''_R + \mathcal{A}_R \psi_R - \mathcal{S}_L h''_L - \mathcal{A}_L \psi_L \quad (\text{B.13})$$

Note that p'_i is not-quite a finite first-derivative since it is missing a $1/\Delta x$.

	$\frac{\partial f_h}{\partial h_{W2}}$	$\frac{\partial f_h}{\partial h_W}$	$\frac{\partial f_h}{\partial h_P}$	$\frac{\partial f_h}{\partial h_E}$	$\frac{\partial f_h}{\partial h_{E2}}$
$\frac{1}{\Delta t}$			1		
$\frac{3}{2\Delta x^2} h_e^2 p'_e$			1	1	
$\frac{3}{2\Delta x^2} h_w^2 p'_w$		-1	-1		
$\frac{1}{\Delta x^4} h_e^3 (\mathcal{S}_R)_e$			1	-2	1
$-\frac{1}{\Delta x^4} h_e^3 (\mathcal{S}_L)_e$		1	-2	1	
$\frac{1}{\Delta x^4} h_w^3 (\mathcal{S}_R)_w$		-1	2	-1	
$-\frac{1}{\Delta x^4} h_w^3 (\mathcal{S}_L)_w$	-1	2	-1		
$\frac{1}{\Delta x^2} h_e^3 (\mathcal{A}_R \partial \psi_R)_e$				1	
$-\frac{1}{\Delta x^2} h_e^3 (\mathcal{A}_L \partial \psi_L)_e$				1	
$\frac{1}{\Delta x^2} h_w^3 (\mathcal{A}_R \partial \psi_R)_w$				-1	
$-\frac{1}{\Delta x^2} h_w^3 (\mathcal{A}_L \partial \psi_L)_w$				-1	

Table B.1: Table of coefficients for principal terms in Jacobian. Note that a variable at a node to the left of an eastern interface is equivalent to that variable at a node to the right of a western interface. For constant coefficients, the second derivative terms can be combined into a single third derivative.

	$\frac{\partial f_h}{\partial \phi_W}$	$\frac{\partial f_h}{\partial \phi_P}$	$\frac{\partial f_h}{\partial \phi_E}$
$\frac{1}{\Delta x^4} h_e^3 \left(\frac{\partial \mathcal{S}}{\partial \phi} _R h''_R \right)_e$			1
$-\frac{1}{\Delta x^4} h_e^3 \left(\frac{\partial \mathcal{S}}{\partial \phi} _L h''_L \right)_e$		1	
$\frac{1}{\Delta x^4} h_w^3 \left(\frac{\partial \mathcal{S}}{\partial \phi} _R h''_R \right)_w$		-1	
$-\frac{1}{\Delta x^4} h_w^3 \left(\frac{\partial \mathcal{S}}{\partial \phi} _L h''_L \right)_w$	-1		
$\frac{1}{\Delta x^2} h_e^3 \left(\frac{\partial \mathcal{A}}{\partial \phi} _R \psi_R \right)_e$			1
$-\frac{1}{\Delta x^2} h_e^3 \left(\frac{\partial \mathcal{A}}{\partial \phi} _L \psi_L \right)_e$		1	
$\frac{1}{\Delta x^2} h_w^3 \left(\frac{\partial \mathcal{A}}{\partial \phi} _R \psi_R \right)_w$		-1	
$-\frac{1}{\Delta x^2} h_w^3 \left(\frac{\partial \mathcal{A}}{\partial \phi} _L \psi_L \right)_w$	-1		

Table B.2: Coefficients for Jacobian terms of solvent-mass equation (ϕ -derivatives)

B.4.2 Interface values—a word of warning

The unknowns of interest are solved on points known as nodes or cell-centers. For certain equations, we require the values at the cell-centers *and* at the interfaces between these cells;

in this instance, we use an arithmetic mean.² For example

$$h_e = h_{P+\frac{1}{2}} = \frac{h_P + h_E}{2}$$

Note that interface values should not be used to construct a finite-second-difference; doing so would artificially increase the magnitude of the derivative. For example:

$$\frac{\partial^2 h}{\partial x^2} \approx \frac{h_e - 2h_P + h_w}{(\Delta x/2)^2} = \frac{2h_P + 2h_E - 8h_P + 2h_P + 2h_W}{\Delta x^2} = 2 \frac{h_E - 2h_P + h_W}{\Delta x^2}$$

which gives *twice* the “normal” centered finite-second-difference.³ On the other hand, these interface values give the same finite-first-difference as a centered finite-first-difference.

B.5 Discretization of convection-diffusion equation

The finite-difference form of the solvent-mass equation (Eq. (4.4)) can be written as

$$f_\phi = \frac{(\phi h)_P - (\phi h)_P^{\text{old}}}{\Delta t} + \frac{1}{\Delta x} (J_e - J_w) = 0 \quad (\text{B.14})$$

Again, we take advantage of the fact that the solvent flux (Eq. (4.5)) J_w for node P is equivalent to J_e for node $P - 1$ and write a single J_i , which is the flux at i th interface:

$$J_i = -\mathcal{D}_i h_i \left(\frac{\partial \phi}{\partial x} \right)_i + \phi_i Q_i \quad (\text{B.15})$$

where the expression for Q_i was given in Eq. (B.10).

All that remains is to take derivatives of Eq. (B.14) with respect to all the variables in the stencil (*i.e.*, h_j and ϕ_j), as shown in Tbl. B.3 and Tbl. B.4. These derivatives make up the entries in the Jacobian.

²When using material properties at the interfaces, we should be using the harmonic mean [77, §4.2-3] given by $D_e = \frac{2D_P D_E}{D_P + D_E}$.

³This increase in magnitude can be reasoned as follows: the arithmetic mean assumes a linear variation between P and E (and between P and W). Thus, the curvature between W and E would be artificially constrained between w and e .

	$\frac{\partial f_\phi}{\partial h_{W2}}$	$\frac{\partial f_\phi}{\partial h_W}$	$\frac{\partial f_\phi}{\partial h_P}$	$\frac{\partial f_\phi}{\partial h_E}$	$\frac{\partial f_\phi}{\partial h_{E2}}$
$\frac{1}{\Delta t} \phi_P$			1		
$\frac{1}{2\Delta x} \mathcal{D}_e \phi'_e$			-1	-1	
$\frac{1}{2\Delta x} \mathcal{D}_w \phi'_w$		1	1		
$\frac{3}{2\Delta x^2} h_e^2 \phi_e p'_e$			1	1	
$\frac{3}{2\Delta x^2} h_w^2 \phi_w p'_w$		-1	-1		
$\frac{1}{\Delta x^4} h_e^3 \phi_e (\mathcal{S}_R)_e$			1	-2	1
$-\frac{1}{\Delta x^4} h_e^3 \phi_e (\mathcal{S}_L)_e$		1	-2	1	
$\frac{1}{\Delta x^4} h_w^3 \phi_w (\mathcal{S}_R)_w$		-1	2	-1	
$-\frac{1}{\Delta x^4} h_w^3 \phi_w (\mathcal{S}_L)_w$	-1	2	-1		
$\frac{1}{\Delta x^2} h_e^3 \phi_e (\mathcal{A}_R \partial \psi_R)$				1	
$-\frac{1}{\Delta x^2} h_e^3 \phi_e (\mathcal{A}_L \partial \psi_L)_e$				1	
$\frac{1}{\Delta x^2} h_w^3 \phi_w (\mathcal{A}_R \partial \psi_R)$				-1	
$-\frac{1}{\Delta x^2} h_w^3 \phi_w (\mathcal{A}_L \partial \psi_L)_w$				-1	

Table B.3: Table of coefficients for principal terms in Jacobian for the solvent-transport equation. All terms are the same those in Tbl. B.1 with the addition of a factor of ϕ .

B.6 No-flux boundary condition at right edge

During the solution of the governing equations, we enforce no-flux boundary conditions at the right edge of the fluid domain. This no-flux boundary condition is equivalent to a symmetry boundary condition with zero first- and third-derivatives of the film thickness, h (see [38]), and zero first-derivative of the solvent concentration, ϕ . This symmetry condition is shown schematically in Fig. B-3.

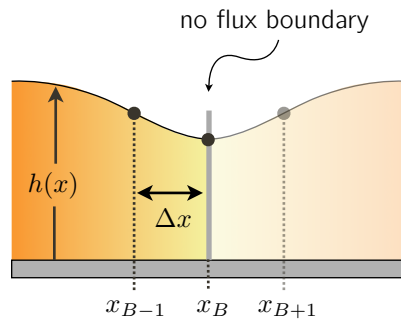


Figure B-3: Schematic of no-flux boundary condition at right boundary.

	$\frac{\partial f_\phi}{\partial \phi_W}$	$\frac{\partial f_\phi}{\partial \phi_P}$	$\frac{\partial f_\phi}{\partial \phi_E}$
$\frac{1}{\Delta t} h_P$		1	
$\frac{1}{\Delta x^2} \mathcal{D}_e h_e$		-1	1
$\frac{1}{\Delta x^2} \mathcal{D}_w h_w$	1	-1	
$-\frac{1}{2\Delta x} h_e \phi'_e \left(\frac{\partial \mathcal{D}}{\partial \phi} \Big _R \right)_e$			1
$-\frac{1}{2\Delta x} h_e \phi'_e \left(\frac{\partial \mathcal{D}}{\partial \phi} \Big _L \right)_e$		1	
$-\frac{1}{2\Delta x} h_w \phi'_w \left(\frac{\partial \mathcal{D}}{\partial \phi} \Big _R \right)_w$		-1	
$-\frac{1}{2\Delta x} h_w \phi'_w \left(\frac{\partial \mathcal{D}}{\partial \phi} \Big _L \right)_w$	-1		
$\frac{1}{2\Delta x} Q_e$		1	1
$\frac{1}{2\Delta x} Q_w$	-1	-1	
$\frac{1}{\Delta x^4} h_e^3 \left(\phi \frac{\partial \mathcal{S}}{\partial \phi} \Big _R h''_R \right)_e$			1
$-\frac{1}{\Delta x^4} h_e^3 \left(\phi \frac{\partial \mathcal{S}}{\partial \phi} \Big _L h''_L \right)_e$		1	
$\frac{1}{\Delta x^4} h_w^3 \left(\phi \frac{\partial \mathcal{S}}{\partial \phi} \Big _R h''_R \right)_w$		-1	
$-\frac{1}{\Delta x^4} h_w^3 \left(\phi \frac{\partial \mathcal{S}}{\partial \phi} \Big _L h''_L \right)_w$	-1		
$\frac{1}{\Delta x^2} h_e^3 \left(\phi \frac{\partial \mathcal{A}}{\partial \phi} \Big _R \psi_R \right)_e$			1
$-\frac{1}{\Delta x^2} h_e^3 \left(\phi \frac{\partial \mathcal{A}}{\partial \phi} \Big _L \psi_L \right)_e$		1	
$\frac{1}{\Delta x^2} h_w^3 \left(\phi \frac{\partial \mathcal{A}}{\partial \phi} \Big _R \psi_R \right)_w$		-1	
$-\frac{1}{\Delta x^2} h_w^3 \left(\phi \frac{\partial \mathcal{A}}{\partial \phi} \Big _L \psi_L \right)_w$	-1		

Table B.4: Table of coefficients for principal terms in Jacobian for the solvent-transport equation.

B.6.1 Thin-film equation

For no-flux boundaries, the Jacobian terms are altered, as shown in Tbl. B.5. The boundary conditions alter the Jacobian at the boundary points (as given in the table).

Since the third derivative uses a wide stencil, the points just-inside the boundaries are also affected by the boundary. Just-inside the right boundary (*i.e.*, when the boundary node B in Fig. B-3 is at the E -node), the normal finite-difference for the third derivative

$$-\frac{\mathcal{S}}{\Delta x^4} h_e^3 (-h_{W2} + 3h_W - 3h_E + h_{E2})$$

is rewritten

$$-\frac{\mathcal{S}}{\Delta x^4} h_e^3 (-h_{W2} + 3h_W - 3h_E + h_P)$$

reflecting the fact that the $E2$ -node lies outside the boundary, but must match node P to satisfy no-flux.

	$\frac{\partial f_h}{\partial h_{W2}}$	$\frac{\partial f_h}{\partial h_W}$	$\frac{\partial f_h}{\partial h_P}$
$\frac{1}{\Delta t}$			1
$\frac{3}{2\Delta x^2} h_w^2 p'_w$		-2	-2
$\frac{1}{\Delta x^4} h_w^3 (\mathcal{S}_R)_w$		-2	2
$-\frac{1}{\Delta x^4} h_w^3 (\mathcal{S}_L)_w$	-2	4	-2
$\frac{1}{\Delta x^2} h_w^3 (\mathcal{A}_R \partial \psi_R)_w$			-2
$-\frac{1}{\Delta x^2} h_w^3 (\mathcal{A}_L \partial \psi_L)_w$			-2

Table B.5: Table of coefficients for principal terms in Jacobian at right boundary for no-flux boundary conditions.

B.6.2 Solvent-mass equation

Assuming no-flux boundary conditions, Eq. (4.4) becomes

$$f_\phi|_L = \frac{(\phi h)_P - (\phi h)_P^{\text{old}}}{\Delta t} + \frac{2}{\Delta x} J_e = 0 \quad (\text{B.16a})$$

$$f_\phi|_R = \frac{(\phi h)_P - (\phi h)_P^{\text{old}}}{\Delta t} - \frac{2}{\Delta x} J_w = 0 \quad (\text{B.16b})$$

at the left and right boundaries (subscripts L and R , respectively). The corresponding derivatives at the boundaries are given in table Tbl. B.6

B.7 Boundary conditions at the growing needle tip

The boundary conditions at the needle tip are applied in two distinct steps. 1) The needle tip is fixed in position during the implicit solution of the unknowns, h and ϕ ⁴ during this

⁴If the needle tip were not fixed, the geometry changes of mesh would add a few extra terms to the Jacobian. More annoyingly, you'd have an extra equation for the velocity which would have to be moved around in the Jacobian in order to maintain the banded structure of the Jacobian.

	$\frac{\partial f_\phi}{\partial h_{W2}}$	$\frac{\partial f_\phi}{\partial h_W}$	$\frac{\partial f_\phi}{\partial h_P}$
$\frac{1}{\Delta t} \phi_P$			1
$\frac{3}{2\Delta x} \phi_w p'_w h_w^2$		2	2
$-\frac{1}{\Delta x^4} \mathcal{S} \phi_w h_w^3$	-2	8	-6
$-\frac{1}{\Delta x^2} \mathcal{A} \phi_w h_w^3 \partial \psi_w$		-2	2
$-\frac{1}{2\Delta x} \mathcal{A} \phi_w h_w^3 h'_w \partial^2 \psi_w$		2	2

Table B.6: Table of coefficients for principal terms in Jacobian on right boundary for no-flux boundary conditions.

time, the needle tip acts as a no-flux boundary. This first step is discussed in §B.7.2. After solving for h and ϕ , we grow the needle by treating it as a fixed-value or “absorbing” boundary. This second step is discussed in §B.7.3.

B.7.1 Discretization at the needle tip

As shown in Fig. B-4, we let the subscript b_0 denote the mesh node nearest the solid/liquid boundary of the needle tip; also, let b_1 denote the next node over; *i.e.*, $b_0 + 1$. Similarly, let the subscript i_0 denote the cell-interface at the needle tip, and let i_1 , i_2 be shorthand for $i_0 + 1$, $i_0 + 2$.

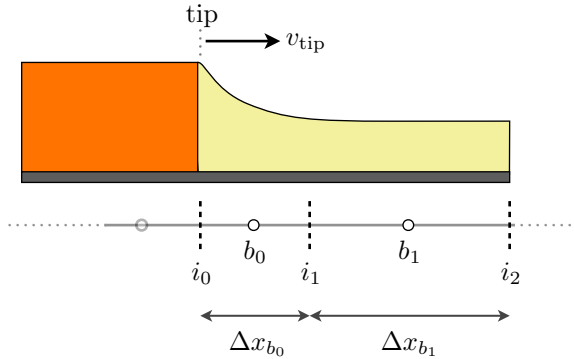


Figure B-4: Discretization of the region near the tip of a growing, 1D crystal.

Finally, we use the subscript “tip” to denote node values at the needle tip. Since, the needle tip acts as both a cell-interface and a mesh node, values at the tip are sometimes denoted by the subscript i_0 and, at other times, by “tip”. Alternatively, imagine a cell centered on the tip-node as shown in Fig. B-5. We can use linear interpolation between

values u_{tip} and u_{b_0} to arrive at a value for u_{i_0} (red dot in Fig. B-5). As $\Delta x_{\text{tip}} \rightarrow 0$, $u_{i_0} \rightarrow u_{\text{tip}}$.

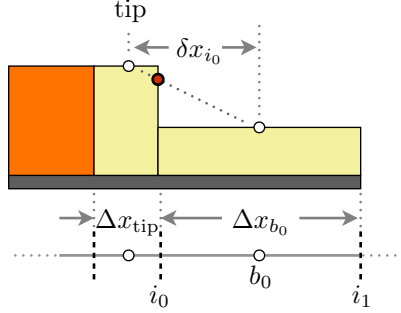


Figure B-5: Close up diagram of the tip-cell at the needle tip showing how values at tip are interpolated onto i_0 . In practice, this cell has zero width, such that $\Delta x_{\text{tip}} \rightarrow 0$.

As shown in the diagram above, the b_0 -node is precisely centered on its cell. Thus, as the needle grows, the cell width, $\Delta x_{b_0} = x_{i_1} - x_{i_0}$, shrinks. Similarly, the node-to-node distances near the needle tip, $\delta x_{i_0} = x_{b_0} - x_{i_0}$ and $\delta x_{i_1} = x_{b_0} - x_{i_1}$, shrink. All mesh nodes and cell-interfaces to the east of b_0 are unaffected by the needle, such that $\Delta x_{b_1} = \Delta x$.

As the tip-cell deforms due to the moving needle, the position of the tip-node (*i.e.*, x_{b_0}) is moved so that it is always at the center of the tip-cell. This convention produces more accurate node values as discussed in [77]. Furthermore, it implies that $\delta x_{i_0} = \Delta x_{b_0}/2$.

B.7.2 Solving the governing equations at the needle tip

During the implicit solutions of h and ϕ , no flux is allowed into the needle. Thus, the governing equations at b_0 are missing a flux from the left, such that

$$\frac{h_{b_0} - h_{b_0}^{\text{old}}}{\Delta t} + \frac{Q_{i_1}}{\Delta x_{b_0}} = 0 \quad (\text{B.17a})$$

$$\frac{(\phi h)_{b_0} - (\phi h)_{b_0}^{\text{old}}}{\Delta t} + \frac{J_{i_1}}{\Delta x_{b_0}} = 0 \quad (\text{B.17b})$$

Also note that the cell width at the needle tip is altered by the needle tip, as denoted by Δx_{b_0} .

Modified derivatives near the boundary

The geometry changes introduced by the growing needle alter the derivatives in the above equations. For example, the first derivatives for h at the cell-interfaces i_0 and i_1 depend on δx_{i_0} and δx_{i_1} instead of Δx as shown below.

$$h'_{i_0} = \frac{h_{b_0} - h_{\text{tip}}}{\delta x_{i_0}}, \quad h'_{i_1} = \frac{h_{b_1} - h_{b_0}}{\delta x_{i_1}}$$

Furthermore, the curvature at the b_0 -node becomes

$$h''_{b_0} = \frac{1}{\Delta x_{b_0}} \left(\frac{h_{b_1} - h_{b_0}}{\delta x_{i_1}} - \frac{h_{b_0} - h_{\text{tip}}}{\delta x_{i_0}} \right)$$

This second difference is simply the difference of the first-differences divided by the distance between the interfaces, $x_{i_1} - x_{i_0} = \Delta x_{b_0}$. Finally, a slight modification is made to the curvature at the b_1 -node:

$$h''_{b_1} = \frac{1}{\Delta x} \left(\frac{h_{b_2} - h_{b_1}}{\Delta x} - \frac{h_{b_1} - h_{b_0}}{\delta x_{i_1}} \right)$$

Implicit equations at the needle tip

The modified governing equations given by Eq. (B.17) are not so different from the equations on the rest of the domain. However, most of the geometry changes introduced by the needle tip are hidden in the fluxes. At the i_1 -interface, the volumetric and solvent fluxes are

$$\begin{aligned} Q_{i_1} &= -h_{i_1}^3 \frac{1}{\delta x_{i_1}} (p_{b_1} - p_{b_0}) \\ J_{i_1} &= -\mathcal{D}_{i_1} h_{i_1} \frac{\phi_{b_1} - \phi_{b_0}}{\delta x_{i_1}} + \phi_{i_1} Q_{i_1} \end{aligned}$$

Furthermore, the modified curvatures appear in the pressure equations:

$$\begin{aligned} p_{b_0} &= -\mathcal{S} \frac{1}{\Delta x_{b_0}} \left(\frac{h_{b_1} - h_{b_0}}{\delta x_{i_1}} - \frac{h_{b_0} - h_{\text{tip}}}{\delta x_{i_0}} \right) + \mathcal{A}\psi(h_{b_0}) \\ p_{b_1} &= -\mathcal{S} \frac{1}{\Delta x} \left(\frac{h_{b_2} - h_{b_1}}{\Delta x} - \frac{h_{b_1} - h_{b_0}}{\delta x_{i_1}} \right) + \mathcal{A}\psi(h_{b_1}) \end{aligned}$$

Finally, values at the interface must be interpolated between their nodal values (as was done in Fig. B-5) as follows⁵

$$\begin{aligned} h_{i_1} &= \left(1 - \frac{\Delta x}{2\delta x_{i_1}}\right) h_{b_1} + \frac{\Delta x}{2\delta x_{i_1}} h_{b_0} \\ \phi_{i_1} &= \left(1 - \frac{\Delta x}{2\delta x_{i_1}}\right) \phi_{b_1} + \frac{\Delta x}{2\delta x_{i_1}} \phi_{b_0} \\ \mathcal{D}_{i_1} &= \left(1 - \frac{\Delta x}{2\delta x_{i_1}}\right) \mathcal{D}_{b_1} + \frac{\Delta x}{2\delta x_{i_1}} \mathcal{D}_{b_0} \end{aligned}$$

At the next node over (*i.e.*, b_1), the governing equations are relatively unchanged, except that the above fluxes should replace the usual fluxes at the western cell-interface:

$$\begin{aligned} \frac{h_P - h_P^{\text{old}}}{\Delta t} + \frac{1}{\Delta x_{b_1}} (Q_e - Q_{i_1}) &= 0 \\ \frac{(\phi h)_P - (\phi h)_P^{\text{old}}}{\Delta t} + \frac{1}{\Delta x_{b_1}} (J_e - J_{i_1}) &= 0 \end{aligned}$$

B.7.3 Solving for the velocity at the needle tip

After solving the governing equations, we can grow the needle. This growth further modifies the values of h and ϕ at b_0 to balance the geometry changes and the Alq₃ absorbed by the needle.

Fixed-value (absorbing) boundary conditions at the needle tip

At the tip of the needle, we assume that the fluid wets the needle, such that $h_{\text{tip}} = h_{\text{solid}}$, as shown in Fig. B-4 and discussed in §6.6.5. In addition, we require fixed-values of concentration, ϕ_{solid} and ϕ_{tip} , at the solid and liquid sides of the needle tip, as discussed in §2.3.2. Thus, the two unknowns of the system, ϕ and h , are known at the liquid/crystal interface. As shown in Fig. 4-2, the dimensionless values of ϕ_{solid} and ϕ_{tip} are 0 and 1, respectively; in the following we use ϕ_{solid} and ϕ_{tip} to avoid confusion.

⁵By definition, nodes b_0 and b_1 are separated by a length δx_{i_1} . Since i_1 and b_1 are fixed in space, these points are always separated by a length $\Delta x/2$. Linear interpolation with these distances gives the equations shown above.

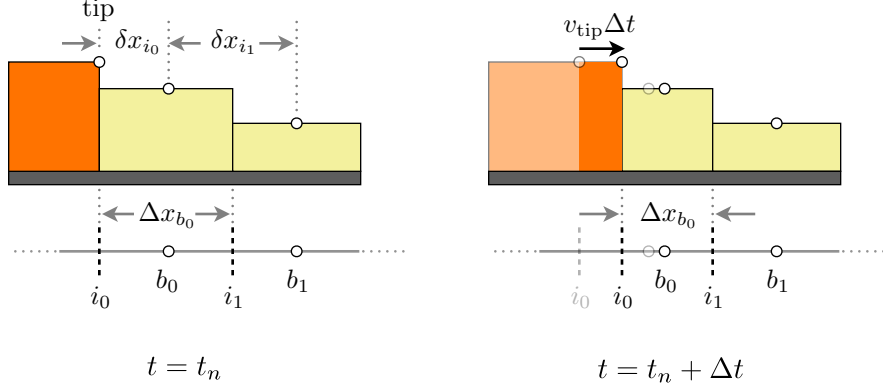


Figure B-6: As the needle grows, the adjacent cell must shrink to make room for the needle. This change of cell volume must be reflected in the discretization. Over the time period Δt , mass was added to the needle, with volume (per unit depth) $v_{\text{tip}}h_{\text{tip}}\Delta t$.

In contrast to the solution of the governing equations (see §B.7.2), this fixed-value boundary condition implies a non-zero flux at the needle tip.

Implicit solution of needle velocity

The needle velocity given by Eq. (4.13) can be written in finite-difference form as

$$v_{\text{tip}} = D_{i_0} \frac{\phi_{b_0} - \phi_{\text{tip}}}{\delta x_{i_0}} \quad (\text{B.18})$$

The growing needle changes the mesh geometry, as shown in Fig. B-6, such that

$$\delta x_{i_0} = \delta x_{i_0}^{\text{old}} - \frac{v_{\text{tip}}\Delta t}{2} \quad (\text{B.19a})$$

$$\Delta x_{b_0} = \Delta x_{b_0}^{\text{old}} - v_{\text{tip}}\Delta t \quad (\text{B.19b})$$

As Alq₃-rich fluid is absorbed into the needle both the height and concentration are altered, such that

$$h_{b_0}\Delta x_{b_0} = (h_{b_0}\Delta x_{b_0})^{\text{old}} - h_{\text{solid}}v_{\text{tip}}\Delta t \quad (\text{B.20a})$$

$$\phi_{b_0}h_{b_0}\Delta x_{b_0} = (\phi_{b_0}h_{b_0}\Delta x_{b_0})^{\text{old}} - \phi_{\text{solid}}h_{\text{solid}}v_{\text{tip}}\Delta t \quad (\text{B.20b})$$

We then solve Eq. (B.18), Eq. (B.19), and Eq. (B.20) simultaneously, *i.e.*, implicitly.

Pseudo-implicit velocity

The unknown values in this problem are given by the vector

$$\underline{x} = [v_{\text{tip}}, \Delta x_{b_0}, h_{b_0}, \phi_{b_0}]$$

These unknowns are associated with Eq. (B.18), Eq. (B.19) and Eq. (B.20); rewriting as a vector of equations, \underline{f} , with elements:

$$\begin{aligned} f_1 : & v_{\text{tip}}\Delta x_{b_0}/2 - D_{i_0}(\phi_{b_0} - \phi_{\text{tip}}) \\ f_2 : & \Delta x_{b_0} - \Delta x_{b_0}^{\text{old}} + v_{\text{tip}}\Delta t \\ f_3 : & h_{b_0}\Delta x_{b_0} - m + h_{\text{solid}}v_{\text{tip}}\Delta t \\ f_4 : & \phi_{b_0}h_{b_0}\Delta x_{b_0} - m_\phi + \phi_{\text{solid}}h_{\text{solid}}v_{\text{tip}}\Delta t \end{aligned} \quad (\text{B.21})$$

When the correct values of \underline{x} are substituted into the above, then $\underline{f}(\underline{x}) = 0$. We “guess” an initial value \underline{x}_0 and solve linear equation

$$\underline{f}(\underline{x}_0) + \underline{\underline{J}}\Delta\underline{x} \approx 0$$

with Jacobian

$$\underline{\underline{J}} = \begin{bmatrix} \Delta x_{b_0}/2 & v_{\text{tip}}/2 & 0 & -D_{i_0} \\ \Delta t & 1 & 0 & 0 \\ h_{\text{solid}}\Delta t & h_{b_0} & \Delta x_{b_0} & 0 \\ \phi_{\text{solid}}h_{\text{solid}}\Delta t & \phi_{b_0}h_{b_0} & \phi_{b_0}\Delta x_{b_0} & h_{b_0}\Delta x_{b_0} \end{bmatrix} \quad (\text{B.22})$$

where the rows match the equations in \underline{f} and the columns match the derivatives with respect to the variables in \underline{x} . This linear system is solved using Newton’s method, as discussed in §B.2.

B.7.4 Eating nodes

Since we have a moving needle tip, some mesh nodes must be transferred from the fluid domain to the solid domain. When the needle tip crosses a mesh node, we must take care

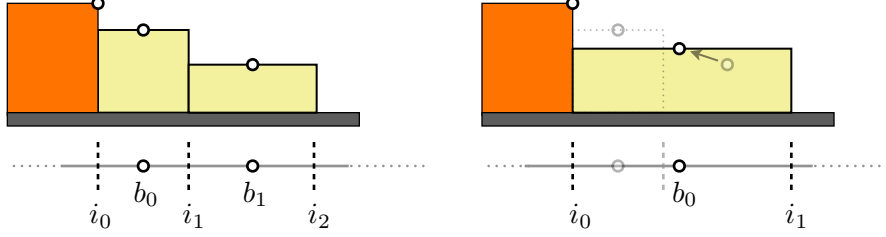


Figure B-7: Cells in the fluid domain before and after the needle eats a node. The heights of the yellow boxes represent the values of the unknown (either h or ϕ), and the orange box represents the needle.

to conserve mass. Figure B-7 shows the steps involved in destroying a node.

1. When needle growth causes Δx_{b_0} to shrink below some threshold (currently using $\Delta x/4$), it is time to “destroy” a node.
2. Combine the mass in the b_0 -cell with that in the b_1 -cell to make one super-node, which extends from i_0 to i_2 .
3. Mark the old b_0 -node as a solid node (instead of a fluid node) and make the old b_1 -node the new b_0 -node (making sure to center the node on the cell). Similarly, i_1 now designates the cell-interface previously labeled i_2 .

As the control volumes are combined, conservation of mass requires

$$(u_{b_0}\Delta x_{b_0})_{\text{new}} = (u_{b_0}\Delta x_{b_0} + u_{b_1}\Delta x_{b_1})_{\text{old}}$$

where $(\Delta x_{b_0})_{\text{new}} = (u_{b_0} + u_{b_1})_{\text{old}}$. After this eating procedure, the solution proceeds as normal.

Appendix C

Miscellaneous

C.1 Filtering needle growth data

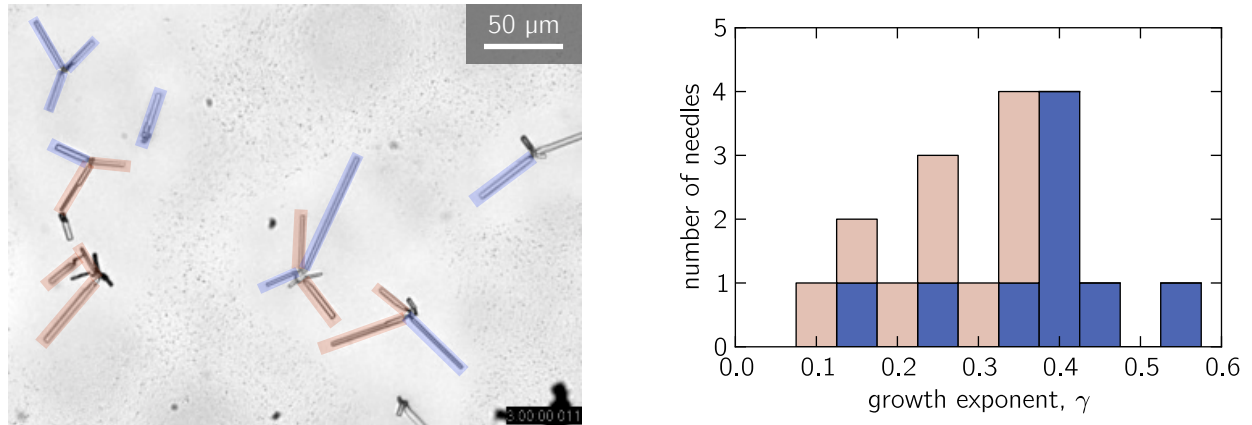


Figure C-1: Left: micrograph of needles with each needle labeled as either unobstructed (blue) or obstructed (red). Right: histogram of growth exponents from needles on left colors matching the overlay on the left.

Figure C-1 shows a micrograph of needles grown from a 15 nm Alq₃ film after annealing for 3 hours. Some needles are labeled as obstructed (red), which suggests that it interacts with other needles during growth. A needle was labeled as obstructed if the clear wetting layer of the needle collided with the wetting layer of an adjacent needle. Unobstructed needles are labeled in blue. The histogram on the right of Fig. C-1 shows the growth exponents for obstructed and unobstructed needles.

C.2 Measuring the growth-exponent in simulations

The growth-exponents described in §6.2 apply to intermediate times. Early- and late-time phenomena can alter γ , such that the analyses of §5.2, §5.3, §5.4, and §5.5 do not apply. As discussed in §6.2.7, there is a dewetting time before which growth-exponents, γ , vary continuously (*i.e.*, needle growth does not behave like a power-law). Other early- and late-time phenomena are discussed below.

C.2.1 Growth-exponent transition at late times

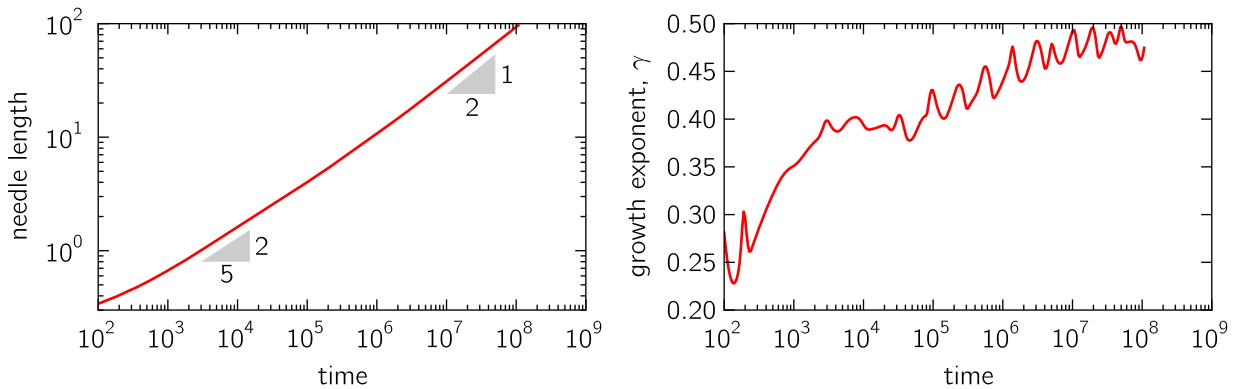


Figure C-2: Transition of growth-exponent, γ , at late times for $\alpha = 0.1$, $h_{\text{tip}} = 16.$, $\phi_0 = 0.5$, and $\varepsilon = 0.5$. The growth exponent, γ , is the slope in the needle length vs. time plot.

Low transport coefficients, α , suggest that coarsening dominates diffusion. Note, however, that droplet collapse slows down faster than diffusion. Thus, regardless of α -value, diffusion will dominate at sufficiently-late times. Figure C-2 demonstrates this transition in the growth exponent: at early time, $\gamma \approx 2/5$; at late time, $\gamma \rightarrow 1/2$. The oscillations in γ are a result of drop collapses as discussed in §C.2.3.

C.2.2 Numerical transient in needle growth

At very early times, the simulations display a transient growth that is linear in time. This transient is a numerical artifact and lasts until the diffusion front grows beyond the first few mesh points. In other words, this transient has a characteristic time of $\hat{\tau}_{\text{linear}} \sim \Delta\hat{x}^2/4\alpha$. Figure C-3 shows the transition from the numerical transient at early time to the steady

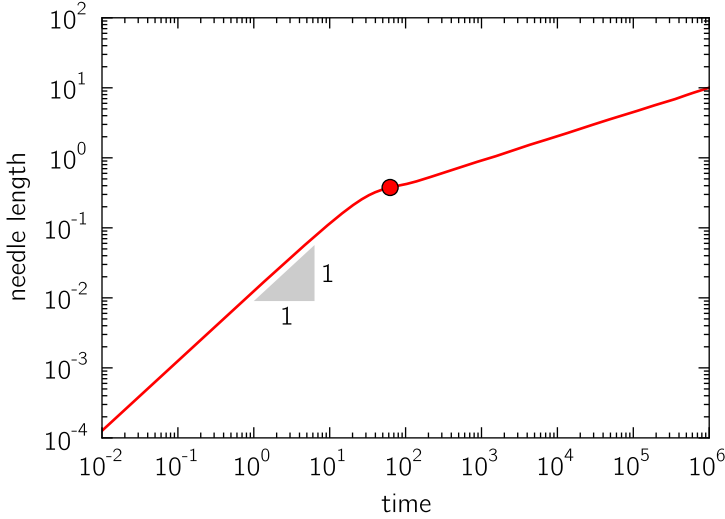


Figure C-3: Numerical transient in needle growth. At times less than $\hat{\tau}_{\text{linear}}$ (marked with a red dot), the needle grows linearly in time.

state growth at late time; as predicted, the time $\hat{\tau}_{\text{linear}}$ (marked with a red dot) separates these two regimes.

C.2.3 Perturbations in the growth-exponent due to drop collapse

At early times, the collapse of a drop has only a minor affect on needle growth because drops are significantly smaller than the needle. As time progresses, however, droplets grow to the size of the needle, and drop collapses near the needle noticeably perturb the growth exponent.

As shown in Fig. C-4, a drop collapse near the needle tip produces a jump in the growth-exponent: As the drop nearest the needle collapses, it pushes Alq₃-rich fluid toward the needle, thus increasing the growth-exponent. Not all of that fluid can be incorporated into the needle (or the meniscus); as this extra fluid is advected away, it stretches the concentration gradient and reduces the growth-exponent (below the steady state behavior).

For sufficiently large perturbations, it is not possible to reliably measure the growth exponent. This issue is exacerbated by low α -values: in this regime, diffusion is slow correct the concentration profile, which was distorted by the drop collapse. In other words, low a α -value prolongs the jump in the growth-exponent, shown in Fig. C-4. This disturbance

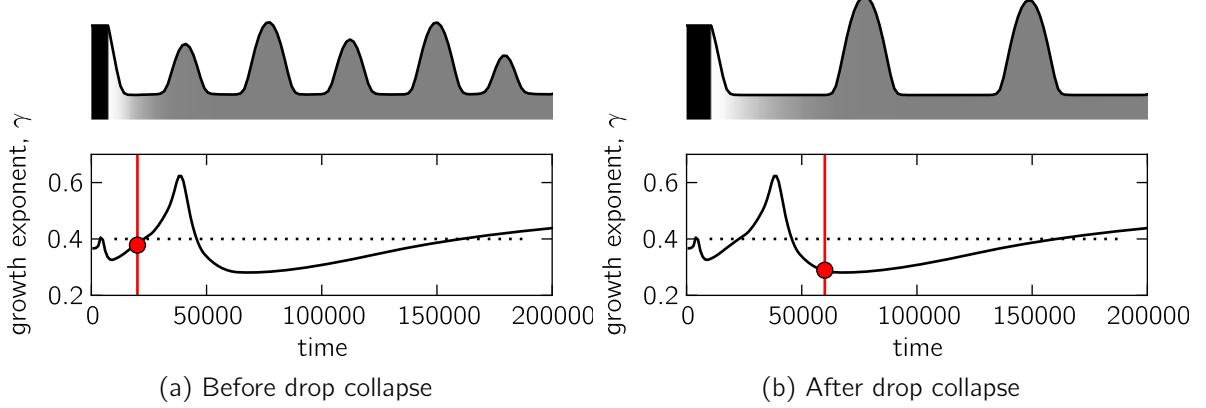


Figure C-4: Perturbation of the growth-exponent due to drop collapse. The red lines in the growth-exponent plots mark the time of the thin film plots above. A drop collapse near the needle tip produces a spike in the growth-exponent.

makes it difficult to extract reliable growth rates for short needles at very-low α -values.

C.3 Marangoni effects

C.3.1 Flows driven by Marangoni effects

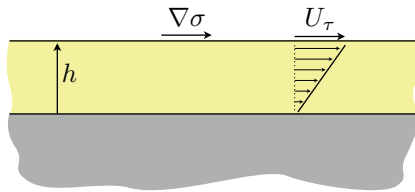


Figure C-5: Shear flow driven by the Marangoni effect

Surface-tension gradients are commonly found when a fluid film varies in composition [44] or temperature [89]. These gradients produce a shear stress along the free surface of the film, $\tau = \hat{t} \cdot \nabla\sigma$, where \hat{t} is the unit vector tangent to the free surface.¹ The resulting shear-induced flow is known as the Marangoni effect. In the absence of pressure gradients, the surface shear, τ , produces a Couette-like flow, as shown in Fig. C-5. The velocity at the

¹In the rest of this thesis, τ (with a subscript) is used to denote characteristic times (of various sorts). Here, we use τ to denote shear stress. Please pardon the inconsistency.

free surface can be related to the surface stress as

$$U_\tau \equiv \frac{\tau h}{\mu}. \quad (\text{C.1})$$

C.3.2 Marangoni effects vs. capillary effects

Integrating the velocity given by Eq. (C.1) gives a fluid flux that scales as $Q_\tau \sim \tau \varepsilon^2 / \mu$. To estimate the importance of Marangoni effects, we compare this flux to that arising from pressure gradients, which scales as $Q_p \sim (\partial p / \partial x) \varepsilon^3 / \mu$ (see Eq. (2.4)). Taking the ratio of these two fluxes, we find

$$\mathcal{M} = \frac{\tau}{\varepsilon(\partial p / \partial x)},$$

where Marangoni effects dominate for large values of \mathcal{M} and pressure-driven flow dominates for small values.

The Marangoni stress should scale like a characteristic change in surface tension $\Delta\sigma$ over a characteristic length L :

$$\tau \sim \frac{\Delta\sigma}{L}.$$

To estimate the pressure gradient, we take the pressure at the needle tip, which scales like h_{solid} / L_m^2 (where h_{solid} is the needle height, and L_m is the length of the meniscus; see §5.5.1). This pressure should act over a characteristic L , such that

$$\frac{\partial p}{\partial x} \sim \frac{1}{L} \frac{h_{\text{solid}}}{L_m^2}.$$

From experiments $h_{\text{solid}} \sim 10^{-7} \text{ m}$, $L_m \sim 10^{-7} \text{ m}$, and $\varepsilon \sim 10^{-8} \text{ m}$,² the surface tension of the mixture should scale as $\Delta\sigma \sim 10^{-2} \text{ N/m}$. Combining these approximations, we find³

$$\mathcal{M} \approx \frac{\Delta\sigma L_m^2}{\varepsilon h_{\text{solid}}} \approx 10^{-1}.$$

²The height of the needle was measured at about 500 nm, and the length of the meniscus should be roughly the same size. Alq₃ molecules are roughly a nanometer in size, so the ultra-thin film should be roughly an order of magnitude larger to accommodate flow of Alq₃ molecules.

³Typical fluids have surface tensions between 0.2 and 0.7 N/m, thus 0.1 N/m is a reasonable estimate of concentration differences.

This estimate suggests that flow driven by capillary pressure dominates Marangoni effects. But given that the above is a rough estimate, it is quite possible that Marangoni effects do influence flow in the present study. Nevertheless, this thesis ignores any contribution from Marangoni effects.

C.4 Cleaning procedure for silicon/glass wafers

Substrates must be cleaned before Alq₃-deposition. Substrates are loaded onto a substrate holder, which holds substrates vertically in glass beakers. Each beaker was filled with roughly 50 ml of solvent and either ultrasonicated or boiled as described in Tbl. C.1. Beakers should be rinsed appropriately (*i.e.*, rinse with water before filling with water or μ 90, with acetone before filling with acetone, and with isopropyl before filling with isopropyl).

step	cleaning solution	time	agitation
1	μ 90 cleaning solution	5 min	ultrasonication
2	deionized water	2 min	ultrasonication
3	deionized water	2 min	ultrasonication
4	acetone	2 min	ultrasonication
5	acetone	2 min	ultrasonication
6	acetone	2 min	ultrasonication
7	isopropyl alcohol	2 min	boiling
8	isopropyl alcohol	2 min	boiling

Table C.1: Cleaning procedure for glass substrates.

C.5 Methanol properties

Methanol is the organic solvent used to anneal Alq₃ in this thesis. Certain estimations in this thesis use the material properties of the methanol summarized in Tbl. C.2. Most of these properties were gathered from Methanol material safety data sheets. The diffusion coefficients in air are taken from Mrazek *et al.* [68]. The self-diffusion coefficient is taken from [18, Tbl. 2].

formula	CH ₃ OH
molar mass (g/mol)	32.04
density (g/cm ³)	0.7918
melting point (°C)	-97.8
boiling point (°C)	64.5
critical temperature (°C)	240
vapor pressure (@ 20°C kPa)	12.3
vapor density (air = 1)	1.11
surface tension (N/m)	0.0227
diffusion coefficient (cm ² /s)	
in air @25°C	0.162
in air @50/@55 °C	0.195–0.197
self-diffusion	2.39 × 10 ⁻⁵
dielectric constant (at 20°C)	30
solvent type	polar
viscosity (at 20°C, Pa · s)	5.44 × 10 ⁻⁴

Table C.2: Methanol properties

Bibliography

- [1] Methanol material safety data sheet. <http://fscimage.fishersci.com/msds/14280.htm>.
- [2] C. A. Angell. Formation of glasses from liquids and biopolymers. *Science*, 267(5206):1924–1935, Mar 1995.
- [3] Robert W. Balluffi, Samuel M. Allen, and W. Craig Carter. *Kinetics of materials*. Wiley-Interscience, 1 edition, 2005.
- [4] J. Becker, G. Grun, R. Seemann, H. Mantz, K. Jacobs, K. R. Mecke, and R. Blossey. Complex dewetting scenarios captured by thin-film models. *Nature Materials*, 2(1):59–63, Jan 2003.
- [5] M. Berggren, G. Gustafsson, O. Inganäs, M. R. Andersson, O. Wennerstrom, and T. Hjertberg. Thermal control of near-infrared and visible electroluminescence in alkyl-phenyl substituted polythiophenes. *Applied Physics Letters*, 65(12):1489–1491, Sep 1994.
- [6] Jozef Bicerano. *Prediction of Polymer Properties*. CRC Press, 3rd edition, 2002.
- [7] J. Bischof, D. Scherer, S. Herminghaus, and P. Leiderer. Dewetting modes of thin metallic films: Nucleation of holes and spinodal dewetting. *Physical Review Letters*, 77(8):1536–1539, Aug 1996.
- [8] C. Bollinne, S. Cuenot, B. Nysten, and A. M. Jonas. Spinodal-like dewetting of thermodynamically-stable thin polymer films. *European Physical Journal E*, 12(3):389–395, Nov 2003.

- [9] Daniel Bonn, Jens Eggers, Joseph Indekeu, Jacques Meunier, and Etienne Rolley. Wetting and spreading. *Rev. Mod. Phys.*, 81(2):739–805, May 2009.
- [10] J. W. Cahn. 1967 institute of metals lecture spinodal decomposition. *Transactions of the Metallurgical Society of AIME*, 242(2), 1968.
- [11] A. Cavagna. Supercooled liquids for pedestrians. *Physics Reports-Review Section of Physics Letters*, 476(4-6):51–124, Jun 2009.
- [12] W. Chen, Q. Peng, and Y. Li. Alq(3) nanorods: Promising building blocks for optical devices. *Advanced Materials*, 20(14):2747–+, Jul 2008.
- [13] N. V. Churaev. Contact angles and surface forces. *Advances in Colloid and Interface Science*, 58(2-3):87–118, Jul 1995.
- [14] N. Clarke. Instabilities in thin-film binary mixtures. *European Physical Journal E*, 14(3):207–210, Jul 2004.
- [15] N. Clarke. Toward a model for pattern formation in ultrathin-film binary mixtures. *Macromolecules*, 38(16):6775–6778, Aug 2005.
- [16] Benjamin P. Cook, Andrea L. Bertozzi, and A. E. Hosoi. Shock solutions for particle-laden thin films. *SIAM Journal on Applied Mathematics*, 68(3):760–783, 2008.
- [17] R. V. Craster and O. K. Matar. Dynamics and stability of thin liquid films. *Reviews of Modern Physics*, 81(3):1131, 2009.
- [18] L. X. Dang and T. M. Chang. Many-body interactions in liquid methanol and its liquid/vapor interface: A molecular dynamics study. *Journal of Chemical Physics*, 119(18):9851–9857, Nov 2003.
- [19] A. Datar, R. Oitker, and L. Zang. Surface-assisted one-dimensional self-assembly of a perylene based semiconductor molecule. *Chemical Communications*, (15):1649–1651, 2006.
- [20] P. G. de Gennes. Wetting - statics and dynamics. *Reviews of Modern Physics*, 57(3):827–863, 1985.

- [21] Pierre G. de Gennes, Francoise Brochard-Wyart, and David Quere. *Capillarity and Wetting Phenomena Drops, Bubbles, Pearls, Waves*. Springer New York, 2003.
- [22] G. de Luca, A. Liscio, P. Maccagnani, F. Nolde, V. Palermo, K. Mllen, and P. SamorI. Nucleation-governed reversible self-assembly of an organic semiconductor at surfaces: Long-range mass transport forming giant functional fibers. *Advanced Functional Materials*, 17(18):3791–3798, 2007.
- [23] G. de Luca, A. Liscio, F. Nolde, L. M. Scolaro, V. Palermo, K. Mullen, and P. Samori. Self-assembly of discotic molecules into mesoscopic crystals by solvent-vapour annealing. *Soft Matter*, 4(10):2064–2070, 2008.
- [24] P. G. Debenedetti and F. H. Stillinger. Supercooled liquids and the glass transition. *Nature*, 410(6825):259–267, Mar 2001.
- [25] B. Derjaguin and M. Kussakov. Anomalous properties of thin polymolecular films v. an experimental investigation of polymolecular solvate (adsorbed) films as applied to the development of a mathematical theory of the stability of colloids. *Acta Physicochimica URSS*, 10(1):25–44, 1939.
- [26] B. V. Derjaguin and N. V. Churaev. Structural component of disjoining pressure. *Journal of Colloid and Interface Science*, 49(2):249 – 255, 1974.
- [27] B. V. Derjaguin and Z. M. Zorin. Optical study of the adsorption and surface condensation of vapors in the vicinity of saturation on a smooth surface (reprinted from proceedings of the 2nd international-congress on surface-activity, vol 1, pg 145-152, 1957). *Progress in Surface Science*, 40(1-4):118–125, May-Aug 1992.
- [28] K. C. Dickey, J. E. Anthony, and Y. L. Loo. Improving organic thin-film transistor performance through solvent-vapor annealing of solution-processable triethylsilylethynyl anthradithiophene. *Advanced Materials*, 18(13):1721–+, July 2006.
- [29] Ken A. Dill and Sarina Bromberg. *Molecular Driving Forces: Statistical Thermodynamics in Chemistry and Biology*. Garland Science, 2002.

- [30] C. D. Dimitrakopoulos and P. R. L. Malenfant. Organic thin film transistors for large area electronics. *Advanced Materials*, 14(2):99–+, Jan 2002.
- [31] Jrgen Evers, Peter Klfers, Rudolf Staudigl, and Peter Stallhofer. Czochralski’s creative mistake: A milestone on the way to the gigabit era. *Angewandte Chemie International Edition*, 42(46):5684–5698, 2003.
- [32] G. Foffi, W. Gotze, F. Sciortino, P. Tartaglia, and T. Voigtmann. Mixing effects for the structural relaxation in binary hard-sphere liquids. *Physical Review Letters*, 91(8):085701, Aug 2003.
- [33] S. R. Forrest. The path to ubiquitous and low-cost organic electronic appliances on plastic. *Nature*, 428(6986):911–918, Apr 2004.
- [34] R. H. Friend, R. W. Gymer, A. B. Holmes, J. H. Burroughes, R. N. Marks, C. Taliani, D. D. C. Bradley, D. A. Dos Santos, J. L. Bredas, M. Logdlund, and W. R. Salaneck. Electroluminescence in conjugated polymers. *Nature*, 397(6715):121–128, Jan 1999.
- [35] K. B. Glasner. Spreading of droplets under the influence of intermolecular forces. *Physics of Fluids*, 15(7):1837–1842, Jul 2003.
- [36] K. B. Glasner. Ostwald ripening in thin film equations. *SIAM Journal on Applied Mathematics*, 69(2):473–493, 2008.
- [37] K. B. Glasner and T. P. Witelski. Collision versus collapse of droplets in coarsening of dewetting thin films. *Physica D: Nonlinear Phenomena*, 209(1-4):80–104, 9 2005/9/15.
- [38] KB Glasner and TP Witelski. Coarsening dynamics of dewetting films. *Physical Review E*, 67(1, Part 2), JAN 2003.
- [39] J. M. Gomba and G. M. Homsy. Analytical solutions for partially wetting two-dimensional droplets. *Langmuir*, 2009.
- [40] W. Gotze and T. Voigtmann. Effect of composition changes on the structural relaxation of a binary mixture. *Physical Review E*, 67(2):021502, Feb 2003.

- [41] L. Granasy, T. Pusztai, T. Borzsonyi, J. A. Warren, and J. F. Douglas. A general mechanism of polycrystalline growth. *Nature Materials*, 3(9):645–650, Sep 2004.
- [42] R. W. Hamming. *Numerical Methods for Scientists and Engineers*. Dover Publications, 1973.
- [43] Eugene Hecht. *Optics*. Pearson Education, 4th edition, 2002.
- [44] A. E. Hosoi and J. W. M. Bush. Evaporative instabilities in climbing films. *Journal of Fluid Mechanics*, 442:217–239, SEP 10 2001.
- [45] Jacob N. Israelachvili. *Intermolecular and Surface Forces*. Academic Press, 2 edition, 1991.
- [46] J. Jackle. Models of the glass-transition. *Reports on Progress in Physics*, 49(2):171–231, Feb 1986.
- [47] Serafim Kalliadasis and Uwe Thiele. *Thin Films of Soft Matter*. Springer Vienna, 2007.
- [48] J. C. T. Kao, A. A. Golovin, and S. H. Davis. Rupture of thin films with resonant substrate patterning. *Journal of Colloid and Interface Science*, 303(2):532–545, Nov 2006.
- [49] H. E. Katz. Recent advances in semiconductor performance and printing processes for organic transistor-based electronics. *Chemistry of Materials*, 16(23):4748–4756, Nov 2004.
- [50] K. F. Kelton. Crystal nucleation in liquids and glasses. *Solid State Physics-Advances in Research and Applications*, 45:75–177, 1991.
- [51] R. U. A. Khan, O. P. Kwon, A. Tapponnier, A. N. Rashid, and P. Gunter. Supramolecular ordered organic thin films for nonlinear optical and optoelectronic applications. *Advanced Functional Materials*, 16(2):180–188, Jan 2006.

- [52] H. I. Kim, C. M. Mate, K. A. Hannibal, and S. S. Perry. How disjoining pressure drives the dewetting of a polymer film on a silicon surface. *Physical Review Letters*, 82(17):3496–3499, Apr 1999.
- [53] J. S. Langer. Instabilities and pattern-formation in crystal-growth. *Reviews of Modern Physics*, 52(1):1–28, 1980.
- [54] R. Limary and P. F. Green. Dynamics of droplets on the surface of a structured fluid film: Late-stage coarsening. *Langmuir*, 19(6):2419–2424, Mar 2003.
- [55] Shuhong Liu, Wechung Maria Wang, Alejandro L. Briseno, Stefan C. B. Mannsfeld, and Zhenan Bao. Controlled deposition of crystalline organic semiconductors for field-effect-transistor applications. *Advanced Materials*, 2009.
- [56] N. J. Long. Organometallic compounds for nonlinear optics - the search for en-light-enment. *Angewandte Chemie-International Edition in English*, 34(1):21–38, Jan 1995.
- [57] G. Malliaras and R. Friend. An organic electronics primer. *Physics Today*, 58(5):53–58, May 2005.
- [58] D. J. Mascaro. *Formation of in-plane crystals of molecular organic semiconductors*. PhD thesis, MIT, 2004.
- [59] D. J. Mascaro, M. E. Thompson, H. I. Smith, and V. Bulovic. Forming oriented organic crystals from amorphous thin films on patterned substrates via solvent-vapor annealing. *Organic Electronics*, 6(5-6):211–220, December 2005.
- [60] O. K. Matar. Nonlinear evolution of thin free viscous films in the presence of soluble surfactant. *Physics of Fluids*, 14(12):4216–4234, 2002.
- [61] A. Mazouchi and G. M. Homsy. Free surface stokes flow over topography. *Physics of Fluids*, 13(10):2751–2761, Oct 2001.
- [62] E. W. Meijer and A. P. H. J. Schenning. Chemistry - material marriage in electronics. *Nature*, 419(6905):353–354, Sep 2002.

- [63] Amy Meyers and Marcus Weck. Solution and solid-state characterization of alq3-functionalized polymers. *Chemistry of Materials*, 16(7):1183–1188, 2004.
- [64] S. Miller, G. Fanchini, Y. Y. Lin, C. Li, C. W. Chen, W. F. Su, and M. Chhowalla. Investigation of nanoscale morphological changes in organic photovoltaics during solvent vapor annealing. *Journal of Materials Chemistry*, 18(3):306–312, 2008.
- [65] V. S. Mitlin. Dewetting of solid-surface - analogy with spinodal decomposition. *Journal of Colloid and Interface Science*, 156(2):491–497, Mar 1993.
- [66] J. V. Moloney and A. C. Newell. *Nonlinear Optics*. Westview Press, 2004.
- [67] J.-F. Moulin, M. Brinkmann, A. Thierry, and J.-C. Wittmann. Oriented Crystalline Films of Tris(8-hydroxyquinoline) Aluminum(III): Growth of the Alpha Poly-morph onto an Ultra-Oriented Poly(tetrafluoroethylene) Substrate. *Advanced Materials*, 14(6):436–439, 2002.
- [68] Robert V. Mrazek, Charles E. Wicks, and K. N. S. Prabhu. Dependence of the diffusion coefficient on composition in binary gaseous systems. *Journal of Chemical & Engineering Data*, 13(4):508–510, 1968.
- [69] L. O. Naraigh and J. L. Thiffeault. Nonlinear dynamics of phase separation in thin films. *Nonlinearity*, 23(7):1559–1583, Jul 2010.
- [70] W. J. Nie. Optical nonlinearity - phenomena, applications, and materials. *Advanced Materials*, 5(7-8):520–545, Jul-Aug 1993.
- [71] Milton Ohring. *Materials science of thin films: Deposition and structure*. Academic Pr, 2nd edition, 2001.
- [72] A. Oron. Three-dimensional nonlinear dynamics of thin liquid films. *Physical Review Letters*, 85(10):2108–2111, Sep 2000.
- [73] A. Oron and S. G. Bankoff. Dewetting of a heated surface by an evaporating liquid film under conjoining/disjoining pressures. *Journal of Colloid and Interface Science*, 218(1):152–166, Oct 1999.

- [74] A. Oron, S. H. Davis, and S. G. Bankoff. Long-scale evolution of thin liquid films. *Reviews of Modern Physics*, 69(3):931–980, Jul 1997.
- [75] J. Oscik. *Adsorption*. Halsted Press, 1982.
- [76] V. Palermo and P. Samori. Molecular self-assembly across multiple length scales. *Angewandte Chemie-International Edition*, 46(24):4428–4432, 2007.
- [77] S.V. Patankar. *Numerical heat transfer and fluid flow*. 1980.
- [78] William H. Press, Saul A. Teukolsky, William T. Vetterling, and Brian P. Flannery. *Numerical recipes in C: the art of scientific computing*. Cambridge University Press, New York, NY, USA, 1992.
- [79] E. Rabani, D. R. Reichman, P. L. Geissler, and L. E. Brus. Drying-mediated self-assembly of nanoparticles. *Nature*, 426(6964):271–274, Nov 2003.
- [80] G. Reiter. Dewetting of thin polymer-films. *Physical Review Letters*, 68(1):75–78, Jan 1992.
- [81] J. Kern Sears and Joseph R. Darby. *Technology of Plasticizers*. John Wiley & Sons, 1982.
- [82] A. Sharma. Many paths to dewetting of thin films: anatomy and physiology of surface instability. *European Physical Journal E*, 12(3):397–407, Nov 2003.
- [83] A. Sharma and R. Khanna. Pattern formation in unstable thin liquid films. *Physical Review Letters*, 81(16):3463–3466, Oct 1998.
- [84] Ashutosh Sharma. Relationship of thin film stability and morphology to macroscopic parameters of wetting in the apolar and polar systems. *Langmuir*, 9(3):861–869, 03 1993.
- [85] Jin Sheng Sheu and Jer Ru Maa. The inception of condensation of water vapor on smooth solid substrates. *Journal of Colloid and Interface Science*, 135(1):178 – 184, 1990.

- [86] Y. Shirota and H. Kageyama. Charge carrier transporting molecular materials and their applications in devices. *Chemical Reviews*, 107(4):953–1010, Apr 2007.
- [87] G. I. Stegeman and R. H. Stolen. Wave-guides and fibers for nonlinear optics. *Journal of the Optical Society of America B-Optical Physics*, 6(4):652–662, Apr 1989.
- [88] G.I. Stegeman, E.M. Wright, N. Finlayson, R. Zanoni, and C.T. Seaton. Third order nonlinear integrated optics. *Lightwave Technology, Journal of*, 6(6):953 –970, jun 1988.
- [89] E. Sultan, A. Boudaoud, and M. Ben Amar. Evaporation of a thin film: diffusion of the vapour and marangoni instabilities. *Journal of Fluid Mechanics*, 543:183–202, Nov 2005.
- [90] G. F. Teletzke, H. T. Davis, and L. E. Scriven. How liquids spread on solids. *Chemical Engineering Communications*, 55(1-6):41–82, 1987.
- [91] G. F. Teletzke, H. T. Davis, and L. E. Scriven. Wetting hydrodynamics. *Revue de Physique Appliquee*, 23(6):989–1007, Jun 1988.
- [92] U. Thiele. Open questions and promising new fields in dewetting. *European Physical Journal E*, 12(3):409–414, Nov 2003.
- [93] U. Thiele. Thin film evolution equations from (evaporating) dewetting liquid layers to epitaxial growth. *Journal of Physics-Condensed Matter*, 22(8):084019, Mar 2010.
- [94] U. Thiele, S. Madruga, and L. Frastia. Decomposition driven interface evolution for layers of binary mixtures. i. model derivation and stratified base states. *Physics of Fluids*, 19(12):122106, Dec 2007.
- [95] U. Thiele, M. G. Velarde, and K. Neuffer. Dewetting: Film rupture by nucleation in the spinodal regime. *Physical Review Letters*, 87(1):016104, Jul 2001.
- [96] Xike Tian, Jinbo Fei, Zhenbang Pi, Chao Yang, Dongyue Luo, Fang Pei, and Lide Zhang. Selective temperature physical vapor deposition route to tri(8-hydroquinoline)aluminum nanowires, nanowalls, nanoclusters and micro-spherical chains. *Solid State Communications*, 138(10-11):530 – 533, 2006.

- [97] A. M. P. Valli, G. F. Carey, and A. L. G. A. Coutinho. Control strategies for timestep selection in finite element simulation of incompressible flows and coupled reaction-convection-diffusion processes. *International Journal for Numerical Methods in Fluids*, 47(3):201–231, 2005.
- [98] Richard van Hameren, Peter Schoen, Arend M. van Buul, Johan Hoogboom, Sergiy V. Lazarenko, Jan W. Gerritsen, Hans Engelkamp, Peter C. M. Christianen, Hans A. Heus, Jan C. Maan, Theo Rasing, Sylvia Speller, Alan E. Rowan, Johannes A. A. W. Elemans, and Roeland J. M. Nolte. Macroscopic hierarchical surface patterning of porphyrin trimers via self-assembly and dewetting. *Science*, 314(5804):1433–1436, DEC 1 2006.
- [99] D. S. Wang, T. Xie, and Y. D. Li. Nanocrystals: Solution-based synthesis and applications as nanocatalysts. *Nano Research*, 2(1):30–46, Jan 2009.
- [100] M. R. E. Warner, R. V. Craster, and O. K. Matar. Surface patterning via evaporation of ultrathin films containing nanoparticles. *Journal of Colloid and Interface Science*, 267(1):92–110, Nov 2003.
- [101] J. S. Wettlaufer and M. G. Worster. Premelting dynamics. *Annual Review of Fluid Mechanics*, 38:427–452, 2006.
- [102] X. L. Xiao, Z. J. Hu, Z. B. Wang, and T. B. He. Study on the single crystals of poly(3-octylthiophene) induced by solvent-vapor annealing. *Journal of Physical Chemistry B*, 113(44):14604–14610, Nov 2009.
- [103] X. L. Xiao, Z. B. Wang, Z. J. Hu, and T. A. B. He. Single crystals of polythiophene with different molecular conformations obtained by tetrahydrofuran vapor annealing and controlling solvent evaporation. *Journal of Physical Chemistry B*, 114(22):7452–7460, Jun 2010.
- [104] R. Xie, A. Karim, J. F. Douglas, C. C. Han, and R. A. Weiss. Spinodal dewetting of thin polymer films. *Physical Review Letters*, 81(6):1251–1254, Aug 1998.

- [105] N. Xu, T. K. Haxton, A. J. Liu, and S. R. Nagel. Equivalence of glass transition and colloidal glass transition in the hard-sphere limit. *Physical Review Letters*, 103(24):245701, Dec 2009.
- [106] J. J. Zhou, B. Dupuy, A. L. Bertozzi, and A. E. Hosoi. Theory for shock dynamics in particle-laden thin films. *Physical Review Letters*, 94(11):117803, Mar 2005.